Title
Developing Interfacial Solar Vapor Generation into a Sustainable Desalination Technology

Author
Finnerty, Casey Thomas Kazuyuki

Publication Date
2022

Peer reviewed|Thesis/dissertation

Developing Interfacial Solar Vapor Generation into a Sustainable Desalination Technology

by

Casey Thomas Kazuyuki Finnerty

A dissertation submitted in partial satisfaction of the

requirements for the degree of

Doctor of Philosophy

in

Civil Environmental Engineering

and the Designated Emphasis

in

Development Engineering

in the

Graduate Division

of the

University of California, Berkeley

Committee in charge:

Professor Baoxia Mi, Chair
Professor Kara Nelson
Professor Alice Agogino

Summer 2022

Developing Interfacial Solar Vapor Generation into a Sustainable Desalination Technology

Abstract

Developing Interfacial Solar Vapor Generation into a Sustainable Desalination Technology

by

Casey Thomas Kazuyuki Finnerty

Doctor of Philosophy in Civil Environmental Engineering

and the Designated Emphasis in

Development Engineering

University of California, Berkeley

Professor Baoxia Mi, Chair

Seawater desalination is one of the most resilient approaches for obtaining water. However, conventional desalination technologies are also some of the most energy-intensive water treatment processes. For this reason, seawater desalination is often viewed as a last resort, and is generally only an option for large urban centers—where the costs can be spread across densely populated districts. With limited access to reliable power grids, technical and managerial expertise, essential supply chains, and financial resources, smaller communities are often the most vulnerable to the impacts of climate change.

Interfacial solar vapor generation (ISVG) is a phenomenon observed in nano-enabled materials to efficiently vaporize water at extremely high efficiencies when exposed to sunlight. Traditionally, these are porous, light-absorbing materials that float at the air-water interface where evaporation normally takes place. When irradiated by sunlight, these materials absorb that light, convert that light into heat, transfer that heat to water in its pores, and accelerate the rate of evaporation. As a result, these 2D-ISVG materials can achieve an evaporative flux of 2.00 $kg\ m^{-2}\ h^{-1}$, which is nearly 200% higher than natural rates. While impressive, this rate is still too low for many practical applications. To increase this rate, we have developed a 3D-ISVG material that utilizes capillary action to wick water onto additional surfaces for evaporation. This enhancement has allowed us to achieve an evaporative flux of 34.7 $kg\ m^{-2}\ h^{-1}$. Given this higher productivity, we have begun evaluating the feasibility of developing 3D-ISVG into a sustainable desalination technology for small-island communities. Specifically, we have been working with Bungin Island in Indonesia to understand how contextual factors should inform the design and implementation of this technology as a means of providing sustainable water access in a climate-impacted future.

To the CEE Student Community at UC Berkeley

Students come to the Civil Environmental Engineering Department at UC Berkeley wanting to make the world a better place. And it is this desire to change the world around us that has grown the CEE community into what it is today. I am so grateful to have been able to build upon the legacy of CEE alumni in our attempts to make this place better for students and reciprocate the love that I have felt during my time here. For future CEE students, keep fighting the fight, continue to organize, and stay hopeful, because—to quote the movie *Rat Race* (2001)—"good things take time, but great things happen all at once."

Contents

List of Figures

List of Tables

Acknowledgments

This dissertation is the result of the collective and cumulative efforts of so many people throughout my life. While I won't be able to thank everyone who has helped shape me into the person I am today—nor will I even be able to convey the depth of my gratitude for those who are acknowledged here—please know how grateful I am for all of your love and support over the years.

I want to start with my family. To my mom, Debbie Finnerty, thank you for raising me in the intellectually-stimulating environment of your 2nd grade classroom. Even though I would complain about having to stay on campus hours after my classmates had all gone home, those years instilled in me a love for learning that I still carry with me today. To my dad, Peter Finnerty, thank you for pushing me to always strive for excellence, even if that meant crying as you checked my middle school math homework. Thank you for those deep car conversations that broadened the horizons of my imagination, and allowing me to share in your dream to leave this world a better place than how you found it. And to my brother, Brendan Finnerty, thank you for being my hero. You are kind, humble, selfless, and my definition of a truly good person. I would also like to thank my aunt and uncle, Curtis and Sharon Sakai. Thank you for making Berkeley my home away from home. I cannot thank you enough for the support system you provided for me in the Bay Area, especially when that support system comes with spaghetti.

Growing up, I had some amazing teachers and coaches who helped guide me through the formative years of primary and secondary school. Thank you to Mrs. Hustwick, for giving me my first periodic table even when I didn't know what it was at the time. Thank you to Ms. Silver for encouraging me to be myself, even though that meant you had to read my essay about poop. Thank you to Mr. Shen for teaching me the importance of history, and tolerating how much I doodled in your class. Thank you to Sñr. Ortiz for showing me that subjects aren't siloed and there are many different ways to learn. Thank you to Mrs. Hartford for supporting my interest in environmental challenges, and for taking our class to SeaWorld. Thank you to Mrs. Merritt for introducing me to engineering and being an extraordinary teacher; I don't know how you covered so many topics in a single year. Thank you to Mrs. Dunlap for teaching me how to think critically and how to write; most of my success as a scientist has come from this ability to write. Thank you to Mr. Sogo for introducing me to the exciting world of research and pushing me to "do the right thing." And thank you to Mr. (Dave) Brobeck, for showing me what it takes to foster a supportive community and teaching me how to be a leader.

While undergrad is a tumultuous time for everyone, I was fortunate to have many friends and mentors at UC Berkeley who not only helped me stay afloat, but supported me as I figured who I was and what I wanted to do with my life. Thank you to Drs. Michelle Douskey and Marty Mulvihill for my first job in STEM, working for the Berkeley Center for

Green Chemistry. Thank you to Professor Danielle Tullman-Ercek for not only providing me with my first research experience, but also fostering such a welcoming environment for undergraduate students. Thank you to my graduate student mentor in the DTE Lab, Dr. Kevin Metcalf, who taught me how to be a researcher, helped me realize my passion for water quality improvement, and was the first to encourage me to apply to graduate school. Thank you to my friend and classmate, Dr. Akshita Dutta, without whom I would have failed most of our chemical engineering and chemistry classes. Thank you to my first environmental engineering instructor, Dr. Khalid Kadir, for showing me what environmental engineering could be and continuously supporting student efforts to find and build community. And thank you to Professor Kara Nelson for allowing me to take her pathogens course as an undergraduate student and writing me a recommendation letter that I consider to be the only reason I was accepted into any graduate programs. I also want to thank Jon Goodman for my first job and teaching me about the water industry, as well as Lyndsey Wiles for being such a supportive friend and coworker during my two years at TriSep Corporation.

Returning to UC Berkeley in the Environmental Engineering graduate program, I was (and continue to be) amazed by my fellow students. I want to thank my entire ENV M.S. cohort (2015-2016), as well as the many friends I have made, both within and outside of the department throughout my time here. The friendship you have all shown me means more than I can put into words. Specifically, thank you to Dr. Katya Cherukumilli for being a welcoming bridge into the ENV program both when I was an undergraduate and graduate student. Thank you to Drs. Scott Miller, Aidan Cecchetti, and Rachel Scholes, whose leadership and involvement in ReNUWIt's Student Postdoc Committee on Diversity Inclusion (SPCDI) sparked a culture of activism and advocacy within the ENV program. Furthermore, I want to thank Rachel Scholes for being a mentor and teaching me how to use the solar simulator (a *critical* instrument for my research). Thank you to Dr. Vivek Rao for also being an early mentor to me and recommending mechanical engineering courses where I could start learning more heat transfer. Thank you to Dr. Siva Bandaru for always being willing to workshop new research and teaching ideas. Thank you to Drs. Emily Cook and Lauren Kennedy for starting the Environmental Engineering Advocacy Team (EEAT) and including me in their peer support group to help me get to the finish line. Additionally, I want to thank Emily Cook for being my co-conspirator on so many different projects in our attempts to make graduate school more accessible and inclusive. Thank you to Dr. Liya Weldegebriel for letting me interrupt your work whenever I walked by your office and for being an inspiring example of true strength. Thank you to James Neher for tutoring me when my math skills were rusty when returning to school, and for introducing me to DD and being an awesome DM. Thank you to Sol Fusi for teaching me to not blindly accept what we are taught and initiating discussions to engage with course materials more deeply. Thank you to Minerva Teli and Alice Hsu for carrying on the torch of activism and advocacy, both in our department and beyond. And thank you to Bavisha Kalyan, Luis Anaya, and Dr. George Moore for creating a space where we can imagine new paradigms of research, teaching, and societal impact. Lastly, thank you to Bavisha Kalyan for having high expectations of me, joining me

on side quests, and being my academic BFF.

I also want to thank my research community. First, I would like to thank my advisor, Professor Baoxia Mi. Thank you for taking me on as your first student from UC Berkeley and giving me the freedom to explore a totally new field for us both. It has been a dream come true working on this project and I can't thank you enough for the opportunity. Thank you to Professors Van Carey and Akanksha Menon for their insights on phase-change heat transfer processes. Thank you to Professors Joeva Rock and Alice Agogino, as well as Dr. Yael Perez, for their support of the Development Engineering aspects of this project. And thank you to Professor David Sedlak for your mentorship with regards to my research project and professional development. I would also like to thank Dr. Sean Zheng for setting up the lab at UC Berkeley and serving as a mentor to myself and many of our labmates. Thank you to Dr. Zhongyun Liu for your kindness in the early years of my Ph.D. and for being my first collaborator. Thank you to Monong Wang, for all of the time and energy you put into supporting our entire lab. Thank you to Kelly Conway, for your patients as we iterated (for years) on which direction to take this research project. And thank you to Courtney Turkatte, for a rewarding mentoring experience and pushing me to be more thoughtful, both as a researcher and an individual. Furthermore, I would like to thank the faculty, staff, and community who keep this place running. Thank you to Shelley Okimoto for having been such an uplifting presence in the department and guiding me through all of the program requirements. Thank you to Jackie Garcia for keeping Davis and O'brien operational, which is not an easy feat. Thank you to Jacob Gallego, Karen Hom, and Jeff Higginbotham from the ME Student Machine Shop and Matt Cataleta and Llyr Griffith from the CEE Machine Shop for their support in fabricating experimental setups and prototyping. I would also like to thank Li Ci Lau for her warm greetings each morning and Abe Rodriguez for supplying the best coffee in Berkeley. And thank you to Professors Tina Chow, Evan Variano, and Mark Stacey for all of the service for the department, as well as their support of the CEE student organizations.

Finally, I want to thank John Palfreyman for being one of my closest friends since we were kids. Thanks to Ryan Priest and Sam Cronin for helping keep things light over the years. Thanks to C.J. Miller and Elaine Ou for showing us how much fun the (East) Bay can be. Thanks to Daniel Ocasio and Mike Alves for being the best neighbors. And last, and certainly not least, I want to thank my partner for the past 10 years—and now fiancée—Melanie De Anda (as well as our dog, Maui). You have been endlessly patient as I have pursued this dream. Even though you think my research is "just logic", I could not have done this without your support; from helping me strategically phrase emails to listening when I need to get stuff off my mind. I am extraordinarily lucky to have had your love throughout this journey and am so grateful to be by your side for the next adventure!

Chapter 1

Introduction

1.1 Challenge Definition

Water access serves as the foundation upon which all societies have developed. Water is essential for food production, energy generation, and human consumption[1]—and the demand for water is continuously rising. By 2050, water demand is expected to increase by 55%[2] as a result from population growth and industrial expansion. Concurrently, overexploitation, pollution, and climate change are decreasing water availability,[3] and it is projected that an additional 1.8 billion people will fall into water stress in the next 30 years. To prevent this catastrophe, alternative water sources need to be considered. One alternative that is gaining prominence are saline sources. These saline sources contain varying levels of total dissolved solids (TDS) and are typically found as brackish water from groundwater aquifers (500 – 30,000 mg/L TDS), saline water from seawater sources (30,000 – 50,000 mg/L), and hypersaline water from brine-producing operations (>50,000 mg/L TDS). The TDS levels of saline sources are typically too high for industrial use and would be dangerous for human consumption. However, desalination technologies can remove TDS, making the water fit for use or consumption. Desalination is primarily achieved by reverse osmosis (RO),[4] where feedwater is pressurized to overcome its osmotic potential (which is directly correlated to TDS) and forced through a semipermeable membrane while dissolved salts are rejected and concentrated into a waste stream. The treated water stream is known as permeate; the amount of permeate produced relative to the amount of feed is known as recovery. Although desalination has the potential to dramatically expand our water resources, this technology has two fundamental drawbacks that limit its applicability: energy consumption and brine management.

The energy required for any desalination process is inextricably tied to the TDS of the feedwater. Treating desalination as a reversible thermodynamic process, the minimum energy required for desalination (E_{min}) is the negative of the change in free energy ($-d(G_{mix})$) upon mixing salt into pure water. This value can be computed by integrating the osmotic

pressure (Π) as a function of produced permeate volume (V_P). As osmotic pressure is a function of TDS concentration, the minimum energy required for desalination increases as a function of the feed TDS concentration and recovery. Despite dramatic advancements in membrane technology over the past few decades,[5] further improvements in energy efficiency appear to be constrained by this thermodynamic limit. Unfortunately, the actual energy required for desalination is higher because of auxiliary processes like intake, pretreatment, post-treatment, and waste disposal, making it significantly more energy intensive than other water acquisition methods[6] (Figure 1.1).

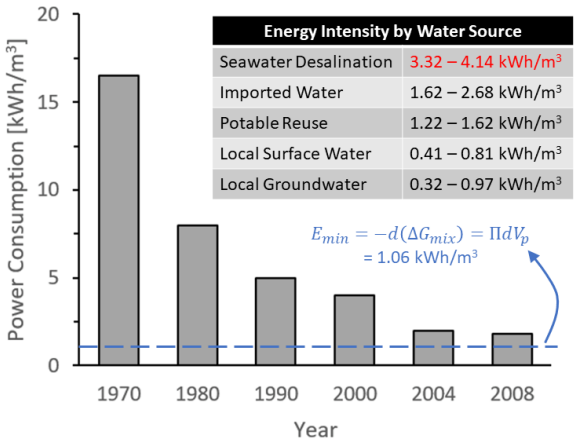

Figure 1.1: The power consumption for RO approaching its thermodynamic limit (figure adapted from Elimelech & Phillip, 2011).[5] The table shows that operation at this limit is comparable or higher than most alternative water sources (data from FBEI report for San Diego, 2010),[6] while practical operation requires significantly more energy (see Seawater Desalination in red).

Waste disposal presents its own challenges as well. Brine management is the proper disposal of the waste stream (brine) produced in most desalination processes. In addition to all the rejected salts, brine may also contain hazardous constituents[7] (e.g., metals, nutrients, pesticides, and other contaminants of emerging concern) and chemical additives[8] (e.g., antiscalants and biocides) that may have adverse effects when discharged. Depending on the recovery, the brine concentration from RO can reach up to 75,000 mg/L, twice the concentration of seawater. Although discharging brine into the ocean is typically the most economical method of brine management, at this high concentration, the brine is denser than seawater. Therefore, extra precautions, like the use of multi-port diffusers to gradually dilute the brine, are necessary so that the brine does not stratify and create dead zones on the ocean floor.[9] Brine management options for inland desalination system tend to be even more expensive, including surface water discharge, deep well injection, evaporation ponds, or zero liquid discharge.[10] Both surface water discharge and deep well injection require extensive surveying and permitting to ensure little to no ecological or geological harm is being done. Evaporation ponds require large areas and their effectiveness varies by climate. Finally, zero liquid discharge (ZLD) is the process of removing all liquids from a brine stream so that only the previously dissolved solids remain. This process, however, is extremely energy-intensive, typically relying on thermally-driven processes to concentrate and crystallize the brine.[11] All of these options can be expensive, which is why brine management is often the limiting factor for the implementation of desalination in inland applications.

The outlook for desalination does not change significantly when considering emerging technologies. Most of these technologies—like forward osmosis and membrane distillation—have focused on reducing energy demand by being able to utilize waste heat for desalination. However, these processes still produce brine and have yet to demonstrate significant energy savings in comparison to RO. Solar desalination is the process of using the heat generated from sunlight to promote the evaporation of water from a saline source. The water vapor generated by this process can be separately condensed into purified water. Despite this technique having been practiced for thousands of years, widespread adoption of solar desalination has been limited due to the low and variable water production rates that sunlight can support. To compensate, these systems require large areas to capture sufficient solar energy for water production, which has traditionally made solar desalination too costly. However, interest in solar desalination has recently been revitalized with the advent of interfacial solar vapor generation.

1.2 Interfacial Solar Vapor Generation

Interfacial solar vapor generation (ISVG) occurs at the interface of a light-absorbing material and water. Upon absorbing sunlight, the material locally transfers thermal energy to adjacently located water, which induces vaporization. In 2012, Neumann et al. demonstrated this phenomenon using a dispersed solution of light-absorbing gold nanoparticles, achieving a solar-conversion or evaporation efficiency of 24% with a solar input of 1 $kW\ m^{-2}$ (equivalent to the light intensity of 1 sun).[12] In 2014, Wang et al. created a plasmonic film with a floating dispersion of gold nanoparticles that was able to localize heating to the air-water interface, increasing evaporation efficiency to 44% using a high-intensity, 532-nm laser.[13] Around the same time, Ghasemi et al. developed a floating, carbon-based structure with broadband light absorption that more effectively localized heat, further improving evaporation efficiency to 64% and demonstrating an evaporative flux of 1.09 $kg\ m^{-2}\ h^{-1}$ under 1-sun conditions.[14] Through research that has built on these initial landmark studies, three key characteristics have emerged as being essential for ISVG (Figure 1.2):

1. *Porous Material for Light Absorption* - To maximize energy available for evaporation, the ISVG material should have broadband light absorption while maintaining a porous structure to facilitate mass and heat transfer by enabling capillary flow and increasing the amount of surface area that is in contact with the water.

2. *Insulation for Heating Localization* - To minimize heat loss, the evaporative interface of ISVG material should be insulated from the source water reservoir, as well as shielded from other heat loss mechanisms.

3. *Mechanism for Water Replenishment* - To enable continuous operation, the ISVG material should have a means of transporting water from the source water reservoir to its porous internal structure (typically achieved by capillary wicking).

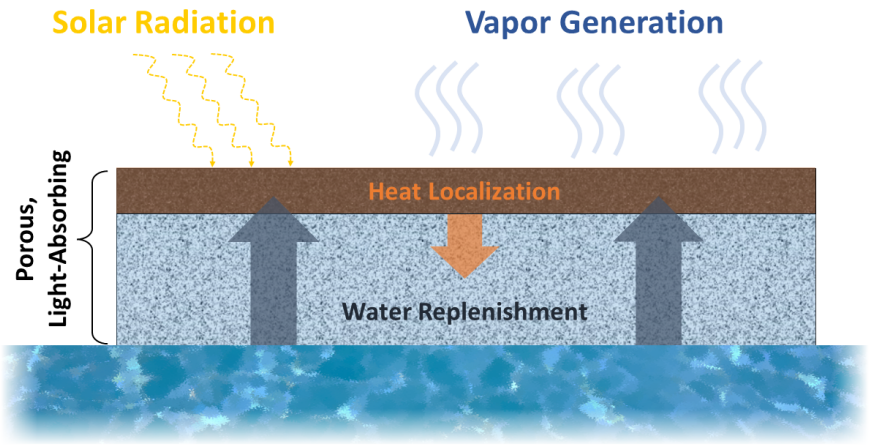

Figure 1.2: The key characteristics of ISVG materials: (1) porous material for light absorption, (2) insulation for heat localization, and (3) a mechanism for water replenishment. These characteristics enable ISVG materials to efficiently convert solar radiation into energy for vapor generation.

While interfacial solar vapor generation is still a relatively young field (as of 2022), it has already undergone several thematic arcs. These include (1) an explosion in the demonstration of various materials that are capable of ISVG, (2) a fascination with maximizing and pushing the limits of energy efficiency, and (3) the current thrust to enhance evaporative throughput to increase relevance for specific applications. Relaying the history of these thematic arcs is important because it provides a contextual understanding of the state of the field as the research being presented in this dissertation was being conducted (2016 - 2022), as well as an indication of where the field may be heading in the future.

1.3 Research Development in ISVG Field

Development of Various ISVG Materials (2014 - 2019)

While foundational to the formation of ISVG as a field, Neumann et al.[12] and Wang et al.[13] both studied nanoparticle suspensions, which would not conventionally be considered ISVG materials. The work of Ghasemi et al. was distinct because they studied a cohesive material that floated at the air-water interface.[14] A key feature of their material was its double-layered structure, which consists of (1) a photothermal layer responsible for light absorption and providing surface area for evaporation, and (2) a base layer that simultaneously provides insulation for heat localization and wicked water to the evaporative interface.

This double-layered structure has been highly influential and served as the archetype for hundreds of ISVG materials.[15] A majority of this diversity is derived from the wide range of nanomaterials that can serve as the photothermal layer.

As previously indicated, the primary purpose of the photothermal layer is to absorb light, convert that light into heat, and transfer that heat to adjacently-located water to promote evaporation. This photothermal conversion is typically accomplished through one of the following mechanisms: (1) plasmonic localized heating of metals, (2) non-radiative relaxation of semiconductors, and (3) thermal vibration of carbon-based materials (Figure 1.3):[16]

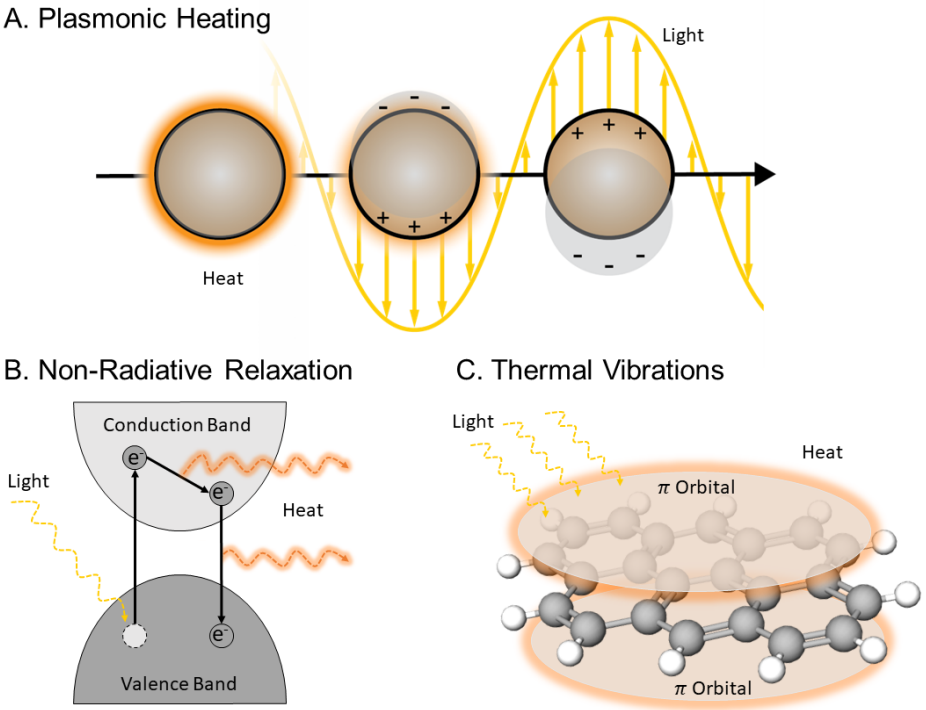

Figure 1.3: The most common photothermal mechanisms for ISVG materials: (A) plasmonic localized heating of metals, (B) non-radiative relaxation of semiconductors, and (C) thermal vibrations of carbon-based materials. Ultimately, each of these mechanisms are efficient at converting light into heat.

- *Plasmonic Localized Heating of Metals* - Localized surface plasmon resonance (LSPR) occurs when metallic nanomaterials are illuminated at their resonance wavelengths, which causes surface electrons to oscillate. As these electrons relax, they cause electron-electron scattering that rapidly dissipates energy through the increase in localized surface temperatures. The wavelengths that induce LSPR can be tuned depending on the shape, size, dielectric coating, and surrounding medium of the metal nanomaterials. While gold is the most common metal nanomaterial used for ISVG,[12, 17, 18] aluminum, copper, cobalt, nickel, silver, palladium, and platinum have also been used.[19,

20] However, the high cost of raw materials—as well as the extensive processing required to achieve broadband light absorption—has ultimately limited the applicability of plasmonic localized heating of metals for ISVG.

- *Non-Radiative Relaxation of Semiconductors* - Semiconducting materials that have traditionally been studied in photovoltaic applications have also been investigated for ISVG. Absorption of photons with energies that exceed their band gap energy promotes the excitation of electrons from the valence band to the conduction band, causing the formation of electron-hole pairs. As these electrons relax to the edge of the conduction band they generate heat through the thermal dissipation of energy. Now at a lower energy level, the electron is able to recombine with its hole by releasing phonons—as opposed to photons—which are thermal vibrations absorbed by the material to generate heat. The electron will continue to release energy through thermal dissipation as it relaxes from the edge of the valence band to its ground state. While a variety of inorganic semiconductors have been researched for ISVG,[16] metal oxides have demonstrated the greatest potential because of their tunable bandgaps in the visible-near infrared region and relatively lower cost.[21, 22] However, at lower temperatures—which is common for ISVG applications—the electrons tend to occupy lower energy states in the valence band and are less effective at absorbing low-energy photons as a result.

- *Thermal Vibration of Carbon-Based Materials* - Carbon-based materials—on the other hand—have a peculiar lamellar structure that allows electrons to be excited from the π orbital to the π^* orbital with even low-energy photons. As a result, carbon-based materials are able to achieve broadband light absorption with relatively minimal processing. Popular carbon-based materials have included carbon nanotubes, graphene oxide, carbon black, and carbonized biomaterials.[23, 24, 25] Due to their high efficacy, low-cost, and simple fabrication, carbon-based materials have come to dominate the ISVG field.

On the flip side, the base layer—which is primarily responsible for providing insulation for heat localization and capillary action for water replenishment—often takes one of two forms: (1) composite or (2) contactless (Figure 1.4):

- *Composite Base Layer* - The composite base was popularized by the double-layered structure used by Ghasemi et al. in 2014,[14] as well as the bilayered biofoam synthesized by Jiang et al. in 2016.[26] In this configuration, the photothermal layer is often synthesized directly to the top of the base layer. These materials are typically porous and hydrophilic so that water can be supplied to the photothermal layer via capillary action. Furthermore, the base layer should also be insulating so that the heat generated by the photothermal layers does not leach into the bulk water. These two objectives are often at odds with each other, as conduction of heat by water through the capillary channels is often attributed as being the primary mode of heat loss. However, given

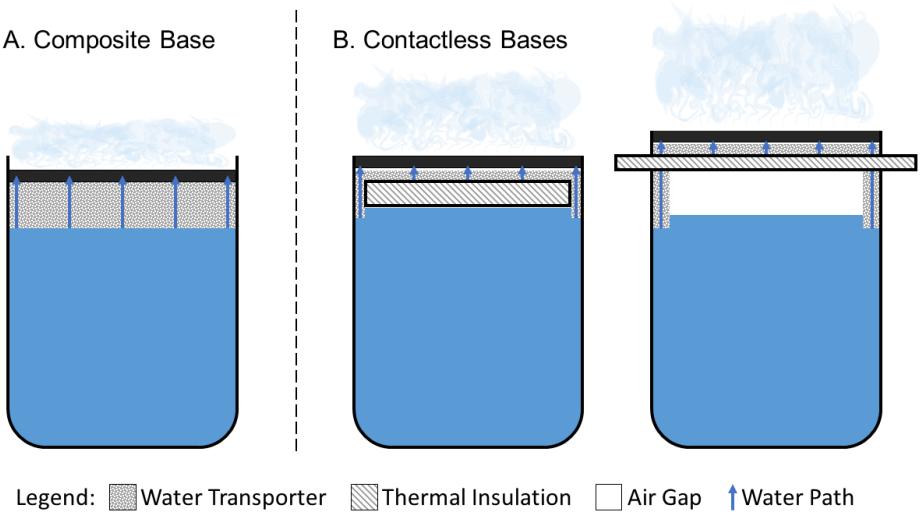

Figure 1.4: The base configurations for flat, two-dimensional ISVG materials: (A) composite base, and (B) contactless bases. The functions of these configurations are to (1) continuously supply water for evaporation, and (2) ensure heat localization in the photothermal layer of the ISVG material. Both contactless bases use an external water transporting material to wick water to the photothermal material. However, the floating contactless base (left) uses a thermal insulating material to limit direct contact between the photothermal material and the bulk water. Whereas the raised contactless base (right) primarily uses an air gap to provide insulation.

the short distances over which water needs to be wicked (on the scale of a few mm), having narrower capillary channels that prioritized heat insulation often results in improved performance.[27, 28, 29, 30] Lastly—in addition to all of the features described previously—the composite base layer is often responsible for ensuring that the ISVG material is buoyant and won't sink when saturated with water.

- *Contactless Base Layer* - The contactless base layer relies on an entirely separate material to transport water from the reservoir to the ISVG material, meaning that the ISVG material has no direct contact with the reservoir. The water transporter, or wicking material, should be hydrophilic, porous, and mechanically stable in water in order to reliably supply water by capillary action. This deviation from the composite base was first introduced by Li et al. in 2016,[31] where a cellulose coating was wrapped around polystyrene foam to supply water via a "2D water path" to their ISVG material. In this work, the ISVG material is essentially a standalone photothermal layer placed in direct contact with the cellulose coating responsible for transporting water. Meanwhile, the polystyrene provides both insulation for heat localization and buoyancy to keep the entire system afloat. While often structurally more complex, the contactless base layer eliminates the tradeoff between water supply and heat localization, and traditionally achieves higher solar-vapor conversion efficiencies than the composite base layer.

The explosion of interest in this field since 2014 can largely be attributed to the relatively low bar for materials to demonstrate the phenomenon of ISVG. As long as a material is (1) porous and light-absorbing, (2) able to localize heat to the evaporative interface, and (3) capable of passively supplying water to this evaporative interface, it is likely to be able to demonstrate ISVG at a decently high efficiency. Furthermore, while nanomaterials have helped spark renewed interest in solar desalination,[32] they do not appear to be a prerequisite for ISVG, with the simple carbonization of abundant materials—like wood,[33] mushrooms,[34] and even cattle manure(!)[35]—being sufficient to synthesize ISVG materials. The desire to continue searching for new materials capable of ISVG persists in the field, although much of these efforts have shifted away from focusing on flat, 2D-ISVG materials and onto more structurally complex 3D-ISVG materials, as will be discussed in the subsequent section of *Enhancing Evaporative Throughput (2018 - Present)*.

Maximizing Energy Efficiency (2017 - 2020)

Solar-vapor conversion efficiency, or evaporation efficiency, has been the primary metric by which various ISVG materials could be compared. Traditionally, the solar-vapor conversion efficiency may be calculated by the following expression (Equation 1.1):

$$\eta_{evap} = \frac{\dot{m}_{evap}^{net}(h_{LV} + c_p \Delta T)}{A_{evap} I_i} \tag{1.1}$$

Where the terms are defined as follows:

- $\dot{m}_{evap}^{net}$ is the difference between the mass flow rates under light conditions ($\dot{m}_{evap}^{light}$) and dark conditions ($\dot{m}_{evap}^{dark}$) $[kg\ s^{-1}]$.
- h_{LV} is the enthalpy of vaporization $[kJ\ kg^{-1}]$.
- c_p is the specific heat associated with heating water before evaporation $[kJ\ kg^{-1}\ K^{-1}]$.
- ΔT is the water temperature difference between the reservoir and the evaporative interface $[K]$.
- A_{evap} is the area of the evaporative interface $[m^2]$.
- I_i is the light intensity, typically under 1-sun conditions ($1kW\ m^{-2}$) $[kW\ m^{-2}]$.

It should be noted that this metric is not without its flaws. For example, the specific heating term—generally assumed to be the temperature difference between the bulk water and the evaporative interface—is often neglected for simplicity (typically introducing $\sim$3% error). Furthermore, the irradiation of sunlight often has unintended auxiliary effects on the experimental conditions (e.g. the heating of the surrounding environment), which means that subtracting out $\dot{m}_{dark}$ would not adequately account for all of the environmental factors that contribute to evaporation aside from sunlight. Lastly, this formulation assumes that the

ISVG material is perfectly flat, meaning that side surfaces or 3D structures do not meaningfully contribute to evaporation. However, despite these shortcomings, many researchers have pursued "record high" solar-vapor conversion efficiencies, with Liu, Z. et al. achieving 88.6% efficiency in 2017,[36] Liu, P. et al. achieving 91.3% efficiency in 2018,[37] and Hong et al. reporting over 100% later in 2018.[38]

To better understand whether evaporation efficiencies exceeding 100% are possible, it can be helpful to calculate the maximum net evaporative flux ($J_{evap}^{net} = \dot{m}_{evap}^{net}/A_{evap}$) by rearranging Equation 1.1 to solve for J_{evap}^{net} (Equation 1.2):

$$J_{evap}^{net} = \frac{m_{evap}^{net}}{A_{evap}} = \frac{\eta_{evap} I_0}{h_{LV} + c_p \Delta T} \tag{1.2}$$

Setting η_{evap} to 100%, and assuming typical experimental conditions, the maximum net evaporative flux is approximately 1.47 $kg\ m^{-2}\ h^{-1}$.[39] While it is likely that the solar-vapor conversion efficiency for some ISVG materials was being overestimated due to a lack of understanding about the assumptions and shortcomings associated with Equation 1.1, a class of ISVG materials began to emerge that offered a new explanation for how net evaporative flux rates exceeding 1.47 $kg\ m^{-2}\ h^{-1}$ were possible.

Most of these energy analyses were performed with hydrogel as the ISVG material. Hydrogels are a class of hydrophilic polymeric materials that are capable of holding large amounts of water within their three-dimensional structure without dissolving.[40] The characteristically high specific surface of hydrogels—the total surface area per unit mass of material—allows for extremely high contact between the material and the water. As a result, water within hydrogels can be found in in three different states: (1) free water, (2) intermediate water, and (3) bound water.[41, 42, 43, 44] Free water refers to water molecules that behave like bulk water, with no association to the hydrogel surface. Bound water refers to water molecules that are strongly interacting with the polar functional groups of the hydrogel, aligning themselves to be in direct contact with the surface. However, what makes hydrogels interesting for ISVG is the relatively high presence of intermediate water. Intermediate water refers to water molecules that are weakly interacting with the hydrogel surface. Where free water molecules are able to form up to four hydrogen bonds with adjacent water molecules (resulting in the high vaporization enthalpy of bulk water) and bound water molecules form even stronger hydrogen bonds with hydrophilic moieties of the hydrogel (which would require even more energy to vaporize), intermediate water molecules cannot form the same number of hydrogen bonds as free water due to their weak interactions with the hydrogel surface but are prevented from forming stronger hydrogen bonds with the surface because of the presence of bound water. As a result, intermediate water within the hydrogel network requires less energy than bulk water to break hydrogens and transition from a liquid state to a vapor state.[45, 46, 47, 48] Moreover, it was posited that the unique interactions between hydrogels and confined water promoted the evaporation of water clusters.[49] Known as the water clus-

ter theory,[50, 51] these water clusters—consisting of a few to tens of molecules—required less energy to evaporate because the hydrogen bonds between water molecules within the cluster didn't need to be broken for vaporization to take place (Figure 1.5).

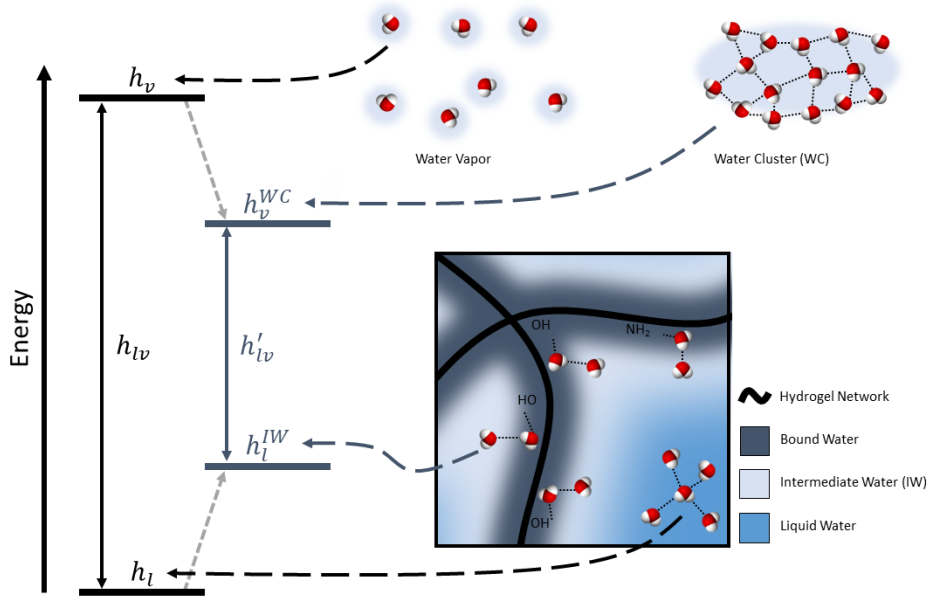

Figure 1.5: The unique properties of hydrogels increase the presence of intermediate water and enable confined heating to produce water clusters. These mechanisms are used to explain the reduction in the enthalpy of vaporization for ISVG from hydrogels.

This reduction in energy was reportedly observed in the direct measurement of the enthalpy of vaporization via differential scanning calorimetry (DSC) and thermogravimetric analysis (TGA) and used to explain how evaporative flux rates as high as 3.6 $kg\ m^{-2}\ h^{-1}$ could be achieved.[52, 49] However, these results remain controversial, with continued calls for more studies to understand the underlying mechanism and in situ observation of water cluster formation from hydrogels.[53, 54] Furthermore, this water cluster effect appears to be highly dependent on tailoring water supply through porosity[52, 49] and surface topology,[55] meaning that the modification of material properties began optimizing toward the artificial conditions of continuous sunlight at an intensity of 1 $kW\ m^{-2}$. With relatively low evaporative flux rates achievable—even at 100% solar-vapor conversion efficiency—and challenges associated with synthesizing materials capable of reducing the enthalpy of vaporization, interest in the field began to shift to utilizing energy sources beyond solar for increasing the throughput of ISVG materials.

Enhancing Evaporative Throughput (2018 - Present)

Although it is ideal for ISVG materials to operate at a high solar-vapor conversion efficiency, the ultimate goal of ISVG—especially when applying ISVG to water treatment applications—

should be the maximization of evaporative flux, or the amount of water evaporated per unit area. While these two metrics are usually complimentary—as solar-vapor conversion efficiency increases, so too will the evaporative flux—the solar-vapor conversion efficiency isolates sunlight as the sole contributor driver for evaporation. However, evaporation can take place even in the absence of sunlight. Awareness of this phenomenon is fairly widespread because it has to be accounted for in the calculation of solar-vapor conversion efficiency (Equation 1.1). The mass flow rate in dark conditions ($\dot{m}_{evap}^{dark}$) is often assumed to be a combination of material and environmental factors that contribute to evaporation, even when no light is present. The reason $\dot{m}_{evap}^{dark}$ has any contribution to evaporation, is that the mass flow rate in dark (as well as light) conditions depends on the following relation (Equation 1.3):

$$\dot{m}_{evap} = \zeta[P_w^{sat}(T_s) - (P_w^{sat}(T_a) \times RH_a)] \tag{1.3}$$

Where the terms are defined as follows:

- ζ is a conversion factor between $[kg\ s^{-1}\ kPa^{-1}]$.
- $P_w^{sat}(T_i)$ is the saturation water vapor pressure at temperature T_i $[kPa]$.
- T_i is the temperature of the ISVG surface or the ambient environment, signified by the subscript "s" and "a") respectively $[K]$.
- RH_a is the relative humidity of the ambient environment, signified by the subscript "a" [%]. It is assumed that the relative humidity at the ISVG surface (RH_s) is 100%, which is why it does not appear in Equation 1.3.

As long as there is a vapor pressure deficit—i.e., $P_w^{sat}(T_s)$ is greater than $P_w^{sat}(T_a \times RH_a)$—evaporation will take place,[56] even if this requires drawing energy from the surrounding environment. Known as evaporative cooling,[57] this phenomenon is often observed by a noticeable decrease in the surface temperature of the ISVG material. This cooling effect is balanced primarily by convective heat transfer from the surrounding environment, which is why the pressure deficit in dark conditions does not drop to 0 and $\dot{m}_{evap}^{dark}$ cannot be neglected in calculating solar-vapor conversion efficiency.

It wasn't until 2018, that this phenomenon began being applied to increase the evaporative throughput of ISVG. Song et al. investigated how the power flux exchange between the ISVG material and the environment depended on the surface temperature of the ISVG material, demonstrating that if the surface temperature of the ISVG material remained below ambient temperatures, the convective and radiative heat transfer terms could derive additional energy for evaporation from the environment.[58] Around the same time, Li et al. presented similar findings, showcasing a three-dimensional (3D)-ISVG material with significant side area that maintained a sub-ambient temperature because it was not exposed to direct sunlight, resulting in solar-vapor conversion efficiencies that far exceeded 100%[59]

(Figure 1.6).

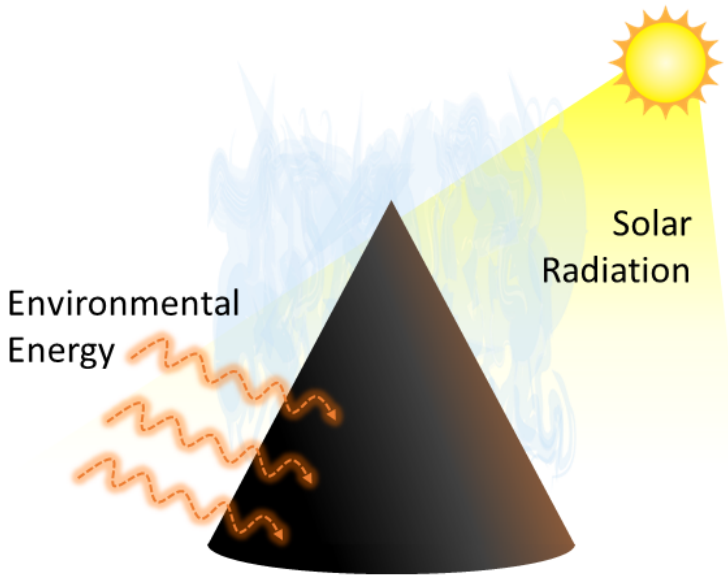

Figure 1.6: 3D-ISVG materials are better suited to take advantage of "environmental energy" because only part of their surface is exposed to solar radiation. Meanwhile, the entire 3D surface is contributing to evaporation, which causes shaded regions to cool to sub-ambient temperatures. This temperature gradient enables 3D-ISVG materials to obtain additional energy from its surrounding environment.

These findings showed that the upper limit of solar-vapor conversion efficiency could be exceeded by utilizing additional energy sources beyond sunlight, including diffuse radiation and ambient heat (sometimes referred to as "environmental energy"). This can be readily achieved by use of 3D-ISVG materials with evaporative surface areas that are not exposed to direct sunlight, allowing them to maintain sub-ambient temperatures. This realization reinvigorated interest in the field of ISVG, corresponding with another explosion of studies demonstrating the enhanced performance of 3D-ISVG materials.

1.4 Knowledge Gap & Research Opportunity

The field of Interfacial Solar Vapor Generation has grown significantly in the past 8 years. However, there are still existing knowledge gaps and opportunities for research. For example, the simple geometry of 2D-ISVG materials are ideal for analyzing the energetics of the ISVG process, revealing how mass and energy flows are linked, as well as pathways for optimization. This 2D geometry is also ideal for studying the effects of fouling—specifically inorganic scaling—and the underlying mechanisms that may degrade ISVG performance over

time. These studies will be essential, especially as ISVG materials begin to be developed for specific applications like water treatment or zero liquid discharge. Furthermore, 2D-ISVG materials using a contactless base configuration (relying on a separate water transporter for its water supply), as well as in-depth studies of hydrogels, were some of the first to explore the upper limits for capillary wicking. Understanding what factors impact this limit has become critical as the field shifts its attention to studying 3D-ISVG materials that can take advantage of "environmental energy," but require capillary action to wick water onto elevated surfaces for evaporation. Additionally, due to their significant geometric differences, there hasn't been systematic comparison between 2D- and 3D-ISVG to clearly delineate advantages of 3D-ISVG beyond higher evaporative flux. Lastly, there have only been limited attempts to develop ISVG into a desalination technology, which would require the capture and condensation of the water vapor produced by ISVG. This oversight is particularly flagrant as many reference water scarcity and safe water access as key drivers motivating their work. As the ISVG field is still relatively young, there is a tremendous opportunity to investigate how both the specific features of ISVG and the local context of an application should be accounted for in the design of a ISVG-based desalination technology.

1.5 Praxis of Development Engineering

To explore how a bench-scale process like ISVG can be thoughtfully designed into a sustainable desalination technology for a specific context, a Development Engineering approach was undertaken. Development engineering is defined as an interdisciplinary field of research and practice that combines the principles of engineering with economics, entrepreneurship, design, business, natural resources, and social science to create technology interventions in accordance with and for individuals living in low-resource settings.[60] In 2019, this led to a partnership with Maryam Karimah, who was an M.Eng. student studying Energy Systems at the University of Illinois, Urbana-Champaign at the time. Through previous work done by Maryam,[61] she had identified that a passive, solar-driven desalination device may be suitable for small-island communities in her home country of Indonesia. Specifically, Maryam suggested working with Bungin Island—a small-island community located off the coast of the Sumbawa Province in the West Nusa Tenggara Regency of Indonesia—because of their local fame as the "world's most populous island"[62] and their persistent water challenges. Conducting interviews with residents on Bungin Island to (1) understand context-specific barriers to water access and (2) incorporate local insights into preliminary designs of an ISVG-based technology, this research aims to engineer in solidarity with this community by translating local-traditional knowledge to hybridize with technocratic-bureaucratic knowledge in a creative process leading to the development of better alternatives.[63] While these efforts only amount to the preliminary steps in the Development Engineering design thinking process (Figure 1.7),[64] the research presented in this dissertation may serve as a guide for the development of other early-stage technologies also using a Development Engineering approach.

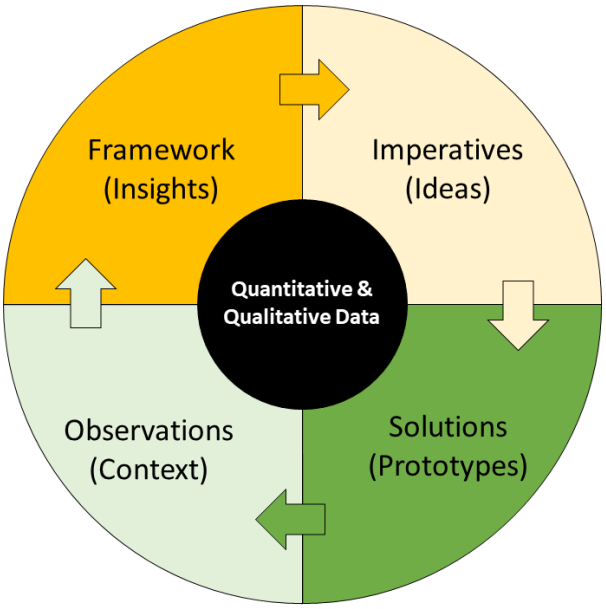

Figure 1.7: Framework for human-centered design in development engineering (adapted from Levine, Agogino & Lesniewski, 2016)[64]

1.6 Research Objectives

To address some of the research gaps presented previously, the work described in this dissertation is organized into the following chapters:

- Chapter 2: Baseline Characterization of 2D Interfacial Solar Vapor Generation
- Chapter 3: Systematic Characterization of 3D Interfacial Solar Vapor Generation
- Chapter 4: Feasibility of ISVG as a Sustainable Desalination Technology for Small-Island Communities

It should be noted that the research for this dissertation was conducted from 2016 to 2022, and the work in Chapters 2 and 3 were published in 2017[65] and 2021[66] respectively. As a result, it is helpful to situate these works within the timeline of thematic arcs discussed previously. Therefore, each chapter has been written with an introduction to provide context about the field at the time the work was being conducted, and a conclusion to highlight each work's key contributions to the field. The fourth chapter applies the principles of Development Engineering to evaluate the feasibility of an ISVG-based desalination technology to increase water access for the small-island community of Bungin Island, Indonesia. The final chapter (*Chapter 5: What's Next for ISVG*) will provide an outlook and recommendations for future directions of research for ISVG.

Chapter 2

Baseline Characterization of 2D Interfacial Solar Vapor Generation

2.1 Introduction

The following chapter is a reprint of *Synthetic Graphene Oxide Leaf for Solar Desalination with Zero Liquid Discharge*, which was published in *Environmental Science & Technology* on September 11, 2017.[65] This work describes the synthesis, characterization, and performance of a new, graphene oxide (GO)-based material capable of interfacial solar vapor generation (ISVG). Compared to other work published during this time, this work was unique in its framing of the ISVG as a bioinspired process, drawing inspiration from the transpiration of mangrove trees. Furthermore, this work was one of the first to explore the performance of interfacial solar vapor generation in high-salinity applications, like zero liquid discharge. While these aspects remain the primary contributions of this work to the field, conducting this research was foundational for advancing our understanding of the underlying mechanics behind ISVG and informed the future direction of my dissertation research.

2.2 Background

As water resources dwindle while demands soar, desalination is becoming a viable water treatment option to augment water supplies. Major advances have been made in recent years to reduce the energy consumption of desalination technologies. For example, state-of-the-art reverse osmosis (RO) membrane systems desalinate seawater with a recovery rate of 50% while consuming as little as 2 $kWh\ m^{-3}$, which is only 25% higher than the practical minimum energy requirement.[5] However, as feed water salinity increases, the energy consumption, operating pressure, and fouling/scaling potential of the membrane system increase. This issue makes it very difficult and costly to further enhance the recovery of an RO-based desalination system or operate it under high salinity conditions.[11] In the meantime, existing brine treatment technologies such as zero-liquid discharge (ZLD) systems are

particularly energy-intensive. For example, the most widely used technology, which relies on mechanical vapor compression (MVC)-based brine concentrators and crystallizers, consumes 20-25 $kWh\ m^{-3}$ and 52-66 $kWh\ m^{-3}$, respectively.[11] Recently, brine concentrators based on membrane processes such as forward osmosis[67] and membrane distillation[68] have been the subject of increasing interest due to their ability to use low-grade heat as an energy source, but it is unclear if they offer substantial advantages over existing MVC-based concentrators. Because high energy consumption remains a major barrier to ZLD, innovative approaches that are more sustainable and energy-efficient than current technologies are desirable.

Recent developments in photothermal steam generation have greatly enhanced the solar light-to-heat conversion efficiency[69] and hold immense promise for increasing the overall efficiency of desalination and water treatment. In this process, materials exhibiting mesoscopic porosity and efficient light absorption[70, 26, 71, 72, 73, 13, 74] are used for localized heat transfer from the light-absorbing material to water in pores. However, the absorption bandwidth of the plasmonic nanoparticles frequently used for absorbing light and converting it to heat under surface plasmon resonance depends on their size and shape,[75] which increase the complexity and cost of the materials.[76, 18] Additionally, plasmonic nanoparticle films tend to be fragile and thus limit their use under realistic operation conditions.

In contrast, the robust and inexpensive carbon-based materials such as graphene,[69, 77] graphene oxide (GO),[31, 78, 79] and graphite[14] are natural broadband light absorbers that are capable of absorbing about 97% of incident sunlight, making them an ideal material for sustainable solar-powered desalination. However, further development of carbon-based materials is required prior to their effective use for photothermal steam generation. This is because hydrophilic materials like GO readily swell or dissolve in water[80] and are thus unsuitable for direct water treatment without necessary modification,[81, 82, 83] while hydrophobic materials like graphene and black carbon cannot maintain good contact with water and thus have limited effectiveness in transferring heat to water.

Looking to nature, mangrove trees rely on a complex salt filtration process involving passive water transport[84] to thrive in waters with a salinity higher than that of seawater.[85] Evaporation of water from leaf stomata under solar irradiation, together with capillary action, creates a negative pressure that transports water from the growing medium into the roots, through the xylem, and eventually to the leaves. Coupled with such water transpiration, mangrove trees have developed two salt-regulating mechanisms. One is to partially exclude salt from water at their roots to minimize the accumulation of salt in their xylem and leaves, and the other is to excrete salt from glands, which are 30 μm in diameter and mostly distributed over the upper surface of mangrove leaves.[86] By mimicking the water transpiration and salt-excreting capability of mangroves, we may innovate an artificial tree system that simultaneously acts as a water purifier and a salt crystallizer, leading to a solar-powered desalination technology with ZLD capability and eliminating the two energy-intensive steps

— brine concentration and crystallization — required by the existing technologies.

This paper reports the first-phase study of a nature-inspired technology for solar-powered desalination with ZLD by using synthetic leaves to enable photothermal water evaporation. We used GO to fabricate a synthetic leaf that is stable in water and capable of generating steam with a high energy conversion efficiency. The evaporation performance of the synthetic GO leaf was evaluated in two configurations of the solar desalination system: (1) a floating configuration, in which the GO leaf floated on and was in direct contact with bulk water, and (2) a tree configuration, in which the GO leaf was lifted above and connected via a water-absorbing sheet to bulk water. Infrared thermal imaging was used to visualize the evaporation mechanism of each configuration. The effects of light intensity and water salinity on the performance of the GO leaf in the tree configuration were systematically investigated. Lastly, the durability and reusability of the GO leaf operated in high-salinity conditions were studied to assess its potential for long-term effective treatment of highly saline water.

2.3 Materials and Methods

Chemicals

Chemicals needed for GO synthesis included graphite flakes with 99% purity (Alfa Aesar, Ward Hill, MA), sodium nitrate (Sigma-Aldrich, St. Louis, MO), sulfuric acid (Sigma-Aldrich, St. Louis, MO), potassium permanganate (Fisher Scientific, Hampton, NH), and hydrogen peroxide (30% solution, Fisher Scientific, Hampton, NH). Additionally, hydrochloric acid (37% solution, Fisher Scientific, Hampton, NH) and ethanol (Koptec, King of Prussia, PA) were used as washing solutions. Fabrication of the synthetic GO leaf required triethylenetetramine (TETA) and 1,4-butanediol diglycidyl ether (BDGE) (Sigma-Aldrich, St. Louis, MO) as crosslinking agents to stabilize GO nanosheets. Cellulosic filter paper (Whatman, Maidstone, United Kingdom) was used as a substrate. Deionized water was produced by a Barnstead Smart2Pure water purification system (Thermo Fisher Scientific, Waltham, MA).

GO Nanosheet Preparation

GO nanosheets were synthesized from graphite flakes using a procedure adapted from a previous study,[83] which was based on the modified Hummers' method.[87, 88] Briefly, 5 g of powdered graphite flakes was oxidized in a mixture of 2.5 g of sodium nitrate, 115 mL of sulfuric acid, and 15 g of potassium permanganate in a 35°C water bath for 30 min, then transferred to a 98°C water bath and diluted by 230 mL of deionized water, where it remained for 15 min. After cooling for 10 min, the mixture was diluted to 700 mL and then added with 5 mL of hydrogen peroxide. The suspension was filtered using a polyethylene terephthalate fiber, and the filtrate was centrifuged at 8,000 x g for 2 h with an Avanti J-30I centrifuge

(Beckman Coulter, Indianapolis, IN). The supernatant was decanted and the precipitate was washed in successive cycles of deionized water, hydrochloric acid, and ethanol using the centrifuge until the supernatant reached pH 7. Next, the GO precipitate was freeze-dried at -50°C and under a pressure of less than 0.2 mbar in a freeze dryer (FreeZone 1, Labconco, Kansas City, MO) to obtain GO powder. The GO was then resuspended in a 20 g/L solution by sonication with a Q500 Sonicator (Qsonica, Newton, CT) in an ice bath at an amplitude of 80% for 2 h. The resulting GO suspension was purified by placing it in a dialysis bag and soaking the bag in 2000 mL deionized water, which was replaced daily for 6 days or until the water conductivity stabilized.

GO Leaf Fabrication

The synthetic GO leaf was prepared by crosslinking the GO nanosheets with TETA and BDGE.[89] As schematically illustrated in Figure 2.1, 0.5 mL of 20 g/L GO suspension was first mixed with 0.1 mL of 0.01 M sodium hydroxide in a 2 mL tube on ice. The solution was then mixed with an Analog Mini Vortexer (Fisher Scientific, Hampton, NH) for 1 min and placed back on ice. Next, 24 μL of TETA was added and the solution was vortex-mixed for 1 min and placed back on ice. Then, 65 μL of BDGE was added and the solution was vortex-mixed before placing the tube in an ice bath that was sonicated at 40% amplitude for 4 min. Two circular coupons, each with a diameter of approximately 4.5 cm, were cut from the filter paper with a circle cutter (Fiskars, Finland). The coupons were dip-coated in the GO-TETA-BDGE solution and left undisturbed at room temperature for 1 min, leading to a GO mass loading density of about 0.29 $mg\ cm^{-2}$ on the coupon. The coupons were then frozen by placing them on a plastic petri dish wrapped in aluminum foil and suspending it in liquid nitrogen for 2 min. The petri dish with the coupons was placed in a freeze dryer (Fisher Scientific, Hampton, NH) overnight at -50°C and under a pressure of less than 0.2 mbar, and then the coupons were transferred to a 100°C oven and stored for 24 h to facilitate the crosslinking reaction. After that, the coupons were soaked in deionized water for 24 h, during which the water was changed at least 5 times. Finally, the resulting GO-TETA-BDGE coupons were stored at 60°C in an Isotemp General-Purpose Heating and Drying Oven (Fisher Scientific, Hampton, NH) to remove any residual water.

GO Leaf Characterization

To investigate the stability of the synthetic GO leaf, its elemental compositions before and after solar irradiation were analyzed by X-ray photoelectron spectroscopy (XPS). To verify the light absorption capability of the GO leaf, its absorption spectrum was measured using an ASD QualitySpec Pro UV-Vis spectrophotometer with a Muglight attachment (ASD Inc., Boulder, CO). The absorption spectrum of the filter paper substrate was also collected as a control to determine light absorption enhancement by GO. The deposition of GO-TETA-BDGE onto the filter paper substrate was verified by collecting the absorption spectra with an iS50 Fourier transform infrared (FTIR) spectrometer (Thermo Fisher Scientific, Waltham,

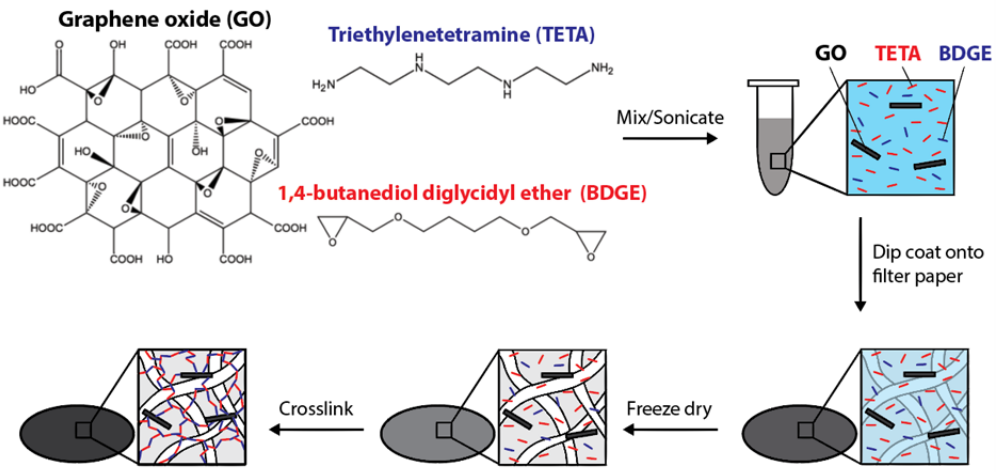

Figure 2.1: Schematic illustration for the fabrication of synthetic GO leaf.

MA). Lastly, the pore size and thickness of the GO leaf were determined by visualizing it with a Gemini Ultra-55 analytical field emission scanning electron microscope (SEM) (Zeiss, Jena, Germany).

Solar Evaporation Experiments and Evaluation

Inspired by the water transpiration process of a natural tree, a bench-scale setup was built to evaluate the solar evaporation performance of the synthetic GO leaf. As shown in Figure 2.2, the synthetic GO leaf was placed on top of a water reservoir (100 mL beaker with an inner diameter of 4.5 cm) by positioning it on a piece of polystyrene sheet. Water was transported from the bulk water to the GO leaf by capillary action through a water-absorbing sheet (Nalgene Versi-Dry Surface Protectors, Thermo Fisher Scientific, Waltham, MA). To promote good contact between the GO leaf and the water absorber, the two materials were sandwiched together using two sheets of polystyrene plastic. As a control, a floating configuration was evaluated, in which the beaker was filled with deionized water and the GO leaf was placed directly on the water surface. Furthermore, baseline tests on water evaporation in the absence of a GO leaf were conducted for the tree and floating configurations, respectively.

The evaporation experiment was started by irradiating the water in the reservoir (with or without a GO leaf installed) with artificial sunlight, which was produced by a 1,000-watt large area light source solar simulator (Spectra-Physics, Stratford, CT) and had a solar spectrum comparable to that of natural sunlight over the visible light region (Figure A.1). A P-8001 mass balance (Denver Instrument, Bohemia, NY) was placed beneath the light source of the solar simulator to record the mass of water remaining in the reservoir at 1-min intervals during irradiation cycles. The evaporation rate was then calculated as the change in the recorded mass of water normalized by the leaf area and the corresponding time interval, that is, the slope of the curve that depicted the relationship between the mass

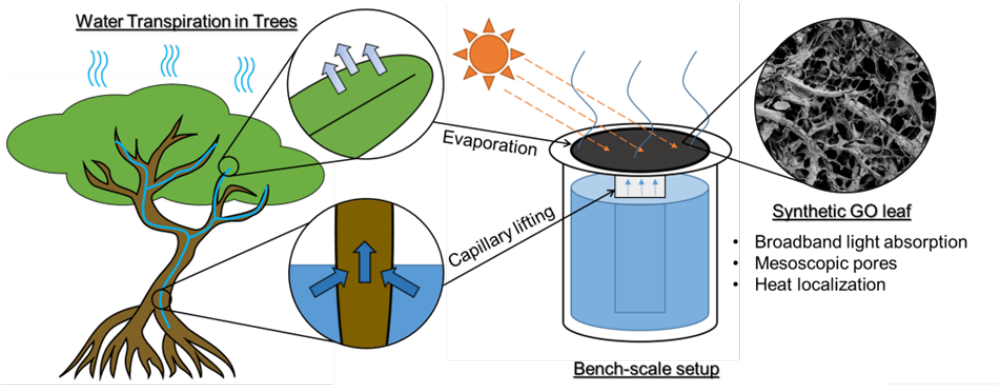

Figure 2.2: Solar evaporation through the synthetic GO leaf to mimic water transpiration in natural trees.

of water evaporated per unit leaf area and the irradiation time. The same analysis was also performed for all control experiments (where light irradiation was not applied) to obtain baseline evaporation rates in dark conditions. The light intensity and solar spectrum were obtained by an LX1330B lux meter (Precision Vision, Woodstock, IL) and an EPP 2000 radiometer (StellarNet Inc., Tampa, FL), respectively. Unless otherwise specified, each solar experiment was performed with a light intensity of 825 $W\ m^2$, which corresponds to 0.82-sun illumination since 1,000 $W\ m^2$ is often considered as the default value for one sun condition in related literature.[31] The temperature evolution was monitored by taking infrared images with a Ti100 infrared camera (Fluke Corporation, Everett, WA) before irradiation and at regular time intervals during irradiation.

Solar Desalination Performance Evaluation

The stabilized evaporation rates for the tree configuration were determined by running the evaporation experiments for at least 5 h using bulk NaCl solutions of different initial salinities (1.7, 3.5, 5.25, and 7 wt.%), representing 0.5, 1.0, 1.5, and 2.0 times the concentration (3.5 wt.%) of NaCl in seawater. The crystal formation on the GO leaf surface was examined by SEM when the salinity of the solution remaining in the reservoir reached a certain level (∼8.8 wt.% NaCl). The long-term evaporation performance of the GO leaf was examined using 15 wt.% NaCl solution (∼4 times seawater salinity), and the effects of salt crystals formed over the leaf surface on temperature distribution and evaporation performance were investigated. The reusability of the material was assessed by scraping off the accumulated salt crystals from the GO leaf using a metal scoopula and briefly soaking it in deionized water for 5 min before reusing the cleaned GO leaf in another evaporation cycle.

2.4 Results and Discussion

Properties of GO Leaf

GO was selected as the solar absorber in this study because of its photothermal capability, hydrophilicity, and low cost. The TETA-BDGE-crosslinked GO nanosheets were deposited across the whole depth of the filter paper, as indicated by the change of color from white to black on both top and bottom surfaces of the filter paper after GO deposition (Figure A.2). Such a fully interwoven structure led to excellent stability (to avoid dissolving in water) and durability (to resist mechanical damages), as the GO leaf did not exhibit signs of cracking or tearing after repeated folding and unfolding in either dry or wet/humid condition (Figure A.3). Furthermore, XPS analysis (Figure A.4) revealed that the changes in elemental composition of the GO leaf due to sunlight irradiation were small.

A major advantage of the GO leaf is its broadband light absorption capability, which is critical for enhancing the overall energy efficiency of solar evaporation. As shown in Figure 2.3-A, the light absorption of the GO leaf was consistently higher than that of the filter paper substrate. Absorption throughout the visible and near infrared regions of the electromagnetic spectrum is attributable to both the broad absorption spectrum and surface roughness (which enhances internal light scattering) of GO.[31] Such mechanisms for photothermal conversion are advantageous over plasmonic heating, which requires noble metals (e.g., gold and silver) and complex material processing to convert narrowband to broadband light absorption. The composition of the GO leaf was evaluated by FTIR. As shown in Figure 2.3-B, the FTIR spectrum of the GO leaf exhibits peaks at 1204, 1566, 1645, and 1724 cm^{-1} that are not present in the spectrum of the filter paper, indicating the existence of epoxy, carboxylate, amide, and ester groups, respectively, in the GO leaf. It is believed that the carboxylate and, to a lesser extent, epoxy and ester peaks were likely contributed by GO, the amide peak was solely due to TETA, and the epoxy and ester peaks were primarily associated with BDGE. The surface (Figure 2,3-C,D) and cross-section (Figure 2.3-E,F) SEM images reveal that the fabricated GO leaf was around 170-μm-thick and had an extremely porous structure, both external and internal, created by the crosslinked GO nanosheets on the cellulosic fibers of the filter paper substrate.

The pores of the 3D microporous network of the GO leaf had a planar diameter in the range of 10 to 30 μm, similar to the size of stomatal openings in natural tree leaves. However, unlike stomata, which mainly serve as gates to regulate the escape of water vapor,[90, 91] the fixed-sized openings of the GO leaf contributed to water evaporation in three different ways. First, the presence of these pores increased the effective surface area and thus enhanced the overall rate of evaporation. Second, because water diffuses much faster near the edge of a pore than at its center, a phenomenon known as the perimeter effect,[92] the rate of pore evaporation was higher than that of bulk water evaporation. Third, the porous GO structure enabled effective heat localization by directly transferring the heat generated

by absorbed light to water within the pores.

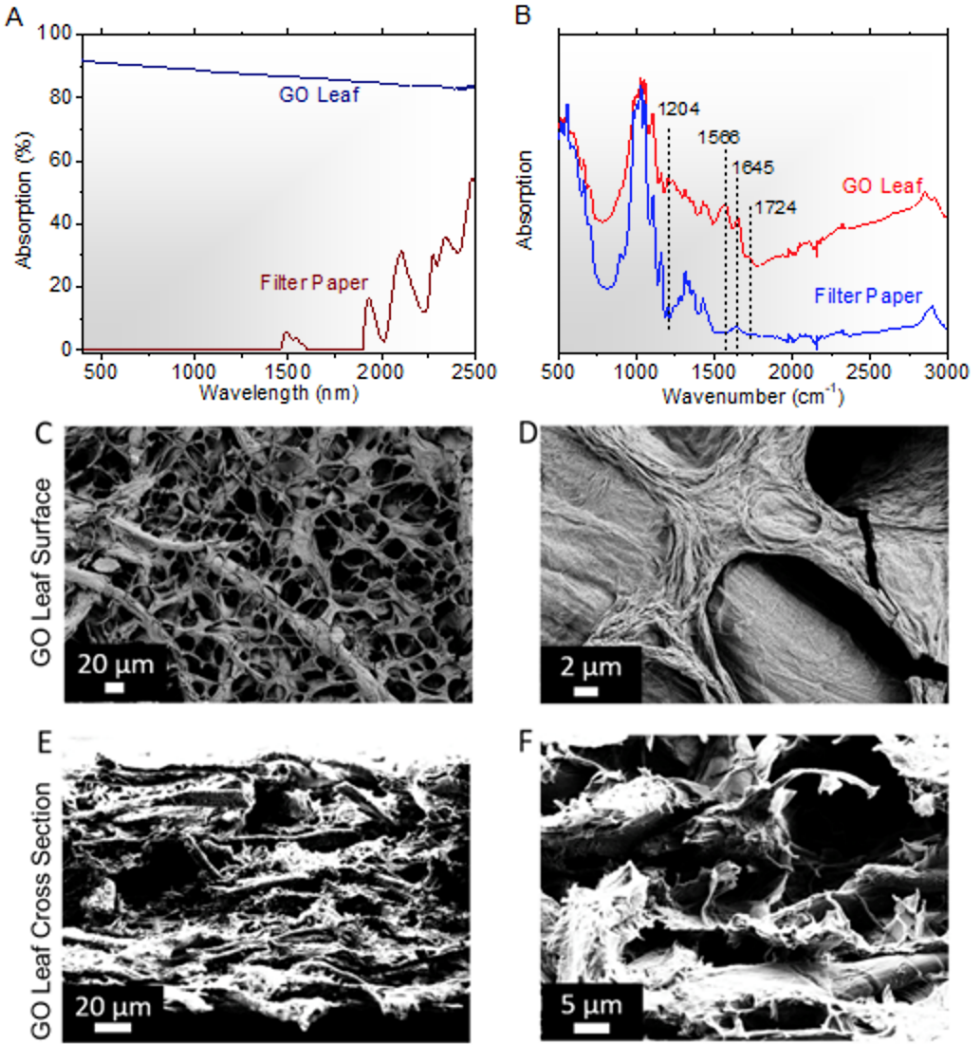

Figure 2.3: Characterization of the synthetic GO leaf. (A) Absorption spectra and (B) FTIR spectra of the filter paper substrate and GO leaf; SEM images with different magnifications of (C and D) the surface morphology and (E and F) cross section of the GO leaf.

Heat Localization Enabled by Tree Configuration

The temperature evolutions of the GO leaf in the floating configuration (where the GO leaf was in direct contact with bulk water) and the tree configuration (where the GO leaf was lifted above and insulated from bulk water, as assembled in Figure A.5) were compared to understand how the GO leaf enhanced the water evaporation through heat localization. The GO leaf heated up much faster than its control in the floating configuration (Figure 2.4-A,B) as well as in the tree configuration (Figure 2.4-C,D). This is because the photothermal

properties of the GO leaf facilitated more light to be converted into heat, increasing the temperature at the evaporation interface. The heat generated in the floating configuration was partly transferred into the bulk water, as evidenced by an increase in the temperature of bulk water, thereby reducing the amount of heat available for evaporation in the GO leaf. In contrast, the bulk water did not significantly heat up in the tree configuration, indicating that heat was mainly retained in the pores of the GO leaf. Note that compared with the floating configuration, the tree configuration only led to a small increase of temperature at the evaporation surface. This is because, although the tree configuration improved heat localization, the corresponding higher rate of evaporation required more energy to vaporize additional water, thus limiting the amount of heat available for increasing the temperature of the GO leaf.

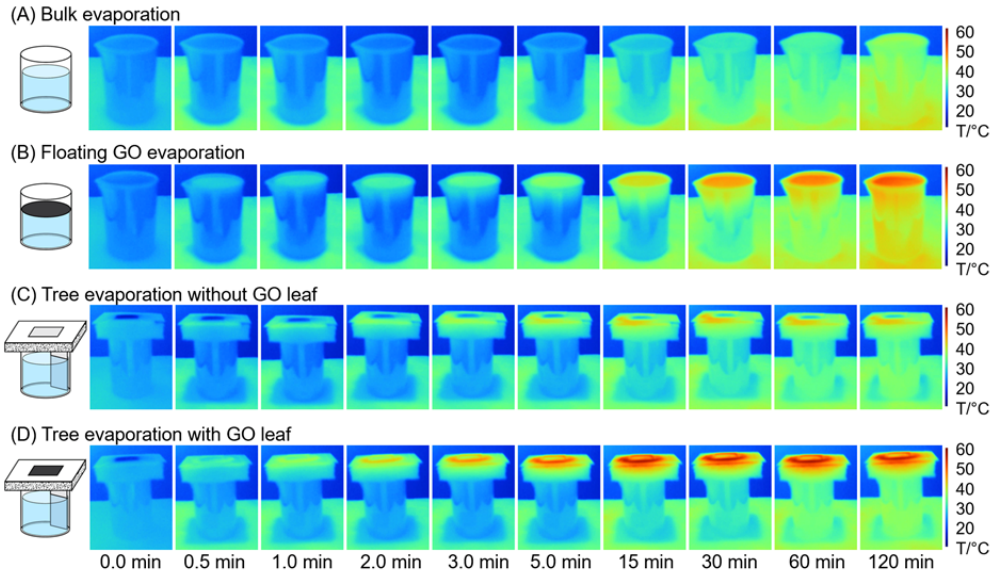

Figure 2.4: Temperature evolution during water evaporation in different configurations: (A) bulk water as a control, (B) GO leaf floating on water surface, (C) tree configuration without GO leaf as a control, and (D) tree configuration with GO leaf.

Solar Evaporation Performance

The evaporation performances of both floating and tree configurations were examined. As shown in Figure 2.5-A, the water evaporation rate (calculated as the slope of the curve) of the GO leaf in the floating configuration was 1.1 LMH, marking a 59% increase from 0.70 LMH of its control experiment without GO leaf. Similarly, the evaporation rate of the GO leaf in the tree configuration was 2.0 LMH, which more than doubled the 0.88 LMH of its control without GO leaf.

The evaporation efficiency (i.e., light-to-vapor energy conversion efficiency), as calculated

in the Appendix A with baseline dark-condition corrections (Figure A.6), increased from 20% for bulk water to 54% for the GO leaf in the floating configuration and 78% for the GO leaf in the tree configuration. While both configurations relied on the photothermal properties of the GO leaf to convert sunlight into usable heat, the evaporation rate for the tree configuration was higher due to better heat localization at the evaporation surface. Figure 2.5-B illustrates the variation in the relative proportions of the total solar energy having different ultimate fates — loss by light reflection and transmission, loss to the surrounding environment through heat transport (i.e., conduction, radiation, and convection), and latent heat for phase change (evaporation) — among different configurations under 0.82-sun illumination. Detailed calculation of the energy distribution is explained in Appendix A. For both bulk water and tree configurations without a GO leaf, most (72-83%) of the energy from the incident light was lost due to light reflection and transmission. In contrast, adding the GO leaf in both floating and tree configurations made it possible to capture significantly more solar energy while reducing the amount of energy lost as reflected/transmitted light to 10%. Besides, the tree configuration with a GO leaf was very energy-efficient, viewing that only 12% of the total energy was lost as heat into the environment. In contrast, the floating GO leaf configuration lost 36% of the total energy to the bulk water that had a direct contact with the GO leaf. Therefore, a key advantage of the tree configuration over the floating configuration is that more heat can be locally trapped by the lifted GO leaf due to the air insulation between the GO leaf and bulk water, thus significantly minimizing the amount of heat energy lost into the aqueous environment.

Our data agreed well with literature data in revealing the importance of having an insulation layer between the bulk water and evaporation surface to enhance the overall light-to-vapor energy conversion efficiency. Our tree configuration with a GO leaf had an efficiency of 78% under 0.82 sun, which is comparable to the efficiency (80-85% under one sun) of other recently reported carbon-based evaporators with good insulation.[69, 77, 31, 78, 79, 14] Some other biological and engineered materials (e.g., carbonized mushroom, two-dimensional MXene) with good photothermal properties and proper insulation also led to a relatively high efficiency ($\sim$80%).[34, 93] However, when an effective insulation layer was absent, a much lower efficiency (50-64%) was reported for GO,[31] plasmonic material,[74, 18] and other materials.[94] Note that the energy conversion efficiency in general increases with increasing light intensity. For example, efficiencies as high as 90-94% were achieved by GO[77] and plasmonic material-based systems[74, 18] when subjected to a much higher light intensity (>4 suns).

Additional characterization of the GO leaf in a tree configuration showed a positive correlation between the evaporation rate and light intensity. As plotted in Figure 2.5-C, the evaporation rate increased approximately linearly with light intensity and nearly doubled as the light intensity increased from 450 to 900 $W\ m^2$. Note that other environmental factors such as humidity, temperature, and wind speed also likely affect the evaporation rate.[95] Research on the effects of these factors is warranted in the future but is beyond the scope of

the present study.

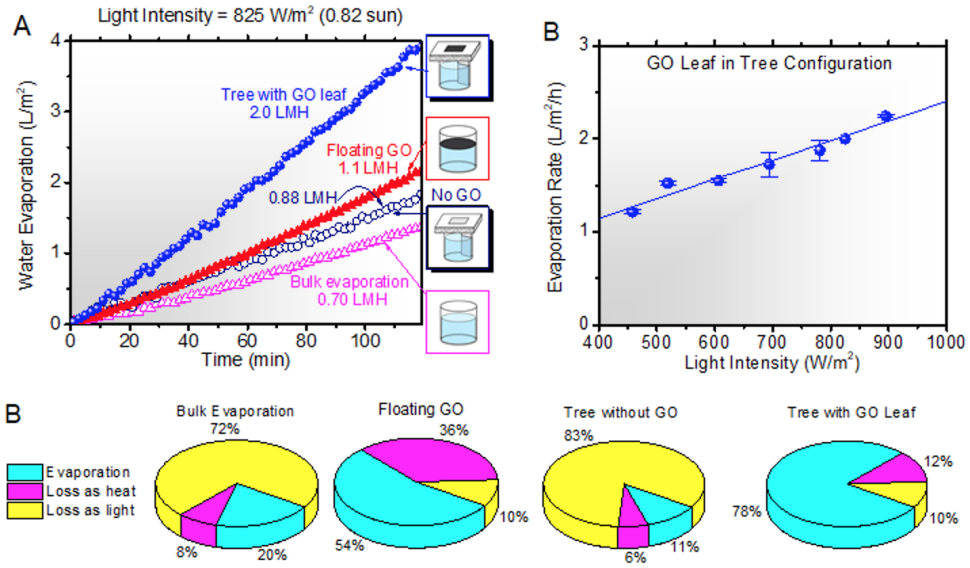

Figure 2.5: Solar evaporation enhanced by the GO leaf: (A) the water evaporation, with the slope denoting the evaporation rate in L/m2/h (LMH), for each configuration; (B) the fate of solar energy for each configuration; (C) the effect of light intensity on the evaporation rate of the GO leaf in the tree configuration.

Solar Desalination Performance

The GO leaf was tested in a tree configuration under the 0.82-sun condition (825 $W\ m^{-2}$) and at different salinity levels. It is observed in Figure 2.6-A that the stabilized evaporation rate of the GO leaf was inversely proportional to water salinity. Specifically, the evaporation rate decreased from 2.0 LMH for fresh (i.e., zero-salinity) water to 0.71 LMH for water with an initial salinity of 7.0% NaCl, twice that of seawater. As salinity further increased, the evaporation rate appeared to decrease much more slowly and reached ∼0.5 LMH at a salinity level of 15 wt.% NaCl. The evaporation rate at each salinity typically decreased initially and stabilized within the first hour, as demonstrated in Figure 2.6-B using the salinity level of 15% as an example. Therefore, compared with the thick accumulation of salt crystals on the GO leaf, the initial formation of salt crystals, which took place within the pores and grew heterogeneously at random locations on the surface, likely played an important role in reducing the evaporation rate. In order to study the structure of salt crystals initially formed on GO surface before it was fully covered by a thick crystal layer, we used SEM to observe the crystal-free regions of the GO leaf with naked eyes after crystals started to accumulate in other regions, using NaCl solutions with initial salinity levels of 1.75% (Figure 2.6-C), 3.5% (Figure A.7), 5.25% (Figure A.7), and 7.0% (Figure 2.6-D), respectively. As expected, an increase in salinity led to more severe crystal formation and thus narrower open

pores of the GO leaf, decreasing the rates of water transport and evaporation (Figure 2.6-A).

It is observed in Figure 2.6-D that open pores still existed in the GO leaf even after it had experienced significant crystal build-up at high salinity. According to the Kelvin equation,[96] evaporation would occur more rapidly on the convex/flat surface of salt crystals formed over the GO leaf surface than on the concave water surface formed within the pores. We hypothesize that such preferential evaporation helped the pores of the GO leaf to remain open as crystals kept growing on the already-formed ones, thereby enabling water evaporation to continue despite salt crystal accumulation on the leaf surface. Similar preferential sites for salt accumulation was also observed in the process of water evaporation from porous media.[97]

It is interesting to note that after the initial pore blockage the additional salt accumulation on the GO leaf surface did not appear to further reduce the evaporation rate. As shown in Figure 2.6-B, the water evaporation vs. time curve has an almost constant slope during a 5-day test (except the first hour) at a very high salinity of 15 wt.% NaCl. The time-lapse snapshots in Figure 2.6-E demonstrate that crystals gradually grew on the GO leaf surface during the 5-day test, with the overall thickness reaching more than 1 cm by day 5. A time-lapse video documenting the 5-day test is available online.[65] In addition, the formation of a thick crystal layer did not significantly decrease the light absorption efficiency of the GO leaf; on the contrary, thermal images (Figure 2.6-F) show that the surface temperature of the GO leaf during the evaporation experiment using high-salinity (15%) water was actually higher than that using deionized water (Figure 2.4-D), indicating that a large portion of light was still able to transmit through the salt crystals accumulated on the GO leaf. Note that the evaporation rate was likely affected by a number of factors, including the surface temperature, pore size, effective evaporation area, and capillary action within the leaf structure, some of which may have conflicting effects on evaporation on the GO leaf. It is suspected that capillary action within the GO leaf might quickly (say, within hours) reach a steady state and become the most limiting factor during subsequent evaporation. Future work to fully understand such effects is needed.

Although the salt accumulation did not noticeably affect the water evaporation rate in the present study, the salt build-up on the GO leaf surface could eventually damage the overall solar desalination system due to, for example, the added weight. To resolve this issue, the accumulated salt should be cleaned regularly during the evaporation operation—salt crystals were scraped off from the GO leaf using a metal scoopula and then the GO leaf was soaked in deionized water for 5 min (Figure A.8-A). In this way, the pristine state of the GO leaf was restored without apparent signs of physical damage or performance deterioration (Figure A.8-B). Note that the accumulation of inorganic (e.g., gypsum) and organic (e.g., natural organic matter, protein and other macromolecules) species on the GO leaf could also affect the evaporation performance. Evaluation of such effects is necessary in the future toward further development of the present solar desalination technology.

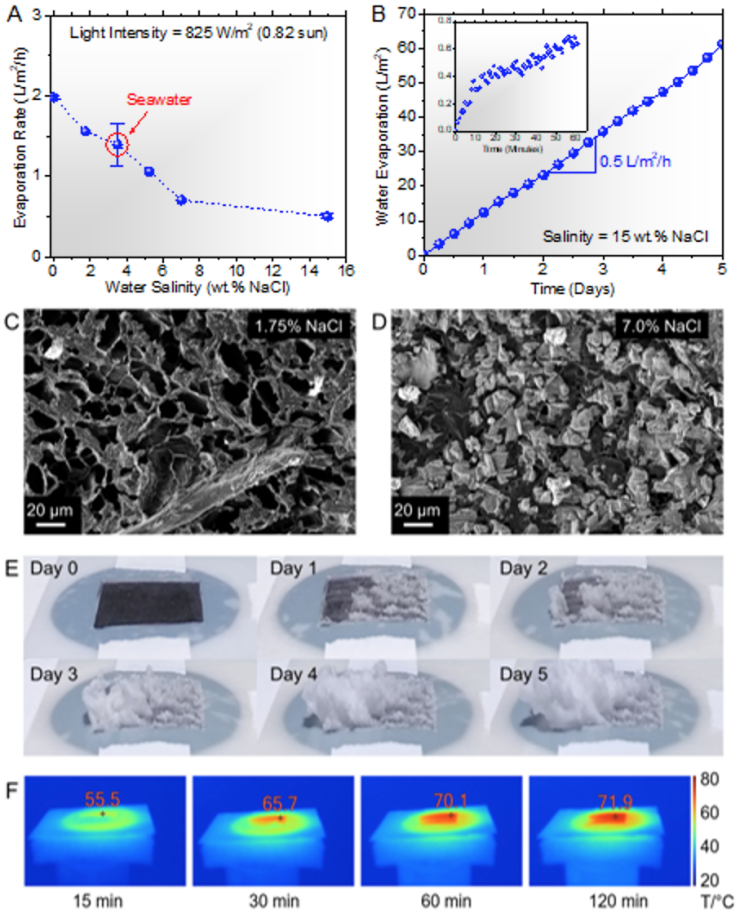

Figure 2.6: Solar desalination by the GO leaf in a tree configuration. (A) Effect of water salinity on the stabilized evaporation rate; (B) 5-day evaporation performance of the GO leaf using 15 wt.% NaCl solution; (C and D) SEM images of the GO leaf surface after salt crystallization occurred with 1.75 and 7 wt.% NaCl solutions respectively ; (E) Time-lapse snapshots of salt crystal formation on the GO leaf surface during a 5-day evaporation experiment using 15 wt.% NaCl solution; and (F) thermal images revealing the effect of salt accumulation over the GO leaf surface on temperature evolution, using 15 wt.% NaCl solution.

Outlook of Artificial Tree for Solar Desalination and Wastewater Treatment with ZLD

An artificial tree system consisting of multiple synthetic GO leaves will be the next-phase experimental configuration toward scaling up the present single-leaf device. We expect that the multi-leaf configuration will make the solar desalination system more compact so as to better withstand real-world environmental stressors. Besides, the multi-leaf configuration will increase the so-called leaf area index (LAI), which is defined as the ratio of total one-

sided leaf area to canopy footprint area.[98] An artificial tree with a larger LAI will not only enable more efficient use of solar light by absorbing scattered/transmitted light and secondary irradiation, but also enhance convective evaporation by increasing the available leaf surface area. In the meantime, future research is warranted to optimize the structure and properties of the GO leaf for maximum utilization of convective evaporation (in addition to direct solar evaporation) along with the capillary force to take up and transport water. Eventually, water vapor generated by synthetic leaves will be collected and condensed to produce clean water. Note that the latent heat released from vapor condensation could be recovered and reused for evaporation, further increasing the overall energy efficiency.

The direct crystallization of salt on synthetic leaves offers an unprecedented opportunity for brine disposal with ZLD. The unique capability of natural mangrove trees to predominantly excrete NaCl crystals on leaf surface, which results in a buildup of magnesium and potassium ions in leaves,[86] suggests the possibility of salt separation and purification during crystallization. In addition to salt excretion on synthetic leaves via water evaporation, salt exclusion at synthetic roots made of semipermeable membranes can be implemented to enhance the overall desalination performance, leading to a complete tree configuration. We expect that the artificial tree system will be capable of treating high-salinity waters and recovering salts using sunlight as the sole energy source. Considering the scale-up feasibility and low fabrication cost of the synthetic GO leaf, the artificial tree system offers a great potential for important applications such as off-grid, robust, and economical wastewater treatment and seawater desalination with minimum environmental impacts.

2.5 Conclusion

This work highlighted the importance of thermal management for ISVG. Under solar conditions of 825 $W\ m^{-2}$, the GO leaf floating directly on the water had an evaporative flux of 1.1 $kg\ m^{-2}\ h^{-1}$, with a corresponding solar-vapor conversion efficiency of 54%. Meanwhile, the GO leaf lifted above the water in a tree-like configuration achieved an evaporative flux of 2.0 $kg\ m^{-2}\ h^{-1}$ with an efficiency of 78%. Furthermore, the GO leaf displayed resilience in high-salinity conditions of 15 wt % as NaCl. Despite the severe accumulation of salt crystals on the GO leaf surface, the evaporative flux remained constant and could be easily restored to its pristine condition by simply scraping off salt crystals from its surface and rinsing with water.

Beyond these key findings, this work was formative in shaping the future direction of this research. While achieving an evaporative flux of 2.0 $kg\ m^{-2}\ h^{-1}$ and a solar-vapor conversion efficiency of 78% would still be considered impressive, this already high value for efficiency highlights the relatively low upper limit of evaporative flux. For example, even if the GO leaf were able to achieve 100% solar conversion efficiency, the evaporative flux rate would only be 2.6 $kg\ m^{-2}\ h^{-1}$, which is too low for most applications. However, the tree-like configuration relied on a water-wicking material to supply water from the reservoir to the GO leaf. While

this wicking material was able to improve heat localization by decoupling the evaporative interface from the air-water interface, being able to passively wick water against the force of gravity adds a height dimension to ISVG that could be used to increase the total surface area available for evaporation.

Chapter 3

Systematic Characterization of 3D Interfacial Solar Vapor Generation

3.1 Introduction

The following chapter is a reprint of *Interfacial Solar Evaporation by a 3D Graphene Oxide Stalk for Highly Concentrated Brine Treatment*, which was published in *Environmental Science & Technology* on November 5, 2021.[66] While a wide range of 3D-ISVG materials were being studied during this time, there had been little effort to categorize these 3D-ISVG materials so that the performance between materials could be properly compared and specific advantages of 3D-ISVG be identified. As a response, this publication set out to establish Evaporation Area Index (EAI)—the ratio of total surface area for evaporation to projected ground area—as a metric to compare various 3D-ISVG structures. Through a systematic comparison between graphene oxide (GO)-based, 2D- and 3D-ISVG materials, this work highlighted the distinct advantages of 3D-ISVG with respect to solar utilization, wind enhancement, and resilience to mineral scaling. While the impact of this work on the field remains to be seen, it is these unique advantages of 3D-ISVG that should be incorporated into future technology development for ISVG.

3.2 Background

Global water security is being threatened by rapidly increasing water demand, primarily driven by population growth.[2] Concurrently, overexploitation, pollution, and climate change are decreasing the availability of traditional water resources,[3] which is estimated to cause an additional 1.8 billion people to fall into water stress in the next 30 years.[99] Expanding to alternative water supplies typically involves advanced treatment, often by reverse osmosis (RO). However, RO requires large capital investment, technical expertise, established supply chains, and a reliable supply of high-grade energy to operate.[100] Furthermore, brine produced by RO has to be properly managed, which severely limits where

RO can be affordably implemented, especially when ocean disposal is impractical.[101]

Interfacial solar vapor generation is an emerging approach to sustainably desalinate water using sunlight, while being capable of achieving zero liquid discharge.[65, 102] In recent literature, interfacial solar evaporation is most often achieved using flat, two-dimensional (2D) materials that float at the air-water interface, where water is wicked into the material's porous structure, photothermally heated by sunlight, and efficiently evaporated.[14] Although optimization of material properties, heat localization, and water replenishment rates have led to extremely high solar-vapor conversion efficiencies, evaporative fluxes from 2D evaporators are still low, typically between 1.5 to 3.0 $kg\ m^{-2}\ h^{-1}$,[28, 103, 54, 49] which would result in a relatively large footprint.

Recently, researchers have proposed the use of 3D evaporators to increase the water production performance.[104] As the name suggests, these 3D structures utilize capillary pumping to supply water to additional surfaces for evaporation.[105] This enables 3D evaporator to achieve evaporation area index (EAI) values (ratio of total area available for evaporation relative to projected ground area) that are greater than 1. Figure 3.1-A summarizes some 3D geometries that have been reported in the literature, including hierarchical structures that contain microscopic 3D features to increase the EAI to around 1.2[106, 107] curved and folded 2D sheets that lead to an increased EAI of around 1.5,[58, 38, 108] 2D sheets that were intentionally converted into 3D geometries to obtain an EAI up to 3 by means of cutting and pasting,[79, 109, 110] and more recently bio-inspired[34, 111, 112] and other 3D evaporators[113, 114, 115] structures that result in EAI values of 5-15. The evaporative water flux of these 3D evaporators were higher than most 2D counterparts, but they have remained less than 5 $kg\ m^{-2}\ h^{-1}$, with only a few 3D evaporators achieving the higher EAI values[116, 117] that are needed to make this approach attractive in practice. Therefore, there is a need to develop an inexpensive, simple 3D evaporator that can achieve a substantially higher EAI that will result in the necessary improvement in water flux.

To address this challenge, we analyzed three geometries (i.e., dome, cone, and cylinder) through mathematical modeling to facilitate the design of 3D evaporators. After finding the optimal geometry being a cylinder, we synthesized a cylindrical, 3D GO stalk that effectively absorbs solar light and takes full advantage of capillary pumping to achieve significant increases in EAI and evaporative surface area. We investigated this 3D design in comparison with a 2D system to evaluate the potential advantages of 3D evaporators, including water flux enhancement, omni-directional light absorption, utilization of wind-induced convection, and scaling resistance with high-salinity brine. These findings are especially relevant as research efforts transition from material synthesis to technology design, with the 3D GO stalk showing promise to reduce the spatial footprint of brine evaporation and potentially achieve zero-liquid-discharge (ZLD).

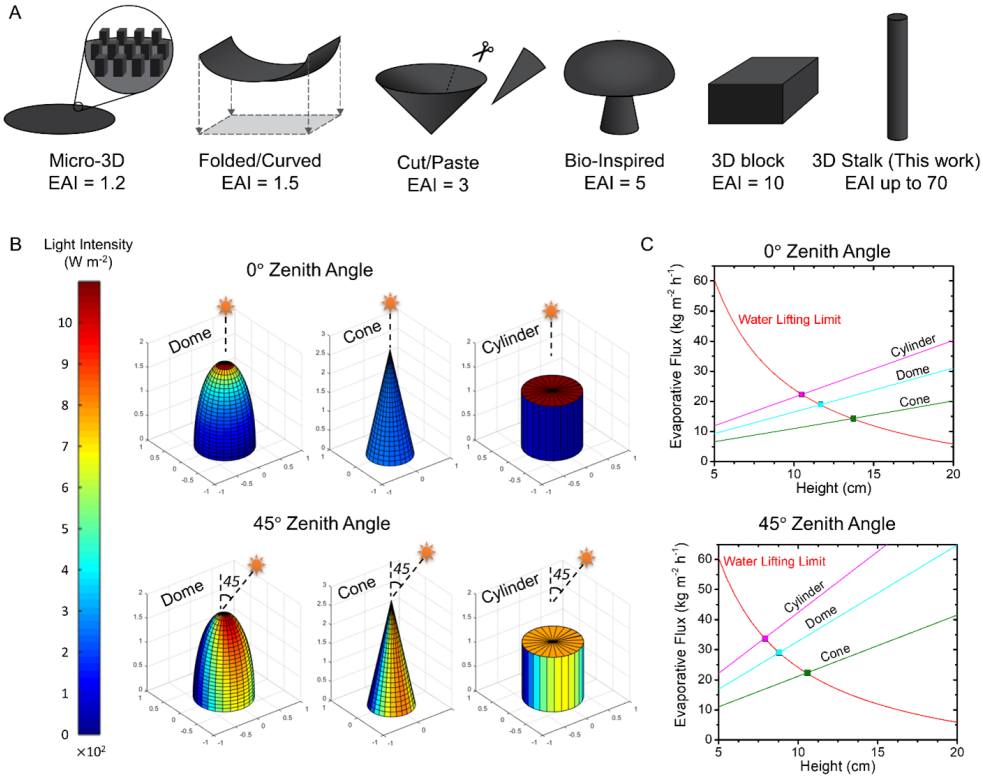

Figure 3.1: Comparison of different 3D evaporator geometries, and their corresponding EAI values, light absorption, and water evaporative flux. A) Comparison of 3D evaporator geometries reported in the literature[118, 119, 120, 121, 122, 123, 124, 125, 126, 127, 128, 129, 79, 130] and their corresponding EAI values. B) Light intensity irradiated onto three 3D geometries (cone, dome, and cylinder) with solar zenith angles of 0° (noon position) and 45° under 1-sun conditions. C) Comparison of the projected evaporative flux of the three different 3D geometries with a set projected area and increasing height. The maximum rate achievable depends on how rapidly water can be replenished to the highest evaporative interface, denoted as the "Water Lifting Limit". The evaporative flux of each 3D evaporators will depend on the incident angle of solar radiation, therefore two solar zenith angles, 0° (top) and 45° (bottom), have been studied.

3.3 Materials and Methods

Light Intensity Analysis and Flux Prediction to Obtain Optimal Geometry

To determine the best 3D geometry to pursue, the evaporative performance of the three 3D geometries illustrated in Figure 3.1-B were investigated as a function of height. The

diameter of the projected area (base) of all three shapes was held constant at 1 cm, while the height was varied from 5 to 20 cm. Using MATLAB, the 3D geometries were constructed by rendering the 3D surfaces into 2D subunits, each with a specific direction and inclination angle (Figures B.1-A and B.1-B). At a light incident angle (Zenith Angle) of 0° or 45°, the light intensity being irradiated onto the 3D geometry surfaces was analyzed. Using empirical data collected on the evaporative flux of the 2D material as a function of light intensity (Figure B.1-C), the evaporative flux of each 2D subunit was estimated. By summing up the evaporation contributions of each 2D subunit, the total evaporative flux of the 3D geometry is determined. The detailed procedure used in the light intensity and flux analysis can be found in the Supplementary Note 1 in Appendix B.

Material Preparation

The 3D GO stalk was synthesized using a procedure adapted from our previous work.[65] As shown in Figure 3.2-A, a GO coating solution was prepared by mixing 17.5 mg/mL graphene oxide (GO) suspended in water, 0.035 M NaOH, 1,4-butanediol diglycidyl ether (BDGE) and triethylenetetramine (TETA) at a volume ratio of 248 : 12.4 : 27 : 10, while keeping all chemicals on ice. The GO coating solution was sonicated with a probe sonicator (Q500 Sonicator, Qsonica, Newtown, CT) at 40% amplitude for 4 minutes. Approximately 2.0 mL of the GO coating solution was applied to a cotton humidifying filter (0.75-cm in diameter, 15-cm in height), which served as the substrate for the 3D GO stalk. The GO-coated stalk was immediately submerged in liquid nitrogen until completely frozen and then transferred to a freeze-dryer (FreeZone 1, Labconco, Kansas City, MO) and kept at a temperature of -50°C and a pressure less than 0.2 mbar for more than 12 hours. The stalk was then placed in an oven at 100°C to crosslink GO and BDGE-TETA for 24 hours. The crosslinked 3D-GO stalk was then soaked in deionized water to dissolve chemical residual for 24 hours, dried in a 60°C oven, and stored in air at room temperature. Synthesis of the 2D GO evaporator followed the same procedure, except that the substrate used was a filter paper coupon (4.7-cm in diameter) and approximately 0.34 mL of the GO coating solution was coated on each coupon.

Material Characterization

The surface morphology and pore size of the 3D-GO stalk were characterized by SEM (Gemini Ultra-55, Zeiss). The light absorption spectra for the 2D- and 3D-evaporators were characterized using UV-Vis-Nir spectrophotometer with an integrating sphere (ASD QualitySpec Pro, Malvern Panalytical and Cary 5000, Agilent). The thermal conductivities were measured using a Cut-Bar method described in Supplementary Note 3 in Appendix B.

Solar Evaporation Setup

To prepare for a solar evaporation experiment, the 3D GO stalk was placed in a 250-mL beaker filled with 200 mL of feed water. The 3D stalk was secured in place by a circular extruded polystyrene (EPS) foam that fit into the top of the beaker and had a hole in its center to hold the 3D stalk. Parafilm was wrapped around the edge of the beaker and the 3D stalk to avoid leaking water vapor from the container. The bottom of the stalk was submerged in feed water to continuously supply water to the evaporation surface under capillary action. The length of the stalk above the EPS foam represents the effective height of the 3D evaporator, and it was adjusted to 1, 7.5, and 13 cm to achieve evaporation area index (EAI) values of 6.3, 41, and 70, respectively. The EAI is defined as the ratio of total surface area for evaporation relative to the projected ground area. By this definition, a 2D evaporator has an EAI of 1, whereas the EAI of a cylindrical 3D evaporator would increase with height. This relationship can be described by Equation 3.1.

$$EAI_{cylinder} = \frac{A_{total}}{A_{projected}} = \frac{\frac{1}{4}\pi d^2 + \pi dh}{\frac{1}{4}\pi d^2} = 1 + \frac{4h}{d} \tag{3.1}$$

where d is the diameter and h is the effective height of the cylindrical GO stalk. If not specified, the effective evaporative height of the 3D GO stalk was kept at 7.5-cm, corresponding to an EAI value of 41. A similar setup was used for the control evaporation experiment for 2D evaporator except that the 2D GO coupon was placed flat on the EPS foam on top of a 250-mL beaker. The feed water was transported to the 2D GO coupon by a water-absorbing sheet (Nalgene Versi-Dry Surface Protectors, Thermo Fisher Scientific) placed underneath the 2D GO coupon.

Solar Evaporation Experiments

The solar evaporation performance of the 2D or 3D evaporator was evaluated using a solar simulator (91194-1000, Newport, Irvine, CA) at an intensity of 1,000 $W\ m^2$ at the most elevated point of light absorption. The mass evaporated over time was recorded every minute using a mass balance, while the surface temperature was monitored periodically using a Ti100 infrared camera. The ambient conditions were monitored using temperature-humidity sensors (DHT22, Adafruit Industries), reporting temperatures between 25 – 35°C and relative humidity between 20 – 40%.

The evaporative flux as a function of zenith angle was measured by angling the 2D and 3D evaporators relative to the fixed light source by 20°, 40°, 60°, and 75°. For the 2D evaporator, this was achieved by using an extended water transporter and elevating the EPS base with aluminum foil. This modified base could then be angled to the specified zenith angles. The evaporative flux as a function of wind speed was measured by placing a variable speed fan (Thermaltake, Taipei, Taiwan) about 10-cm away from the evaporator surface. Using an anemometer (Flexzion), the wind speed generated by the fan at the material surface was

measured to be approximately 1.3, 1.9, and 3.5 m/s.

The evaporative flux as a function of salinity was measured by varying the NaCl concentration in the feed solution. The salt concentration tested included 3.5, 7.0, 10.5, 14.0, 17.5 wt % NaCl, representing 1x, 2x, 3x, 4x, and 5x typical seawater salt concentration (3.5 wt %). A long-term scaling test was run with 17.5 wt % NaCl, under 1-sun conditions (1 $kW\ m^2$) for 45 hours.

3.4 Results and Discussion

3D-Geometric Design

To determine the optimal geometry and guide the rational design of a 3D structure for solar evaporation, we used MATLAB to predict the evaporative flux rates of different 3D structures under varying incident light angles. We first analyzed the variation of solar intensity on the 3D structure surfaces at zenith angles of 0° (solar noon position) and 45°. Analyzing the performance of 3D structures at different incident light angles is important because it illustrates how the performance of the evaporator would vary throughout the day because of solar movement. Although this daytime variability in performance is an integral feature of all evaporators, it has not been rigorously characterized until this work.

As illustrated in Figure 3.1-B, we selected three structures (dome, cone, and cylinder) to study the effect of EAI. The light intensity on the surfaces of each of the 3D structures is not uniform due to the changing inclination angle of the surfaces. At a Zenith angle of 0°, the top surface of the 3D cylinder receives the highest light intensity, but its side surface does not receive any direct light exposure; while the light intensity on the dome and cone surfaces are weaker and distributed into a larger area. When the Zenith angle increased to 45°, all the 3D structures demonstrated larger areas being exposed to relatively high light intensity.

After translating the light intensity distribution to evaporative water flux, the total water flux for each 3D structure was calculated and plotted in Figure 3.1-C. At both 0 and 45° Zenith angles, the cylindrical 3D structure demonstrated the highest water flux among the three geometries being studied. The advantage of the cylinder is primarily a result of the higher EAI values than that of the cone or dome. For example, the EAI for the cylinder, dome, and cone at the height of 5 cm is 21, 16, and 10, respectively. The increase of structure height will result in further increase of EAI values and corresponding increases of evaporative water flux, as illustrated in Figure 3.1-C. However, the evaporative flux cannot increase indefinitely, as it will be eventually limited by the maximum rate at which water can be lifted to the evaporative interface by capillary forces. The maximum water lifting rate was calculated by assuming an internal pore diameter of 100 μm and a water contact angle

of 0°, and the results are plotted as the water lifting limit in Figure 3.1-C. The detailed calculation of the water lifting limit was described in the Supplementary Note 2 in Appendix B.

As shown in Figure 3.1-C, the water lifting limit decreases with increasing structure height, and its intersection with each flux line (for cylinder, cone and dome) represents the maximum achievable evaporative flux for each geometrical design. For instance, the maximum evaporative flux for a cylindrical 3D evaporator under the current design is 22 $kg\ m^{-2}\ h^{-1}$, which was achieved at a height of 10.4 cm when the solar Zenith angle is 0°. Any increase of the cylinder height beyond 10.4 cm will not be able to further increase the evaporative flux due to the water lifting limit. At Zenith angle of 0°, the maximum evaporative flux of the cone and dome are 14 and 12 $kg\ m^{-2}\ h^{-1}$, respectively, much lower than that of the cylinder. Similarly, when the Zenith angle is 45°, the maximum evaporative flux of the cylinder (34 $kg\ m^{-2}\ h^{-1}$) is much higher than that of cone and dome (22 and 18 $kg\ m^{-2}\ h^{-1}$, respectively). This analysis indicates that a cylinder represents a better 3D design than a cone or a dome as it will produce the highest EAI and evaporative water flux. Therefore, we chose the cylindrical design as the geometry of the 3D evaporator to investigate in the subsequent experiments. Note that the quantitative prediction of maximum flux or height may differ from the real experimental data as the base and pore diameters of the synthesized 3D evaporator could be different from the parameters that we assumed in the calculation.

Synthesis and Characterization of Cylindrical 3D Evaporator

To synthesize a cylindrical 3D evaporator, we started with a commercially available cotton humidifying filter that serves as a substrate with high internal porosity, high hydrophilicity, and low thermal conductivity. To maximize the EAI, it is critical to have high internal porosity and hydrophilicity to increase the limits of water replenishment rate so that water lifting does not become a limiting factor for high evaporative flux. Low thermal conductivity is critical for heat localization so that the absorbed solar energy can be effectively utilized for water vaporization. To enable effective solar light absorption, the cotton stick was coated by crosslinked graphene oxide (GO) following the procedure illustrated in Figure 3.2-A. This creates a 3D GO stalk with a light-absorbing exterior that has sub-micrometer pores (Figure 3.2-B), while leaving the core unmodified to facilitate rapid water transport via capillary wicking (Figure 3.2-C). Based on the SEM, the pore size between cellulosic fibers in the unmodified core ranges between 50 and 200 μm, whereas the GO coating provides much smaller pores that can be less than 0.5 μm. The heterogeneity of these pores enables the cylindrical 3D evaporator to rapidly lift water through the middle of the stalk and achieve saturation, while using high capillary pressure at the evaporative interface to maintain a wet state during operation.

In addition to having an efficient water replenishment mechanism, the 3D GO stalk demonstrates high efficiencies in broadband light absorption and heat localization that greatly contribute to solar vapor generation. As shown in Figure 3.2-D, compared to a 2D-GO con-

trol, which underwent a similar synthesis process to that of the 3D-GO stalk except that a filter paper was used as the supporting substrate,[65] the 3D-GO stalk demonstrates higher and near-complete absorption of light across the solar spectrum from 350 to 2500 nm. The higher absorption efficiency of the 3D-GO stalk is attributed to the thickness of the GO photo-thermal material, which allows for complete absorption of light that is transmitted by its top surface.

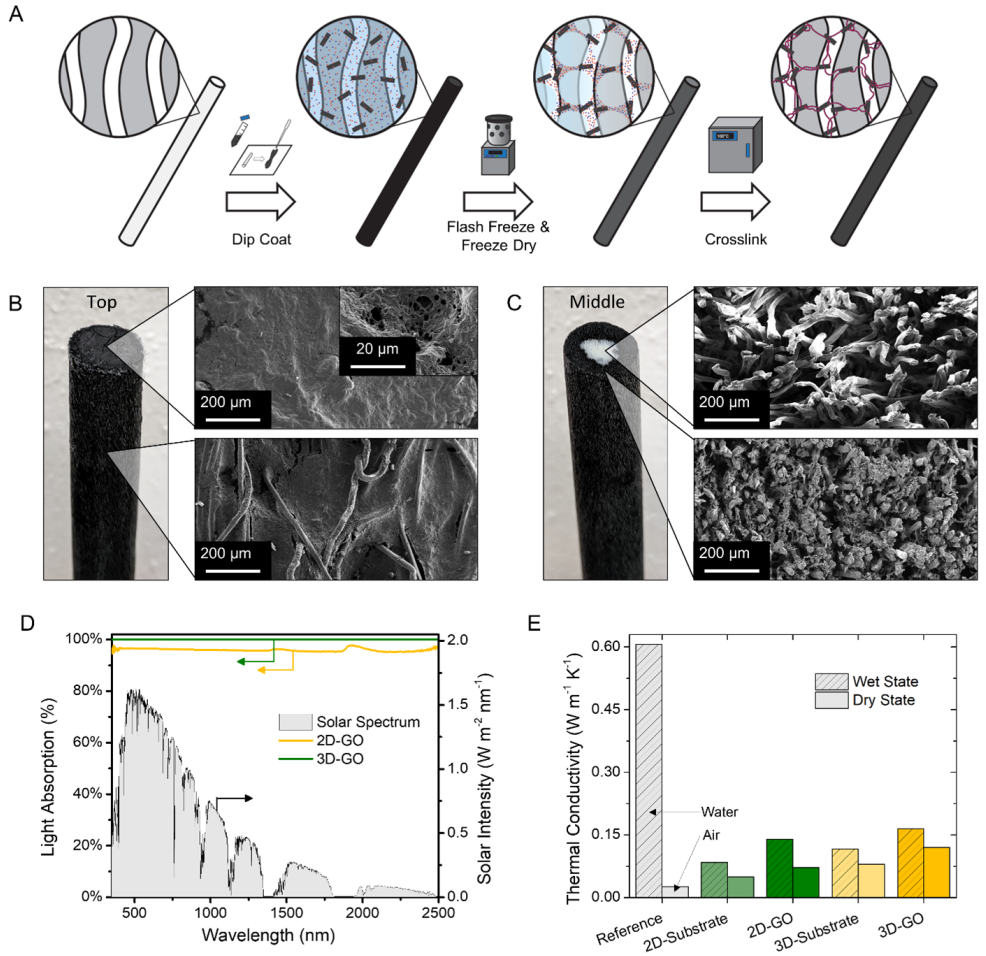

Figure 3.2: Synthesis and characterization of the cylindrical 3D-GO stalk. A) Synthesis of the cylindrical 3D evaporator by coating GO on a cotton stick. B) Scanning electron microscopy (SEM) images of the top (with a higher magnification insert) and side of the synthesized 3D GO stalk. C) SEM images of a cross-section from the middle of the 3D GO stalk, showing the unmodified cellulose fibers at the core and GO-modified cellulose fibers toward the outer perimeter. D) Light absorption across the solar spectrum of the 2D- and 3D-GO. E) Thermal conductivity of the 2D- and 3D- substrates and GO evaporators.

In conventional 2D evaporators, heat localization at the air-water interface is achieved with a thermal insulation layer that minimizes conductive heat losses from the surface to

the bulk water. To evaluate the heat localization capability, the thermal conductivity of the evaporators, as well as the unmodified substrates, was measured in both wet and dry states. Figure 3.2-E shows that introducing the GO coating increases the thermal conductivity of both the 2D- and 3D-evaporators compared to the unmodified substrate. This is expected as the cross-linked GO replaces air in the porous substrate. As a result, the higher thermal conductivity of the crosslinked GO increases the materials' effective thermal conductivity. Similarly, the wet evaporators have higher thermal conductivities in comparison to their dry counterparts as water displaces air within the porous structure. The thermal conductivities of the wet 2D- and 3D-evaporators are 0.140 and 0.165 $W\ m^{-1}K^{-1}$, respectively. Even though the 3D geometry results in a higher thermal conductivity, the distance over which heat must be conducted before being lost to the bulk water reservoir is significantly larger (1-13 cm) than traditional 2D evaporators ($\sim$200 μm). This dramatically reduces the overall heat loss due to conduction and maintains the heat localization that is necessary for efficient evaporation.

Evaporation Performance of the 3D GO Stalk

The vapor generation performance of the 3D GO stalk was evaluated using the setup illustrated in Figure 3.3-A. The bottom of the GO stalk was submerged in the feed water reservoir to take in water, while the stalk above the white polystyrene base provided an effective area for water evaporation. By adjusting the height of the GO stalk above the base to 1, 7.5, and 13 cm, we studied the performance of the GO stalk at EAI values of 6.3, 41, 70, respectively. We also characterized the performance of a 2D GO evaporator, which by definition has an EAI value of 1. As shown in Figure 3.3-B, operating under 1-sun conditions, increasing the EAI value beyond 1 significantly increased the evaporative flux from 1.8 (EAI = 1.0) to 34.7 (EAI = 70) $kg\ m^{-2}\ h^{-1}$.

The flux enhancement can be attributed to both increased total surface area available for evaporation and more effective utilization of energy sources (e.g., ambient heating, diffuse radiation) other than the solar energy input. For example, ambient heating can serve as an additional energy source due to convective heat transfer from the relatively warmer ambient environment to the cooled sides of the 3D GO stalk. As demonstrated by the thermal images in Figure 3.3-C, the side surfaces of the GO stalk that are not in direct sunlight drop to a sub-ambient temperature because of evaporative cooling. Similarly, the stalk under dark conditions is much cooler than the ambient air, enabling heat transfer from the ambient environment to the evaporation surface. Comparing the evaporative performance under 1-sun and dark conditions indicates that a large percentage of water flux is attributed to the evaporation taking place under dark conditions, as shown in Figure 3.3-B. The high evaporation flux under dark conditions confirms that the 3D GO stalk with its large EAI is capable of effectively using ambient heating compared to other geometries. Although similar behavior of drawing heat from the environment during evaporation has also been observed in other studies,[58, 114, 59] the high aspect ratio of our 3D GO stalk capitalizes on this

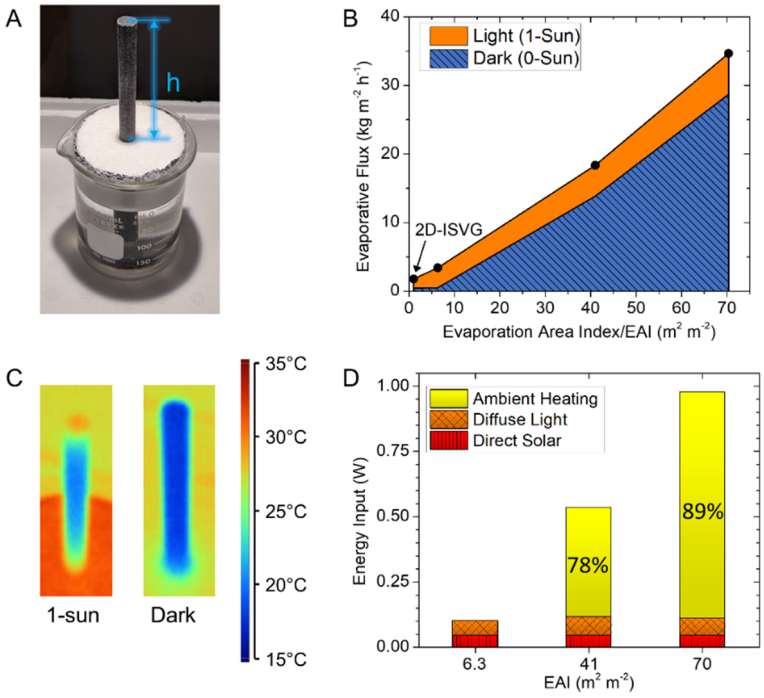

Figure 3.3: Evaporation performance and efficiency of the 3D evaporator. A) The experimental setup for performance characterization. B) The change of evaporative flux of the 3D GO stalk in dark and light conditions as EAI value increases. C) Thermal images of the 3D GO stalk under light and dark conditions. D) Contribution to energy input from direct solar, diffuse light, and ambient heating.

phenomenon, allowing the GO stalk to achieve evaporative flux rates 15-20 times what has been previously reported.

As shown in Figure 3.3-B, the evaporative flux of the 3D GO stalk with high EAI values (40-70) are more than 10 times higher than the maximum solar-to-vapor output of 1.5 $kg\ m^{-2}\ h^{-1}$ under 1-sun conditions.[39] This again indicates that energy sources other than direct solar are playing a very important role in contributing to the high evaporative flux (18.4 $kg\ m^{-2}\ h^{-1}$ for the 7.5-cm stalk and 34.7 $kg\ m^{-2}\ h^{-1}$ for the 13-cm stalk). In order to understand the roles of different energy sources, the total energy input (q_{input}) can be analyzed by accounting for the three primary energy sources:

$$q_{input} = q_{solar} + q_{diffuse} + q_{ambient} \tag{3.2}$$

where q_{solar}, $q_{diffuse}$, and $q_{ambient}$ are energy flows coming from direct solar radiation, diffuse radiation, and ambient heating. A full description of how each of these factors were accounted for can be found in Supplementary Note 4 and 5 in Appendix B. Through this analysis, the contributions from each energy source were calculated and plotted in Figure 3.3-

D. The amount of energy from direct solar and diffuse light remains constant when the EAI value changes. However, as the EAI value increases, a growing amount of energy comes from ambient heating. For example, when EAI increases from 6 to 70, the energy contribution from ambient heating increases from 0% to 89% of total energy input, while the contribution from direct solar decreases from 44% to 4.5%. This shows that the increase in evaporative flux as the height of the GO stalk increases is primarily a result of absorbing more ambient heating. It indicates that the 3D GO stalk would generate effective evaporation in a warm, dark environment even without sufficient sunlight exposure. Overall, the 3D GO stalk can derive the energy for evaporation from multiple sources, enabling a dramatic reduction in the spatial footprint of solar evaporation.

3D-Enhanced Omnidirectional Light Utilization

One major advantage of the 3D evaporator is its omnidirectional light utilization as the sun moves across the sky throughout the day. Most solar evaporation studies use a solar source at a fixed position, often under the optimal conditions of solar noon with a zenith angle of 0°, i.e., with the incident light perpendicular to the evaporation surface. However, understanding the effect of solar movement is critical to predict the actual performance of solar evaporators throughout the day. For 2D evaporator, an increase in the zenith angle when the sun deviates from a vertical position decreases the projected cross-section that receives solar radiation, resulting in a decrease of evaporative flux (Figure 3.4-A). However, the 3D evaporator exhibits an opposite trend, with an increase in evaporative flux as the solar angle deviates from the noon position. The reason for this is that under solar noon conditions, the only surface to receive direct radiation is the top of the cylindrical 3D stalk. As the zenith angle increases, a greater cross-section (including a portion of the sides of the cylinder) is irradiated by sunlight, resulting in a higher evaporative flux. This is a promising result for outdoor applications of 3D GO evaporator, where higher performance may be achieved in the hours leading up to and away from solar noon.

3D-Enhanced Utilization of Wind Energy

The second advantage of the 3D GO stalk is that it can extract energy from the ambient environment, thus resulting in efficient utilization of convection from the wind. To demonstrate this advantage, we used a fan to blow air at varying speeds across the 2D- and 3D-evaporators and observed significantly higher flux enhancement in the 3D evaporator than 2D. As shown in Figure 3.4-B, when the external air flow rate increases from 0 to 3.5 $m\ s^{-1}$, the evaporative flux of the 3D GO stalk increases from 15.4 to 52.7 $kg\ m^{-2}\ h^{-1}$, resulting in an increase of 241%; while the flux of 2D material only increases from 2.2 to 3.2 $kg\ m^{-2}\ h^{-1}$, an increase of merely 45%. The differences between the 2D- and 3D-evaporators are attributed to the geometry difference that affects the formation of the airflow boundary layer. The thickness of this boundary layer is important because water vapor molecules produced by the evaporator must diffuse through the boundary layer before convective forces sweep them

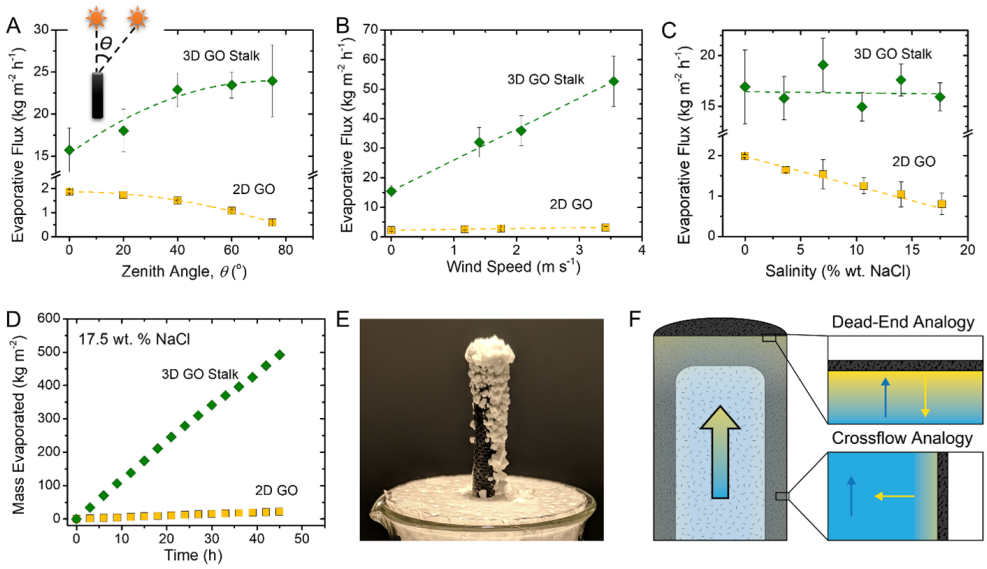

Figure 3.4: Enhanced evaporation performance enabled by 3D geometry. Comparison of the performance of 3D and 2D GO evaporators as a function of A) varying incident light angle, B) increasing wind speed (external forced convection rates), and C) increasing feedwater salinity. D) Mass evaporated over time with a feedwater containing 17.5 wt. % NaCl to demonstrate the constant evaporative flux observed despite scale formation. E) Scale formation on the surface of the 3D GO stalk. F) Dead-end and crossflow analogies to describe scaling behavior of the 3D-GO stalk.

away. As the rate of forced convection increases, the boundary layer thickness is compressed, decreasing the distance that water molecules must diffuse and increasing the driving force for evaporation. However, given that the average flow path length across the 2D evaporator is longer than that of the 3D evaporator, the boundary layer is still developing (and thus thinner) over a greater portion of the 3D evaporator surface area. As a result, the 3D GO stalk has a significantly higher response to increases in external convection rates than the 2D GO evaporator. This result is also promising because vapor accumulation near the evaporative interface is a severely limiting factor for vapor production in closed systems (such as a traditional solar still) that aim to condense the water vapor. Introducing external forced convection not only increases the rate of evaporation, but also could contribute to moving water vapor into a separate stage for condensation if water recovery is desired.

Resilience to Mineral Scaling

A final unexpected, but exciting advantage of the 3D GO stalk is its capability of maintaining high evaporative flux when feedwater salinity increases. As shown in Figure 3.4-C, the evaporative flux of the 3D GO stalk remains almost constant at 16.0 $kg\ m^{-2}\ h^{-1}$ over the range of 0 to 17.5 wt. % NaCl, demonstrating a resilience to increasing feedwater salinities which resemble brines that can currently only be treated with energy intensive thermal brine

concentrators. The flux of 2D GO evaporator decreases from 2 to 0.5 $kg\ m^{-2}\ h^{-1}$ under these same conditions, which is expected due to the reduction in vapor pressure caused by increasing feedwater salinity, consistent with what we reported in an earlier study.[65, 102] In addition, the high flux of 3D GO stalk is not affected by the accumulation of salt on the evaporative surface. As seen in Figure 3.4-D, the evaporated mass of water for both 2D- and 3D-evaporators increases at a relatively constant rate during the course of a continuous 45-h evaporation run, despite significant salt accumulation can be observed on both 2D (presented in our previous publication6) and 3D material surfaces (Figure 3.4-E) at such high salt concentration (17.5 wt. % NaCl) in feedwater. Note that further studies are needed to investigate the effects of more complicated mineral composition on this behavior.[131] Nevertheless, with pure NaCl the continuous high flux of the 3D stalk results in the vaporization of a total of 492 kg of water per m^2 throughout the 45-h period, while under the same condition the 2D GO evaporator would only vaporize 22 kg of water per m^2. Such a high evaporation rate for a salinity that is 5 times more concentrated than seawater demonstrates the potential of the 3D GO stalk for brine concentration and ZLD applications.

To explain why the 3D GO stalk has better resistance to these high salinities compared to its 2D counterpart, we illustrate the transport process in the 3D stalk using an analogy from membrane filtration (Figure 3.4-F). The evaporation process on the top surface of the stalk is analogous to a dead-end filtration, which results in extreme concentration polarization because the direction of water flow opposes the direction of the back-diffusion of salt, creating a higher salt concentration at the evaporative interface on top of the 3D GO stalk. These high salt concentrations lower the saturation vapor pressure at the evaporative interface, thus lowering the driving force for evaporation and decreasing the flux. Since the evaporation on the entire 2D evaporator is like dead-end filtration, its performance is prone to the negative impacts of high salt concentration. However, such an effect on the performance of the 3D GO stalk is greatly diminished because the top surface evaporation constitutes a small portion of the total evaporative surface area (only 2.4% for this experiment). Meanwhile, the side surfaces of the 3D GO stalk benefit from crossflow, where the back-diffusion of salt ions is accelerated by the upward flow of water through the 3D stalk. Therefore, the reduced concentration polarization on the sides may slow down the accumulation of salts and contribute to maintaining a constant evaporative flux for the 3D GO stalk.

Furthermore, the precipitation of salt onto the surface of the 3D GO stalk (Figure 3.4-E) presents another promising opportunity in ZLD, i.e., mineral recovery. As salt crystals grow on the sides of the cylindrical 3D evaporator, they gradually become unstable and naturally slough off the cylindrical structure. This process could be engineered into a passive salt management strategy that simultaneously prevents excessive buildup of salt on the 3D structure while collecting crystallized salt with valorization application.

Technology Outlook for the 3D GO Stalk

This study explored a variety of advantages of using 3D GO stalk for brine treatment in comparison with 2D evaporators. As summarized in Figure 3.5-A, our cylindrical design significantly increases the EAI value, enabling high evaporative flux that is about 100 times faster than a traditional evaporation pond. The flux enhancement is also attributed to more efficient use of ambient heating and omnidirectional light utilization. In addition, the 3D GO stalk is capable of maintaining high flux in highly concentrated brine and demonstrates potential for mineral recovery. We also compared the performance of the 3D GO stalk with published literature on other 3D structures. As shown in Figure 3.5-B, this study is one of two studies with EAI values greater than 30 (see Supplementary Note 6 in Appendix B for full details).[117] Most structures have low evaporative fluxes (less than 5 $kg\ m^{-2}\ h^{-1}$) due to relatively low EAI values.[58, 38, 110, 132, 133] Although some other studies demonstrate 3D evaporators with moderate EAI values, they do not achieve comparable evaporative flux rates owing to self-inhibiting structures, i.e., their geometries prevent the diffusion of water vapor away from the evaporator, creating high-humidity pockets near the evaporative interface that diminish the driving force for evaporation.[111, 120, 119, 118, 112]

The high evaporative flux combined with the passive salt management strategy demonstrated in this work indicated that the 3D GO stalk has the potential to significantly reduce the spatial and energy footprint of brine treatment. If paired with upstream purification steps, the 3D GO stalk could be used for continuous production of mineral resources for salt mining or resource recovery operations. Further investigation is still needed to study the effects of scaling up to a treatment system that contains a large number of GO stalks and to evaluate the fouling performance under long-term operation with realistic feed streams. Nevertheless, the 3D GO stalk has demonstrated the ability to significantly reduce the spatial footprint of the solar evaporation process while passively processing brines with salt concentration as high as 17.5 wt%, bringing the field one step closer toward the development of a sustainable off-grid desalination technology with ZLD and salt recovery.

3.5 Conclusion

This work explored how capillary wicking can be used to passively supply water to additional surfaces, accessing EAI values significantly greater than 1. In 1-sun conditions, a GO stalk with an EAI value of 70 was able to achieve an evaporative flux of 34.7 $kg\ m^{-2}\ h^{-1}$, which is the highest reported evaporative flux in the field to date. This work was also the first to conduct a thorough energy balance on a 3D-ISVG material, ascertaining that the corresponding evaporation efficiency (when accounting for solar irradiation, diffuse light, and ambient heat) was 95.3%. Furthermore—in a systematic comparison to the 2D GO leaf—the 3D GO stalk exhibited unique advantages including omnidirectional sunlight utilization, a dramatic increase of the evaporation rate by introducing wind, and scaling resistance in

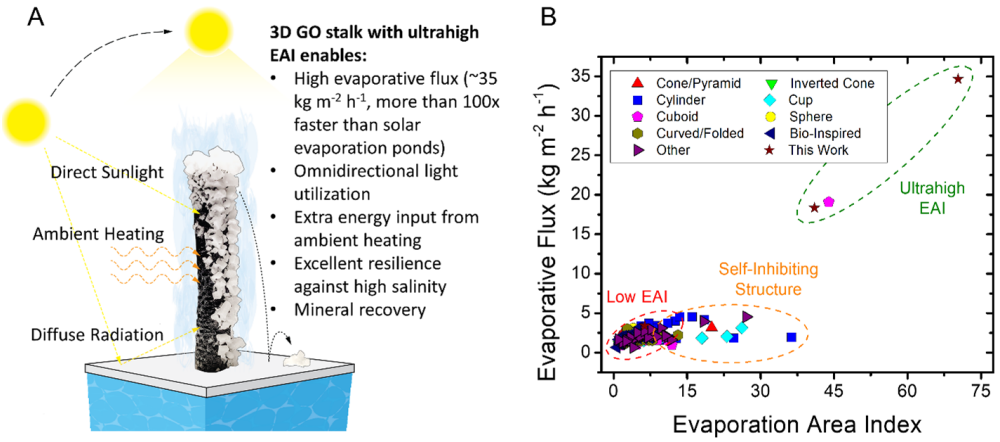

Figure 3.5: Comparison of the performance of the GO stalk to other 3D evaporators. A) Summary of the advantages of 3D GO stalk. B) Comparison of our work with the evaporative flux of 3D evaporators reported through June 2021.[103, 107, 106, 58, 38, 108, 79, 109, 110, 34, 111, 112, 114, 115, 113, 116, 117, 59, 132, 133, 118, 119, 120, 121, 122, 123, 124, 125, 126, 127, 128, 129, 130, 134, 135, 136, 137, 138, 139, 140, 141, 142, 143, 144, 145, 27, 146, 147, 148, 149, 150, 151, 152, 153, 154, 155, 156] The data were all obtained under 1-sun conditions.

evaporating brines with a salt content of up to 5 times seawater (17.5 wt % as NaCl).

The evaporative flux rates demonstrated in this work are high enough for some water treatment applications, although efforts are still needed to fully explore the potential of 3D-ISVG materials, especially with regards to condensing the water vapor produced by ISVG. Based on the work that has been presented here, omni-directional light utilization, wind-driven performance enhancement, and resiliency to mineral scaling have all been identified as key features that should be taken advantage of in these applications. Coupling these features with the ability for ISVG to operate passively (or without an electrical input), a decentralized ISVG-based technology may have an advantage over conventional desalination technologies in low-resource settings. While membrane-based desalination technologies are generally able to achieve higher energy efficiencies than ISVG,[157] this performance is contingent on reliable access to high-grade energy, supply chains for equipment and chemicals, and technical expertise for maintenance and operation.[158] Furthermore, deploying a technology without understanding the context in which it is being implemented can lead to site-specific factors confounding the success of technical interventions.[159] Therefore, a Development Engineering approach has been used to evaluate the feasibility of an ISVG-based technology for increasing water access for the small-island community of Bungin Island in Indonesia.

Chapter 4

Feasibility of ISVG as a Sustainable Desalination Technology for Small-Island Communities

4.1 Introduction

Small island communities are acutely vulnerable to climate-induced water scarcity. With an increase in hurricanes and extreme storm events, flooding can contaminant an island's surface water resources.[160] Meanwhile, sea level rise promotes seawater intrusion causing the salinization of the island's groundwater sources.[161] As a result, 71% of small islands in developing states face risks of water shortages.[162] While interventions to increase water access exist, many of these efforts fail because they lack the technical, managerial, and financial resources to support the projects long-term.[163] Furthermore, technological interventions often ignore the unique context in which they are being implemented creating additional barriers for success.[164]

Solar-thermal desalination is a (re)emerging approach[165] that has a great potential for improving water access in under-resourced settings, including small-island communities.[157] Drawing on the radiative energy in sunlight, these approaches typical entail the photothermal heating of water to promote distillation (the vaporization of water) and subsequent condensation. Specifically, interfacial solar vapor generation (ISVG), mediates this process using a porous, light absorbing material. When these ISVG materials are exposed to sunlight, it absorbs that light, turns it into heat, transfers that heat to water in its pores, and accelerates evaporation.[14] Recent work to increase the throughput of these materials has led to the advent of three-dimensional ISVG (3D-ISVG) that use capillary action to wick water to additional surfaces for evaporation and draw upon the heat from the surrounding environment to increase the maximum water output achievable by this process.[59] These 3D-ISVG materials have also demonstrated omni-directional light utilization, performance

enhancement with forced convection, and increased resilience to the impacts of inorganic fouling.[66]

While these features of 3D-ISVG may be promising for the development of a sustainable solar-thermal desalination technology for small-island communities, the ultimate success (or failure) of such a technology will depend on how well context-specific factors are incorporated into its design and implementation.[166] Following Development Engineering's principle to understand the problem, context, and needs,[64] this research will focus on the unique water-related challenges faced by small-island communities in Indonesia, and analyze whether it is feasible to apply an ISVG-based solar desalination to address its water challenges.

Located in Southeast Asia between the Indian and Pacific Oceans, Indonesia is home to more than 273 million people across approximately 6,000 islands—the most of any country in the world. Although Indonesia's water challenges are diverse, it is currently estimated that about 22 million Indonesians lack safe drinking water.[167] Zooming in further, this work aims to understand the historical, physical, and social constraints entangling the water access for the Indonesian community of Bungin Island, and how this context should be incorporated into the development of 3D-ISVG into a sustainable desalination technology.

4.2 Background on Bungin Island, Indonesia

Bungin Island is a small-island community located off the coast of Sumbawa Province in the West Nusa Tenggara Regency of Indonesia (see Figure 4.1-A,B). The island is inhabited by descendants of members of the Bajo Tribe, who sailed to Bungin Island from southern Sulawesi around 1800.[168] Along with their own language (*Bahasa Bajo*), the original inhabitants of Bungin Island brought many Bajo traditions with them, including *Nangung Rumah*, which requires men who wish to marry to build the foundation of their family's future home by gathering rocks and dead coral from the waters surrounding the island (see Figure 4.1-C).[169] Although Bungin Island was only about 3 hectares upon its founding, this practice has increased the size of the island to more than 8.5 hectares. The housing arrangement that has arisen from this tradition is uniquely dense, and—with a population exceeding 3,400 people—Bungin Island is known as "The Most Populous Island in the World" by Indonesians.[62]

Despite its high population density, Bungin Island has no freshwater resources on the island itself. Traditionally, residents of Bungin Island would travel by boat to mainland Sumbawa to collect groundwater from a well.[170] As the population of Bungin Island continued to grow, an undersea pipe was constructed in the early 1990s to supply water from the Marente-Alas River to Bungin Island. Homes located near the center of the island were connected to this piped infrastructure first and receive water directly on their premises. In expansions of this piped infrastructure that occurred in the late 2000s, additional homes situated near the existing piped infrastructure have been connected, but homes located further

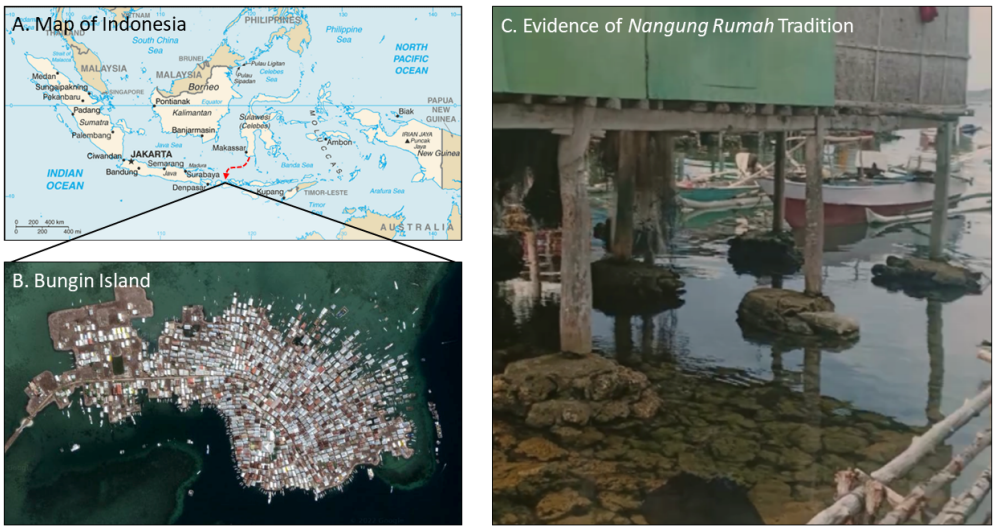

Figure 4.1: Geographical and historical context of Bungin Island. (A) Map of Indonesia showing the migration of members of the Bajo Tribe from Southern Sulawesi to Bungin Island. (B) 2022 Satellite image of Bungin Island. (C) New homes constructed in water around Bungin island following the *Nangung Rumah* tradition.

away—or homes that were built after these expansions—remain disconnected. As a result, these homes continue to travel off-island—typically by boat—to collect water from coastal wells.

These water challenges have been amplified by growing water scarcity. With less water available from the Marente-Alas River, the local water utility—known as PDAM (Perusahaan Daerah Air Minum)—switched to an intermittent water supply, only supplying water via the piped infrastructure periodically. Homes located upstream on the piped infrastructure will often store excess water that can be used later or resold. Unfortunately, this causes the water to run out before it reaches other homes located downstream on the piped infrastructure, forcing more households to either have to purchase water from their neighbors or travel off-island to access coastal wells. More recently, deterioration of the piped infrastructure has resulted in leaking and clogging issues. When piped water cannot be provided, PDAM will often deploy water tankers to Bungin Island, although limited road access on Bungin Island causes this intervention to perpetuate many of the same water access inequities as the piped infrastructure. Meanwhile, the Ministry of Maritime Affairs and Fisheries installed a seawater water desalination plant on Bungin Island in 2018. However, maintenance issues caused the plant to be shut down after only a few months of operation.[171] Too much water can present its own challenges. In early 2022, heavy rains caused a flash flood that damaged the pipe that supplies water to Bungin Island,[172] preventing water from being supplied to the island for approximately two months. Similar to times of water scarcity, water tankers are used to alleviate water stress anytime when the piped network is down. Forcing more

people to travel off-island to obtain water, the culmination of these events has created an undue water burden for those living on Bungin Island.

While technological interventions cannot serve as a panacea for all of these water challenges, there may be opportunities to alleviate specific instances of water stress on Bungin Island by exploring the current context surrounding water access and incorporating these insights into the development of a novel water treatment technology. By conducting interviews with current residents, this work serves as a feasibility analysis for how a technology using 3D-ISVG could be designed to improve water access on Bungin Island.

4.3 Materials and Methods

Prior research about the settlement patterns of Bungin Island[173] categorized households into three regions: central, intermediate, and outer. Central households—as the name suggests—are located more centrally on Bungin Island near its main roads. Having been established for longer, these central households are more likely to have undergone renovations and have better access to amenities, such as piped water access onto their premises. Intermediate households surround the central region of the island and spread out to the coastline of Bungin Island. Having been built more recently, these households have had less time to undergo renovations and are built along more narrow roads. Lastly, outer households border the coast of Bungin Island and extend beyond the coastline. These households were built most recently—with the least amount of time for renovations—and are typically constructed on partially reclaimed ground or directly above the ocean.

We applied this framework to explore how the location of a household can impact water access. As illustrated in Figure 4.2, the central households (colored in green) are located directly adjacent to the roads, which is being used as a proxy for the piped water network. The exterior households (colored in red) are either bordering the coastline of the island or located on the water. Lastly, the intermediate households (colored in yellow) are the remaining households that are not located in proximity of either the roads or the ocean. Twelve households distributed across the central, intermediate, and outer regions of Bungin Island were invited to participate in semi-structured interviews. As the water access of households located in the outer region was hypothesized to be the most precarious, six outer households were interviewed, while three were conducted with central households and three were conducted with intermediate households. Households were selected at random, based on the rough locations within each region. Interviews were conducted in March 2022 by a team of interns using a semi-structured interview guide to understand the collection, storage, and use of water in the households. Additionally, these households were also asked to provide feedback on the preliminary design of a solar-thermal desalination system utilizing 3D-ISVG.

After obtaining informed consent, the interns conducted 30 minute, audio-recorded interviews. Interviewees received a prepaid phone card with a value of 100,000 IDR, as well as a

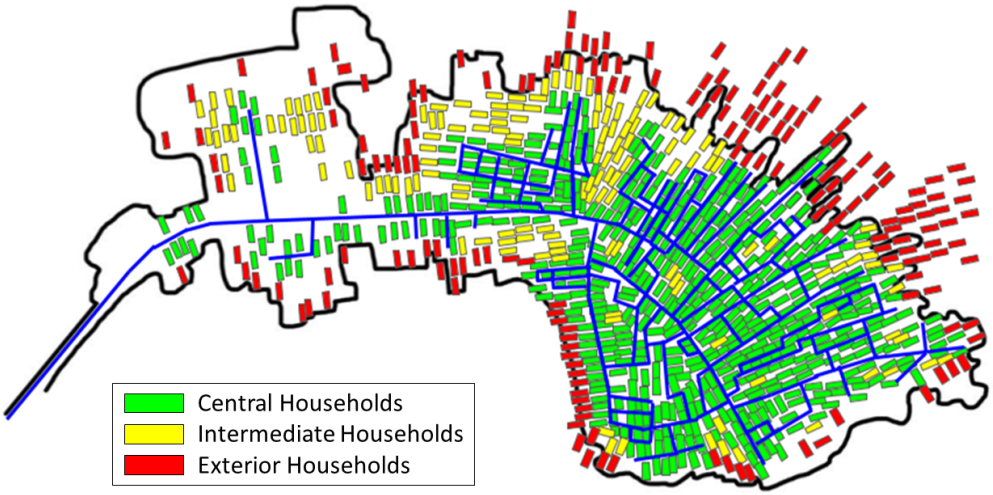

Figure 4.2: Categorization of households on Bungin Island into Central, Intermediate, and Exterior regions. The blue lines indicate roads that were observable by satellite and serve as a proxy for where the piped water is likely to be supplied to households.

refillable water bottle, for their participation in the interviews. This research was approved by the University of California — Berkeley's Committee for Protection of Human Subjects (IRB 2021-10-14763). All audio-recorded material was transcribed verbatim and then translated from Bahasa Indonesian to English using a translation service. Written notes taken by the interviewing interns were digitized to provide additional context to the transcripts. The content of the interviews was then analyzed to identify patterns and trends, as well as qualitative insights that should be incorporated into the design of a sustainable desalination technology.

4.4 Results

Household Characteristics

Interviews were conducted with household members who self-identified as being involved with the water collection. On Bungin Island, water collection appears to be a shared responsibility between the male and female members of the household, with 50% of interview households describing women as the primary water collector and the remaining describing men as the primary water collector. In general accordance with this stated practice, 58% of those who were interviewed were women. Many households described occupations relating to the fishing industry, with 60% of male respondents identifying as fishermen. Meanwhile, 86% of female respondents identified as vendors, with 33% of these respondents specifying that they sold fish at the market. Other male-oriented occupations included water taxi (20%) and service work (20%). In addition to being vendors—typically at the market or local kiosks—57% of female respondents also described housewife duties as part of their daily work.

While households built through the *Nangung Rumah* tradition are similar in size (roughly 10 meters by 6 meters in area)[174], households located more centrally on Bungin Island are generally older and have had more time to undergo renovations.[173] These improvements generally involve the continued raising of the land beneath the home so that entirely dry land beneath the home can be achieved. This space beneath the home is often used for storage or as a location for a kiosk. Meanwhile, within the home, walls are built to create permanent separation between rooms. The original stills that hold up the home are fortified and—in some cases—walls are built around the space beneath the home for the creation of additional rooms. This evolution of renovations generally occurs over the course of decades, with households located more externally—having been built more recently—having less time to enact these changes (see Figure 4.3). Despite this, households located in the exterior portion of the island had the highest average occupancy of 4.5 people per house. This average occupancy appeared to decrease for households located more centrally, with households located in the intermediate and central portions of the island having an average of 4.3 and 3.0 people per household, respectively. This is important because water demand generally scales with the number of water users, indicating that—on average—exterior households would have the highest demand for water.

Figure 4.3: General trajectory of home renovations on Bungin Island. From oldest to newest, households can be categorized into the following: (A) Central Households, (B) Intermediate Households, and (C) Exterior Households.

Household Experiences with Water

As seen in Table 4.1, households obtain their water from multiple sources to fulfill a variety of water uses in the home. The data that informs Table 4.1 was taken from responses where households were asked: (1) What are their primary water sources? (2) How do they use the water collected from each source? (3) How much does it cost to obtain water from each of these sources? And (4) how much time does it take to collect water from each of these sources? In column 1 of Table 4.1, the number of respondents that identified a particular water source is identified in parentheses. In column 2 of Table 4.1, respondents could iden-

tify multiple uses for each water source, but the number of respondents relative to the total is indicated in parentheses. These water uses generally fall into three categories: drinking, cooking, and cleaning—where cleaning generally entails washing the floors, counters, dishes, and clothes, as well as bathing. With regards to drinking water, 83% of households interviewed primarily used plastic cups, which can be purchased through kiosks located on the island or from stores on the mainland of Sumbawa. With regards to cooking water, 66% of households interviewed receive a galon (19-L container) through a service provided by a local enterprise that uses reverse osmosis to treat groundwater on mainland Sumbawa and delivers that water to the residents on Bungin Island. While less common, three households (25%) described using alternative water sources for drinking water, including piped water from the local utility (PDAM) and the galon. Similarly, four households (33%) described using alternative water sources for cooking, including piped water from PDAM, water purchased from neighbors (originally piped water from PDAM), freshwater from an off-island well, and water delivered by a water tanker. Lastly, piped water from PDAM, water purchased from neighbors, freshwater from an off-island well, water delivered via water tanker, brackish water from an on-island well, and water captured from rainwater were all used as sources for cleaning.

Table 4.1: Reported water sources, associated cost, and general water uses on Bungin Island.

Water Source	**Uses**	**Cost [IDR / L**	**Collection Time [min / week]**
Bottled Water (10)	Drinking (10/10)	1,856	6
Galon (8)	Cooking (8/8) Drinking (1/8)	421	25
Piped Water from PDAM (4)	Cleaning (3/4) Cooking (2/4) Drinking (2/4)	4	12
Purchased Water from Neighbor (9)	Cleaning (9/9) Cooking (1/6)	48	41
Freshwater Well, Off-Island (7)	Cleaning (7/7) Cooking (1/7)	338	125
Water Tanker (6)	Cleaning (6/6) Cooking (1/6)	100	25
Brackish Well, On-Island (3)	Cleaning (3/3)	0	84
Rainwater (1)	Cleaning (1/1)	0	0

As bottled water and the galon—primarily used for drinking and cooking respectively—are perceived as being higher quality water, they generally cost more than water used for cleaning. The cheapest and least time-intensive water source for cleaning water is piped water from PDAM. However, only 33% of households interviewed had access to this water source, likely because water infrastructure is costly to upgrade, making it challenging to

connect new homes to the pre-existing piped network. However, households who are unable to receive water from this source—either because they are not connected or insufficient water is being supplied to the island—can still access this water source by purchasing it from their neighbors. In fact, this is the most common approach for obtaining water used for cleaning, with 75% of interviewed households engaging in this practice. As seen in Figure 4.4-A, neighbors from whom this water may be purchased typically have piped water access from PDAM and store water in drums beneath their home. Serving as a buffer for when the intermittent piped water supply is not flowing, this water can also be resold to neighbors. While neighbors can collect this water by manually transporting back to their home using buckets, in some cases neighbors will connect directly to their neighbor's PDAM water supply (as seen in Figure 4.4-B), although this is usually a special arrangement between relatives living in neighboring households. However, not all households have neighbors from whom they can purchase water. As a result, the second most common source for cleaning water is traveling off-island to collect water from freshwater wells located along the coast of mainland Sumbawa. As seen in Figure 4.4-C, households will travel by boat to collect water from these wells every 2-3 days. The fuel and time costs associated with this collection process makes off-island freshwater wells the most costly and time-intensive water source for cleaning. Water tankers are also a significant source used for cleaning. By trucking in a large tank of water, these tankers charge households for how much water they withdraw. As will be discussed later, these water tankers are often large and cannot access many regions of the island, which is likely why this water source is used less than the off-island freshwater wells, despite being cheaper and less time-intensive. Lastly, on-island brackish water wells and rainwater capture are also used, however they are used significantly less than other sources. The brackish water has a higher salinity than the other sources discussed, which explains why it is used exclusively for cleaning, if at all. Meanwhile, not many households appear to have rainwater harvesting equipment installed, which may explain why only one household reported using this water source (See Figure 4.4-D).

When disaggregating this data by household type, it becomes evident that exterior households experience the greatest hardships when it comes to water access. As previously mentioned, exterior households are often built most recently and, therefore, are less likely to have access to the piped water network. Furthermore, exterior households are located the furthest from homes that are connected to the piped network—as well as the main roads used by water tankers—forcing them to rely on the more expensive and time-intensive freshwater wells located off-island. As seen in Table 4.2, this results in exterior households spending the most time and money on collecting water. Meanwhile, these barriers to water access result in exterior households collecting the least amount of water on a per person basis. To put these values into context, the minimum water required for human domestic needs (including drinking, basic sanitation services, human hygiene, and food preparation) ranges between 27 and 200 liters per person per day,[175] with the World Health Organization recommending at least 70 liters per person per day in emergency situations.[176] This suggests that all households—regardless of location on Bungin Island—are subsisting on minimum wa-

Figure 4.4: Various water sources for households on Bungin Island. (A) Water drums used to store water from the intermittent piped water supply. (B) Water hose channeling water from one household to a neighboring one. (C) Collecting water by boat from a freshwater well located along the coast of mainland Sumbawa. (D) Homemade rainwater harvesting contraption installed onto the roof of a household on Bungin Island.

ter requirements, with exterior households persisting under emergency-like conditions with regards to water access.

Table 4.2: Water access for different household types on Bungin Island.

Household Type	**Piped Water Access**	**Time Collecting [hrs / week]**	**Household Spending on Water [IDR / week]**	**Water Collected [L / person / day]**
Central	67%	3.3	188,000	155
Intermediate	33%	2.7	151,000	126
Exterior	17%	3.5	200,000	77

Although not included on Table 4.2, there is also a discrepancy among household types with regards to water storage methods. When asked how the water is stored, 100% of central households and 67% of intermediate households reported using closed containers for

storage, with 33% of intermediate households using a mix of open and closed containers. For exterior households, 50% of households reported using closed containers, 17% reported using a mix of open and closed containers, and 33% reported using open containers only. Water storage is an important consideration for water disparities, as open storage containers puts households at greater risk of water contamination and exposure to waterborne illnesses.[177] While all of these indicators suggest exterior households face the greatest challenges for water access, it should be noted that the majority (67%) of all households interviewed expressed dissatisfaction with their current water circumstance. Prominent grievances regarding water services included concerns over rising costs of water, inconsistencies in water quality, and uncertainty about water availability in the future.

Feasibility Analysis for a Sustainable Desalination Technology

While all the residents of Bungin Island face a variety of challenges when it comes to water access, it is generally accepted that those living in the exterior portion of the island face the greatest water burden. In addition to our analysis, this conclusion was reaffirmed when residents were asked to identify which households face the greatest challenges when it comes to water access. In response to this question, nearly all respondents specified households located on the northeast edge of Bungin Island (see Figure 4.5-A). This region coincides with the location of where a majority of new homes are being built. As previously discussed, these homes generally do not have piped water access. Additionally, as they are located furthest away from homes that do have piped water access, it is less feasible for them to purchase and transport water from their neighbors. Meanwhile, the roads between these homes are either narrow or man-made bridges that cannot support vehicles (see Figure 4.5-B). As a result, the water tankers that are often deployed in emergencies to alleviate water stress cannot access these exterior households (Figure 4.5-C) and are therefore an unsuitable intervention for improving water access.

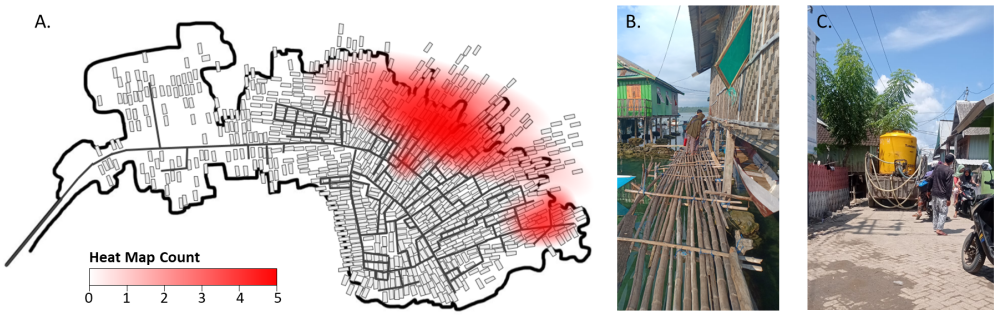

Figure 4.5: The disproportionate water burden faced by exterior households. (A) Heat map informed by interviewed households indicating which households face the greatest challenges to water access. (B) Man-made bridges connecting households located on the exterior portion of Bungin Island. (C) Water tankers used to provide water to Bungin Island that can only access main roads.

Given the disproportionate water burden placed on exterior households, it was concluded that the feasibility of a sustainable desalination technology should be evaluated based on their requirements and preferences. Being located on the exterior portion of the island, these households are in close proximity to the ocean and a majority (67%) of interviewed households have access to a boat during the day. As many of these households already obtain water from the freshwater wells located off-island, and given that there is limited undeveloped land space on Bungin Island, we posit that a sustainable desalination technology could be a floating device that is accessible by boat. When asked their preference between collecting water from a floating device themselves or having someone else collect and distribute the water on-island, 80% of respondents from exterior households preferred to collect the water themselves. Rather than relying on the piped infrastructure to supply this water, we believe that the pre-existing practice of buying and selling water to neighbors could be a more equitable means of distribution. When water is purchased from a neighbor, it is generally transported manually using buckets or pumped short distances via hose. As a result, it is less likely that water generated in the exterior portion of the island would be transported great distances, allowing for these water resources to be retained where the water need is greatest.

In addition to these insights, households were asked how much they would be willing to pay for this water. Interestingly, the stated willingness to pay was lowest for exterior households, who—on average—would pay 47 IDR per liter, whereas intermediate and central households would pay 67 and 96 IDR per liter, respectively. While nearly all households reported that they would be comfortable using the water for cleaning, 58% of all respondents also specified that they would be comfortable using this water for cooking, with 80% of exterior households, specifically, expressing this preference. Furthermore, 83% would consider using this water to drink if it was demonstrated to be clean and healthy. Beyond these potential uses, interviewees advised that the floating device should not be located along the southern and southeastern edges of the island, as this is where Bungin Island's main dock is located and these waters experience the greatest boat traffic. However, it was mentioned that it is important to place the device somewhere public where everyone can know its location and have access to it. While locating the device away from discharge points of human-generated wastewater is also a priority, this specific consideration was not identified in any of the interviews, potentially because of lacking centralized sanitation services. However, this hypothesis requires further investigation into the existing sanitation infrastructure.

4.5 Implications for a Desalination Technology based on 3D-ISVG

Our survey indicates that the exterior households on the Bungin island would greatly benefit from a decentralized desalination device that could provide cheap and reliable water

resources. A 3D-ISVG technology has the potential of meeting the needs with the following advantages:

- *Passive Operation* - 3D-ISVG is able to desalinate seawater through a passive process, meaning that no electricity is necessary for operation. The only requirements for operation are direct access to seawater and sunlight.
- *No Competition for Land Use* - As a 3D-ISVG technology would require direct access to seawater, a floating device is being proposed. This would allow the desalination system to not compete for already limited land on Bungin Island.
- *Low Capital Investment* - The materials used for 3D-ISVG are relatively straightforward to synthesize and could potentially be sourced and processed locally. This would reduce capital investment and shorten supply chains for manufacturing these devices.
- *Simple Maintenance* - The resiliency to the impacts of inorganic scaling would allow a 3D-ISVG device to operate without the traditional decline in performance due to the buildup of scale. Furthermore, 3D-ISVG structures can be designed to shed salt crystals when they form, which can potentially be engineered to reduce maintenance requirements.

As the development of a desalination technology using 3D-ISVG is still in its early stages, there are a variety of factors that could impact its potential design (see Figure 4.6-A). As a continuous water supply is required for interfacial solar vapor generation, a floating device would place the ISVG material in close proximity to the ocean water that it would be treating. Furthermore, a floating device could be located away from housing or other building structures that could potentially shade the device from sunlight during the day, maximizing 3D-ISVG's omni-directional light utilization. Also in our previous work,[66] we demonstrated the extraordinary enhancement of evaporative flux when exposed to forced convection or wind. While the condensation of water vapor would require a closed device, we propose outfitting the device with a vertical-axis wind turbine (VAWT) that can take advantage of coastal winds prevalent around Bungin Island, blowing at an average speed of 7.5 m/s.[178] Directly utilizing this wind, the VAWT could mechanically rotate a circulation fan located within the device (see Figure 4.6-B). Not only would this boost evaporation, but it would circulate humid air away from the 3D-ISVG materials to a separate chamber located beneath the ocean surface. Shaded by the upper part of the device, the lower chamber would have a cooler temperature to promote condensation. Lastly, preliminary evidence indicates that 3D-ISVG has a high resilience to the impacts of inorganic scaling. While this finding has the potential to extend operation time between maintenance visits, the device should be designed to minimize any and all maintenance requirements so that the device does not fall into disrepair.

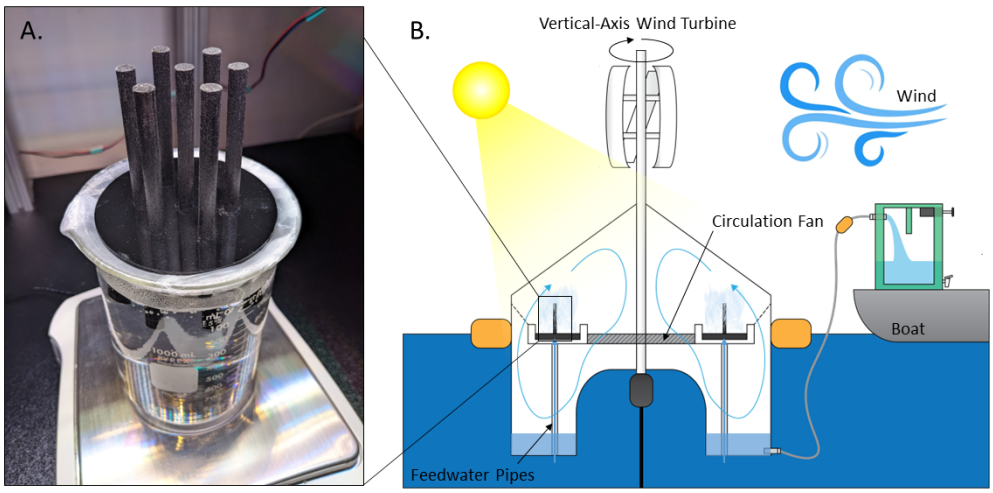

Figure 4.6: Implications for a 3D-ISVG desalination technology. (A) An array of 3D cylindrical materials used for interfacial solar vapor generation. (B) Design features of a 3D-ISVG desalination technology accounting for contextual factors surrounding water access on Bungin Island.

4.6 Conclusions & Future Outlook

This work aimed to understand the specific challenges to water access experienced on Bungin Island, and how these insights should be used to inform the feasibility and design of a sustainable desalination technology using 3D-ISVG. By interviewing households located in the central, intermediate, and exterior regions of the island, it was found that exterior households face the greatest water burden: having access to the least number of water sources, collecting the least amount of water per person, and spending the most time and money on collecting water. As a result, these exterior households were the focus of a feasibility analysis for a sustainable desalination technology. Based on this analysis, it was determined that the desalination technology should be a floating device located in close proximity to the exterior households. Furthermore, this water should be distributed by the pre-existing practice of buying/selling water among neighbors to ensure water generated by this device promotes water access for exterior households first. Finally, these insights were combined with recent findings on the specific advantages of 3D-ISVG to propose design considerations for a sustainable desalination technology using 3D-ISVG.

As previously discussed, 3D-ISVG has many specific advantages that make it amenable to Bungin Island's context. ISVG requires direct access to seawater and sunlight, which would be abundant for a floating device. The ISVG process is passive—requiring no electrical input—reducing both capital costs and the need for technical maintenance. And the performance of 3D-ISVG materials can be significantly enhanced by utilizing coastal winds, while 3D-ISVG's resiliency to inorganic fouling can extend operation before maintenance is

required. However, 3D-ISVG is not without its drawbacks. As an early-stage technology, 3D-ISVG still has many technical aspects that need to be resolved, including in-depth investigations into the condensation of water vapor produced by ISVG, potential risks of biofouling, and long-term salt management. Furthermore, 3D-ISVG should not be the only technology considered to improve water access for Bungin Island. A floating photovoltaic-powered reverse osmosis (PV-RO) system could also meet the criteria identified in this analysis. However, reliable access to high-grade energy, supply chains for equipment and chemicals, and technical expertise for maintenance[158] would be necessary for the successful operation of a floating PV-RO, and to avoid the same fate of the decommissioned desalination plant that was installed on Bungin Island in 2018.(Samawa, 2018) Rainwater capture is another option that could be used to augment water supplies, and is currently being used by some households. However, access to this water source would be seasonal, providing additional water in times of the year when water is already plentiful. Moreover, exterior households that are built directly above the ocean have less space to store captured rainwater, making this option less feasible for the households that would need it most. Lastly, passive atmospheric water harvesting (AWH)—note that active AWH would have the similar constraints to a PV-RO system—is an emerging approach that extracts water directly from the air. While the humid climate of Bungin Island is favorable for this approach,[179] many of the sorbents used for AWH release water as vapor and face the same challenges as ISVG with regards to condensation.[180] Additionally, these sorbents often only undergo one water release cycle per day, resulting in low daily water yields of 0.045 to 0.095 L per kg of material.[181]

While this work was able to establish certain trends with regards to household experiences with water on Bungin Island, expanding the number of households interviewed would increase the robustness of this analysis. This would be especially important for determining a more accurate value for the willingness to pay for water. Furthermore, this analysis only identified which water sources were used by households, while the underlying logic that goes into deciding which water source to use and when was not explored. Specifically, the practice of buying and selling water from neighbors warrants greater scrutiny, especially as it was proposed as the primary method for distribution for a sustainable desalination technology. While 58% of interviewed households identified purchasing water from a neighbor as a primary water source, 0% of interviewed households self-identified as selling water, despite 33% of households having access to piped water from PDAM. Additionally, this work did not investigate potential gender disparities with respect to water collection. Although the high-level analysis presented here did not indicate significant gender disparities, it is unclear which household members are responsible for collecting water from which water sources. As each water source requires a different amount of time and effort to access, there may be gender disparities that are hidden in this preliminary analysis.

Lastly, this work is intended to encourage researchers studying ISVG materials to begin exploring application-relevant questions. For example: How is the long-term performance of 3D-ISVG impacted by operating on seawater? How should a device be designed to minimize

maintenance requirements? How can a 3D-ISVG device be designed to maximize the use of forced convection generated by a VAWT? What is the practical water production rate that can be achieved by one of these devices? How is water production impacted by local climate and seasonality? While the social and technical questions presented here would traditionally be investigated separately, it is the hallmark of Development Engineering to grapple with the complex interactions between context-specific factors and technology design. As ISVG continues to be developed into a sustainable desalination technology, both the application context and the people involved should have an active role in the technology design and implementation.

Chapter 5

What's Next for Interfacial Solar Vapor Generation?

5.1 Outlook for Interfacial Solar Vapor Generation

This dissertation has chronicled the development of interfacial solar vapor generation as a field, from the carbon-based, double-layered structure introduced by Ghasemi et al. in 2014[14] to our feasibility analysis of a sustainable desalination technology utilizing 3D-ISVG for a small-island community context. As the field has grown, several key advantages of ISVG have emerged:

- *Sustainable* - ISVG can channel energy from a variety of sources—at extremely high efficiencies—toward evaporation, including omni-directional sunlight, ambient heat, and forced convection from wind.
- *Low-Cost* - The material requirements for ISVG (porous material for light-absorption, insulation for heat localization, and mechanism for water replenishment) are actually quite easy to achieve. As a result the materials and fabrication methods used to synthesize ISVG materials can be relatively low in cost and thus may provide solutions in development engineering.
- *Off-Grid* - Deriving the energy for evaporation from natural sources, ISVG can operate without any electrical input. As a result, much of the surrounding infrastructure that is required for other water treatment technologies may not be necessary for ISVG.

However, ISVG is not without its drawbacks. In a recent theoretical analysis, showed that ISVG materials operating at 100% solar-vapor conversion efficiency could only achieve a specific water productivity (SWP) of 2.4 LMH (without the recovery of latent heat).[157] In contrast, a photovoltaic-powered reverse osmosis (PV-RO) system could have a solar-utilization efficiency of 35%, but achieve a SWP of 125 LMH. While this analysis did not

account for alternative energy sources that can contribute to evaporation, as has been demonstrated for 3D-ISVG materials,[66] it still highlights the fact that the SWP for ISVG will likely remain an order of magnitude below PV-RO for seawater desalination applications. Nevertheless, ISVG may have key advantages in non-traditional applications, such as desalination in low-resource settings or treatment of hypersaline brines.

What follows are recommended avenues of research to guide the ISVG field as it begins to explore new frontiers. These research recommendations have been organized into four categories: material advancements, understanding complex mechanisms, application-oriented evaluation, and technological design.

5.2 Material Advancements

As the exploration of 3D-ISVG materials are still in their early stages, there are a wide range of 3D structures still to be explored. Specifically, 3D-ISVG materials with a high aspect ratio (or a high height dimension) warrant greater investigation to deepen our understanding of tradeoffs between water wicking height and evaporative flux. Consistency in how the performance of these materials are reported is critical though. While solar-vapor conversion efficiency was previously the metric used to compare the performance of various ISVG materials, this metric is less meaningful for 3D-ISVG materials. Now that the dominant energy source driving evaporation is no longer sunlight (but typically ambient heat), accounting for the contributions of alternative energy sources has made computing evaporation efficiency challenging, especially for complex 3D-ISVG structures. As we demonstrated in our work,[66] obtaining a value for evaporation efficiency requires accounting for evaporative flux, direct light irradiance, diffuse light irradiance, surface temperature, bulk water temperature, ambient temperature, and ambient humidity in both dark and light conditions. As all of these measurements are subject to error, evaporation efficiency ends up being a poor metric of comparison for 3D-ISVG materials. Since the ultimate goal of ISVG is to produce water, a better metric for comparison is the evaporative flux under light conditions. Traditionally, this is measured under 1-sun conditions (1 $kW\ m^{-2}$) with pure water. As 3D-ISVG materials can be complex in their geometries, these values should be reported with their corresponding evaporation area index (EAI) or the ratio to total surface area for evaporation relative to its projected ground area. The evaporative flux under dark conditions (0 $kW\ m^{-2}$) should also be reported, and not subtracted from the evaporative flux in light conditions (as was the norm for computing solar-vapor conversion efficiency). Lastly, the ambient temperature and humidity under both light and dark conditions should always be reported with their corresponding evaporative flux rates as well.

There is still interesting research exploring the ability of hydrogels to preferentially evaporate intermediate water and patterned surfaces to promote the formation of water clusters, but definitive evidence of these phenomena is still lacking. As the high amount of energy required

for evaporation is the bottleneck between ISVG and other higher-throughput solar desalination technologies, progress in material development to enhance these phenomena would be a game changer. However, these phenomena have only been observed in highly controlled settings and the preservation of this behavior in more practical operating conditions has not been explored.

Meanwhile—due to the simplicity of 3D-ISVG—it has an advantage as a water treatment technology in low-resource settings. Therefore, the field would benefit from an investigation into sustainable materials and fabrication processes. The carbonization of biomass has recently been gaining popularity because (1) biomass feedstock tends to have an inherent 3D shape and (2) conversion of biomass into a 3D-ISVG material can be achieved through simple carbonization.[182] Some interesting materials that have arisen from this approach have included carbonized corn stalks,[183] sunflower heads,[118] and lotus seed pods.[184] Pre-processing of these materials is common to improve performance of the resulting 3D-ISVG material. However, these variations in material synthesis have a cost associated with them. Therefore, it is recommended that further studies include fabrication costs as a means of comparison between sustainable 3D-ISVG materials.[185]

5.3 Understanding Complex Mechanisms

As the ISVG field transitioned from 2D to 3D materials, an entirely new dimension of complexity was introduced into the field. Not only do additional energy sources now have to be accounted for, but the 3D-ISVG material can now have complex interactions with itself. To maximize evaporative flux rates, it would be ideal to maximize the surface area for evaporation while minimizing the spatial footprint of the 3D-ISVG array. However, packing 3D-ISVG materials too close together can block sunlight and cause shading on adjacent 3D-ISVG materials. Additionally, packing materials too close together can create local regions of high humidity that would impede the evaporative flux. Therefore, research is needed to optimize on how closely 3D-ISVG materials can be packed together and how this varies as a function of latitude, meteorological conditions, and wind availability.

Furthermore, there has been a lack of attention paid to the mechanism and impacts of fouling on long-term ISVG performance. While there have been some preliminary studies investigating simple inorganic scaling behavior of sodium chloride,[65, 186, 134, 187] these studies may be misleading as the salt precipitation behavior of sodium chloride is somewhat unique,[188] and the changes significantly from salt species to salt species, as well as for mixtures.[189] Moreover, other forms of fouling have been widely ignored. Biofouling, specifically, has the potential to severely impact the efficacy of 3D-ISVG in real-world applications. As 3D-ISVG relies on capillary action to wick water to additional surfaces for evaporation, it is suspected that the biological contamination of the (often biomass-based) 3D-ISVG could disrupt these water flow pathways and gradually erode the structural in-

tegrity of the material. For this reason, long-term testing in application-relevant conditions is desperately needed to understand the full potential of 3D-ISVG as a technology.

5.4 Application-Oriented Evaluation

As previously mentioned, ISVG has competitive advantages in specific applications, such as desalination in low-resource settings or treatment of hypersaline brines. Additionally, other studies have shown the applicability of ISVG materials for energy generation,[190, 191] sterilization,[192, 193] and chemical reactions.[194, 195] In order to develop a deeper understanding of how ISVG will perform in these applications it is important to evaluate in application-relevant conditions, with respect to feedwater quality, daily light availability, and local meteorological conditions. Brine Management will likely be one of the most prominent applications for ISVG, as minimum and zero liquid discharge practices are becoming more widespread.[11] In fact, the reported performance data for most ISVG materials is actually more relevant to evaporation-only applications because ISVG materials are almost always evaluated in open-air conditions, where the water vapor generated by the ISVG material does not accumulate around the material and impede its evaporation rate. Brine management—with higher concentrations of potential species of interest—also presents opportunities for resource recovery. Many researchers have begun studying how ISVG could be used to isolate and recover minerals and metals in high purities. Finally—as explored in this dissertation—ISVG has potential in seawater desalination applications, specifically in low-resource settings. However, significant research is still required to close the loop between evaporation and condensation before ISVG can be developed into a technology. Meanwhile, Development Engineering emphasizes that no two contexts are the same and thoughtful community engagement is paramount for evaluating the feasibility of any intervention. All communities have unique relationships with their water resources, and it is essential to understand the political, social, and historical roots of this relationship before trying to co-develop any kind of solution.

5.5 Technological Design

The key challenge for an ISVG-based desalination technology is condensing water vapor without impeding high rates of evaporation. This is challenging because the rate of evaporation is maximized in hot and arid conditions, whereas the rate of condensation is maximized in cold and humid conditions. Additionally, condensation must contend with physical limitations that impede its rate, including water droplet nucleation, coalesces of droplets, and physical removal of larger droplets from the condensing surface. Traditional solar still tries to achieve evaporation and condensation in a single stage, with condensation often serving as the rate-limiting step for water production rates.[196] As proposed in Chapter 4, evaporation and condensation should occur in separate stages, but the transportation of water vapor

from stage to stage is challenging without the precision of electric fans. While this would undermine the "off-grid" advantage of ISVG, this could enable the introduction of multiple stages for evaporation and condensation. This is significant because the energy consumed by evaporation is released by condensation, and by linking evaporation-condensation stages together this heat can effectively be recycled to evaporate additional water in a subsequent stage. This phenomenon can be quantified as the gained output ratio (GOR), or how much distilled water can be condensed from the vaporization of 1 kg of water. As a point of comparison, the multiple stages used by conventional thermal desalination systems allow these technologies to achieve GOR values as high as 15. If similar GOR values could be achieved by an ISVG-based desalination technology, the specific water production is estimated to be around 22 LMH.[157]

Finally, a techno-economic analysis could be conducted to understand the impacts of introducing electrical components into an ISVG-based technology on the levelized cost of water. Other features that warrant exploration include the introduction of light concentrators and thermal collectors. Additionally, easy-of-maintenance with respect to fouling and salt-removal should also be considered in technology design. Lastly, these designs should be iterated and improved upon based on the results of pilot testing and user-centered feedback.

Bibliography

[1] Hayley Leck et al. "Tracing the water–energy–food nexus: Description, theory and practice". In: *Geography Compass* 9.8 (2015), pp. 445–460.

[2] Xavier Leflaive. "Water Outlook to 2050: The OECD calls for early and strategic action". In: *Global Water Forum*. 2012.

[3] Zbigniew W Kundzewicz and Valentina Krysanova. "Climate change and stream water quality in the multi-factor context". In: *Climatic Change* 103.3 (2010), pp. 353–362.

[4] Edward Jones et al. "The state of desalination and brine production: A global outlook". In: *Science of the Total Environment* 657 (2019), pp. 1343–1356.

[5] Menachem Elimelech and William A Phillip. "The future of seawater desalination: energy, technology, and the environment". In: *science* 333.6043 (2011), pp. 712–717.

[6] Equinox Center. "San Diego's Water Sources: Assessing the Options". In: *San Diego, CA* (2010).

[7] Paolo Roccaro. "Treatment processes for municipal wastewater reclamation: The challenges of emerging contaminants and direct potable reuse". In: *Current Opinion in Environmental Science & Health* 2 (2018), pp. 46–54.

[8] Fang Tang et al. "Effects of chemical agent injections on genotoxicity of wastewater in a microfiltration-reverse osmosis membrane process for wastewater reuse". In: *Journal of hazardous materials* 260 (2013), pp. 231–237.

[9] Yolanda Fernández-Torquemada et al. "Dispersion of brine discharge from seawater reverse osmosis desalination plants". In: *Desalination and Water Treatment* 5.1-3 (2009), pp. 137–145.

[10] Muftah H El-Naas. "Reject brine management". In: *Desalination, trends and technologies* (2011), pp. 237–252.

[11] Tiezheng Tong and Menachem Elimelech. "The global rise of zero liquid discharge for wastewater management: drivers, technologies, and future directions". In: *Environmental science & technology* 50.13 (2016), pp. 6846–6855.

[12] Oara Neumann et al. "Solar vapor generation enabled by nanoparticles". In: *ACS nano* 7.1 (2013), pp. 42–49.

[13] Zhenhui Wang et al. “Bio-inspired evaporation through plasmonic film of nanoparticles at the air–water interface”. In: *Small* 10.16 (2014), pp. 3234–3239.

[14] Hadi Ghasemi et al. “Solar steam generation by heat localization”. In: *Nature communications* 5.1 (2014), pp. 1–7.

[15] Haoyu Bai, Tianhong Zhao, and Moyuan Cao. “Interfacial solar evaporation for water production: from structure design to reliable performance”. In: *Molecular Systems Design & Engineering* 5.2 (2020), pp. 419–432.

[16] Liangliang Zhu et al. “Recent progress in solar-driven interfacial water evaporation: Advanced designs and applications”. In: *Nano Energy* 57 (2019), pp. 507–518.

[17] Yanming Liu et al. “A bioinspired, reusable, paper-based system for high-performance large-scale evaporation”. In: *Advanced Materials* 27.17 (2015), pp. 2768–2774.

[18] Lin Zhou et al. “Self-assembly of highly efficient, broadband plasmonic absorbers for solar steam generation”. In: *Science advances* 2.4 (2016), e1501227.

[19] Jie Liang et al. “Plasmon-enhanced solar vapor generation”. In: *Nanophotonics* 8.5 (2019), pp. 771–786.

[20] Mingwei Zhu et al. “Plasmonic wood for high-efficiency solar steam generation”. In: *Advanced Energy Materials* 8.4 (2018), p. 1701028.

[21] Peijin Ying et al. “Band gap engineering in an efficient solar-driven interfacial evaporation system”. In: *ACS applied materials & interfaces* 12.29 (2020), pp. 32880–32887.

[22] Qing Zhu et al. “A hydrogenated metal oxide with full solar spectrum absorption for highly efficient photothermal water evaporation”. In: *The Journal of Physical Chemistry Letters* 11.7 (2020), pp. 2502–2509.

[23] Tieshan Yang et al. “Carbon-based absorbers for solar evaporation: Steam generation and beyond”. In: *Sustainable materials and technologies* 25 (2020), e00182.

[24] Wen He et al. “Structure development of carbon-based solar-driven water evaporation systems”. In: *Science Bulletin* 66.14 (2021), pp. 1472–1483.

[25] Weixin Guan, Youhong Guo, and Guihua Yu. “Carbon materials for solar water evaporation and desalination”. In: *Small* 17.48 (2021), p. 2007176.

[26] Qisheng Jiang et al. “Bilayered biofoam for highly efficient solar steam generation”. In: *Advanced Materials* 28.42 (2016), pp. 9400–9407.

[27] Yan Li et al. “Solar absorber with tunable porosity to control the water supply velocity to accelerate water evaporation”. In: *Desalination* 511 (2021), p. 115113.

[28] Hanxue Liang et al. “Thermal efficiency of solar steam generation approaching 100% through capillary water transport”. In: *Angewandte Chemie International Edition* 58.52 (2019), pp. 19041–19046.

[29] Zhenxing Wang et al. "Confinement capillarity of thin coating for boosting solar-driven water evaporation". In: *Advanced Functional Materials* 31.22 (2021), p. 2011114.

[30] Wei Zhang et al. "Capillary-flow-optimized heat localization induced by an air-enclosed three-dimensional hierarchical network for elevated solar evaporation". In: *ACS applied materials & interfaces* 11.10 (2019), pp. 9974–9983.

[31] Xiuqiang Li et al. "Graphene oxide-based efficient and scalable solar desalination under one sun with a confined 2D water path". In: *Proceedings of the National Academy of Sciences* 113.49 (2016), pp. 13953–13958.

[32] Peng Wang. "Emerging investigator series: the rise of nano-enabled photothermal materials for water evaporation and clean water production by sunlight". In: *Environmental Science: Nano* 5.5 (2018), pp. 1078–1089.

[33] Zhen Yu et al. "Enhancing efficiency of carbonized wood based solar steam generator for wastewater treatment by optimizing the thickness". In: *Solar Energy* 193 (2019), pp. 434–441.

[34] Ning Xu et al. "Mushrooms as efficient solar steam-generation devices". In: *Advanced Materials* 29.28 (2017), p. 1606762.

[35] Yanpei Tian et al. "Carbonized cattle manure-based photothermal evaporator with hierarchically bimodal pores for solar desalination in high-salinity brines". In: *Desalination* 520 (2021), p. 115345.

[36] Zhejun Liu et al. "Extremely cost-effective and efficient solar vapor generation under nonconcentrated illumination using thermally isolated black paper". In: *Global Challenges* 1.2 (2017), p. 1600003.

[37] Peng-Fei Liu et al. "A mimetic transpiration system for record high conversion efficiency in solar steam generator under one-sun". In: *Materials today energy* 8 (2018), pp. 166–173.

[38] Seunghyun Hong et al. "Nature-inspired, 3D origami solar steam generator toward near full utilization of solar energy". In: *ACS applied materials & interfaces* 10.34 (2018), pp. 28517–28524.

[39] Xiuqiang Li et al. "Measuring conversion efficiency of solar vapor generation". In: *Joule* 3.8 (2019), pp. 1798–1803.

[40] Enas M Ahmed. "Hydrogel: Preparation, characterization, and applications: A review". In: *Journal of advanced research* 6.2 (2015), pp. 105–121.

[41] T Hatakeyema, A Yamauchi, and HJEPJ Hatakeyema. "Studies on bound water in poly (vinyl alcohol). Hydrogel by DSC and FT-NMR". In: *European Polymer Journal* 20.1 (1984), pp. 61–64.

[42] ZH Ping et al. "States of water in different hydrophilic polymers—DSC and FTIR studies". In: *Polymer* 42.20 (2001), pp. 8461–8467.

[43] Takahiko Terada, Yasushi Maeda, and Hiromi Kitano. "Raman spectroscopic study on water in polymer gels". In: *The Journal of Physical Chemistry* 97.14 (1993), pp. 3619–3622.

[44] Tao Wang and Sundaram Gunasekaran. "State of water in chitosan–PVA hydrogel". In: *Journal of applied polymer science* 101.5 (2006), pp. 3227–3232.

[45] Kazuhiro Hara Kazuhiro Hara et al. "Raman scattering study during the dehydration process of polyacrylamide gel". In: *Japanese journal of applied physics* 34.10R (1995), p. 5700.

[46] K Hara et al. "Elastic property and Raman spectrum evolutions during dehydration process of polyacrylamide gel". In: *Physica B: Condensed Matter* 219 (1996), pp. 526–528.

[47] Kushi Kudo et al. "Structural changes of water in poly (vinyl alcohol) hydrogel during dehydration". In: *The Journal of chemical physics* 140.4 (2014), p. 044909.

[48] Yurina Sekine and Tomoko Ikeda-Fukazawa. "Structural changes of water in a hydrogel during dehydration". In: *The Journal of chemical physics* 130.3 (2009), p. 034501.

[49] Fei Zhao et al. "Highly efficient solar vapour generation via hierarchically nanostructured gels". In: *Nature nanotechnology* 13.6 (2018), pp. 489–495.

[50] Asuka Fujii and Kenta Mizuse. "Infrared spectroscopic studies on hydrogen-bonded water networks in gas phase clusters". In: *International Reviews in Physical Chemistry* 32.2 (2013), pp. 266–307.

[51] Mitsuhiko Miyazaki et al. "Infrared spectroscopic evidence for protonated water clusters forming nanoscale cages". In: *Science* 304.5674 (2004), pp. 1134–1137.

[52] Youhong Guo et al. "Synergistic energy nanoconfinement and water activation in hydrogels for efficient solar water desalination". In: *ACS nano* 13.7 (2019), pp. 7913–7919.

[53] Fei Zhao et al. "Materials for solar-powered water evaporation". In: *Nature Reviews Materials* 5.5 (2020), pp. 388–401.

[54] Linlin Zang et al. "Nanofibrous hydrogel-reduced graphene oxide membranes for effective solar-driven interfacial evaporation and desalination". In: *Chemical Engineering Journal* 422 (2021), p. 129998.

[55] Youhong Guo et al. "Tailoring nanoscale surface topography of hydrogel for efficient solar vapor generation". In: *Nano letters* 19.4 (2019), pp. 2530–2536.

[56] Donald B Anderson. "Relative humidity or vapor pressure deficit". In: *Ecology* 17.2 (1936), pp. 277–282.

[57] Cornelius E Klots. "Evaporative cooling". In: *The Journal of chemical physics* 83.11 (1985), pp. 5854–5860.

[58] Haomin Song et al. "Cold vapor generation beyond the input solar energy limit". In: *Advanced Science* 5.8 (2018), p. 1800222.

[59] Xiuqiang Li et al. "Enhancement of interfacial solar vapor generation by environmental energy". In: *Joule* 2.7 (2018), pp. 1331–1338.

[60] *Why development engineering*. Jan. 2022. URL: https://developmentengineering.berkeley.edu/about/why-development-engineering/.

[61] Briana Collins. *Plans for water filtration system could also empower women*. Aug. 2019. URL: https://foxillinois.com/news/illinois-innovations/plans-for-water-filtration-system-could-also-empower-women.

[62] *Get to know bungin island the world's most populous island*. July 2020. URL: https://authentic-indonesia.com/blog/get-to-know-bungin-island-the-worlds-most-populous-island.

[63] Syed Imran Ali. "Engineering in solidarity: Hybridizing knowledge systems in humanitarian and international development work". In: *Procedia Engineering* 107 (2015), pp. 11–17.

[64] David I Levine, Alice M Agogino, and Martha A Lesniewski. "Design for Impact: A Development Engineering Graduate Program at UC Berkeley". In: (2016).

[65] Casey Finnerty et al. "Synthetic graphene oxide leaf for solar desalination with zero liquid discharge". In: *Environmental science & technology* 51.20 (2017), pp. 11701–11709.

[66] Casey TK Finnerty et al. "Interfacial Solar Evaporation by a 3D Graphene Oxide Stalk for Highly Concentrated Brine Treatment". In: *Environmental science & technology* 55.22 (2021), pp. 15435–15445.

[67] Robert L McGinnis et al. "Pilot demonstration of the NH3/CO2 forward osmosis desalination process on high salinity brines". In: *Desalination* 312 (2013), pp. 67–74.

[68] Sulaiman Al-Obaidani et al. "Potential of membrane distillation in seawater desalination: thermal efficiency, sensitivity study and cost estimation". In: *Journal of membrane science* 323.1 (2008), pp. 85–98.

[69] Yoshikazu Ito et al. "Multifunctional porous graphene for high-efficiency steam generation by heat localization". In: *Advanced Materials* 27.29 (2015), pp. 4302–4307.

[70] Chao Chang et al. "Efficient solar-thermal energy harvest driven by interfacial plasmonic heating-assisted evaporation". In: *ACS applied materials & interfaces* 8.35 (2016), pp. 23412–23418.

[71] Yang Liu et al. "Bioinspired bifunctional membrane for efficient clean water generation". In: *ACS applied materials & interfaces* 8.1 (2016), pp. 772–779.

[72] Yiming Liu et al. "Floatable, self-cleaning, and carbon-black-based superhydrophobic gauze for the solar evaporation enhancement at the air–water interface". In: *ACS applied materials & interfaces* 7.24 (2015), pp. 13645–13652.

[73] Rongzheng Wan and Guosheng Shi. "Accelerated evaporation of water on graphene oxide". In: *Physical Chemistry Chemical Physics* 19.13 (2017), pp. 8843–8847.

[74] Lin Zhou et al. "3D self-assembly of aluminium nanoparticles for plasmon-enhanced solar desalination". In: *Nature Photonics* 10.6 (2016), pp. 393–398.

[75] Yuan Ni et al. "Heat generation and stability of a plasmonic nanogold system". In: *Journal of Physics D: Applied Physics* 49.5 (2015), p. 055302.

[76] Kyuyoung Bae et al. "Flexible thin-film black gold membranes with ultrabroadband plasmonic nanofocusing for efficient solar vapour generation". In: *Nature communications* 6.1 (2015), pp. 1–9.

[77] Panpan Zhang et al. "Vertically aligned graphene sheets membrane for highly efficient solar thermal generation of clean water". In: *ACS nano* 11.5 (2017), pp. 5087–5093.

[78] Xiaozhen Hu et al. "Tailoring graphene oxide-based aerogels for efficient solar steam generation under one sun". In: *Advanced materials* 29.5 (2017), p. 1604031.

[79] Xiuqiang Li et al. "Three-dimensional artificial transpiration for efficient solar wastewater treatment". In: *National Science Review* 5.1 (2018), pp. 70–77.

[80] Sunxiang Zheng et al. "Swelling of graphene oxide membranes in aqueous solution: characterization of interlayer spacing and insight into water transport mechanisms". In: *ACS nano* 11.6 (2017), pp. 6440–6450.

[81] Baoxia Mi. "Graphene oxide membranes for ionic and molecular sieving". In: *Science* 343.6172 (2014), pp. 740–742.

[82] Hubiao Huang et al. "Ultrafast viscous water flow through nanostrand-channelled graphene oxide membranes". In: *Nature communications* 4.1 (2013), pp. 1–9.

[83] Meng Hu and Baoxia Mi. "Layer-by-layer assembly of graphene oxide membranes via electrostatic interaction". In: *Journal of Membrane Science* 469 (2014), pp. 80–87.

[84] K Kim et al. *Novel water filtration of saline water in the outermost layer of mangrove roots Sci.* 2016.

[85] Catherine E Lovelock and Ilka C Feller. "Photosynthetic performance and resource utilization of two mangrove species coexisting in a hypersaline scrub forest". In: *Oecologia* 134.4 (2003), pp. 455–462.

[86] MR Atkinson et al. "Salt regulation in the mangroves Rhizophora mucronata Lam. and Aegialitis annulata Rbr". In: *Australian Journal of Biological Sciences* 20.3 (1967), pp. 589–600.

[87] S William, JR Hummers, Richard E Offeman, et al. "Preparation of graphitic oxide". In: *J. Am. Chem. Soc* 80.6 (1958), pp. 1339–1339.

[88] Daniela C Marcano et al. "Improved synthesis of graphene oxide". In: *ACS nano* 4.8 (2010), pp. 4806–4814.

[89] Shibing Ye, Jiachun Feng, and Peiyi Wu. "Highly elastic graphene oxide–epoxy composite aerogels via simple freeze-drying and subsequent routine curing". In: *Journal of Materials Chemistry A* 1.10 (2013), pp. 3495–3502.

[90] Marilla Lamb et al. "A synthetic leaf: the biomimetic potential of graphene oxide". In: *Bioinspiration, Biomimetics, and Bioreplication 2015*. Vol. 9429. International Society for Optics and Photonics. 2015, p. 942915.

[91] Stephen C Sillett et al. "How do tree structure and old age affect growth potential of California redwoods?" In: *Ecological Monographs* 85.2 (2015), pp. 181–212.

[92] Jing-min Li et al. "A bio-inspired micropump based on stomatal transpiration in plants". In: *Lab on a Chip* 11.16 (2011), pp. 2785–2789.

[93] Renyuan Li et al. "MXene Ti3C2: an effective 2D light-to-heat conversion material". In: *ACS nano* 11.4 (2017), pp. 3752–3759.

[94] Lianbin Zhang et al. "Hydrophobic light-to-heat conversion membranes with self-healing ability for interfacial solar heating". In: *Advanced Materials* 27.33 (2015), pp. 4889–4894.

[95] Pieter Jan Cornelis Kuiper. "The effects of environmental factors on the transpiration of leaves, with special reference to stomatal light response". PhD thesis. Veenman, 1961.

[96] William Thomson. "4. On the equilibrium of vapour at a curved surface of liquid". In: *Proceedings of the Royal Society of Edinburgh* 7 (1872), pp. 63–68.

[97] Mansoureh Norouzi Rad et al. "Effects of grain and pore size on salt precipitation during evaporation from porous media". In: *Transport in Porous Media* 110.2 (2015), pp. 281–294.

[98] Nathalie JJ Breda. "Ground-based measurements of leaf area index: a review of methods, instruments and current controversies". In: *Journal of experimental botany* 54.392 (2003), pp. 2403–2417.

[99] C Adam Schlosser et al. "The future of global water stress: An integrated assessment". In: *Earth's Future* 2.8 (2014), pp. 341–361.

[100] M Sarai Atab, AJ Smallbone, and AP Roskilly. "An operational and economic study of a reverse osmosis desalination system for potable water and land irrigation". In: *Desalination* 397 (2016), pp. 174–184.

[101] Pei Xu et al. "Critical review of desalination concentrate management, treatment and beneficial use". In: *Environmental Engineering Science* 30.8 (2013), pp. 502–514.

[102] Akanksha K Menon et al. "Enhanced solar evaporation using a photo-thermal umbrella for wastewater management". In: *Nature Sustainability* 3.2 (2020), pp. 144–151.

[103] Jiebin Tang et al. "Realization of low latent heat of a solar evaporator via regulating the water state in wood channels". In: *ACS applied materials & interfaces* 12.16 (2020), pp. 18504–18511.

[104] Jianhua Zhou et al. "Development and evolution of the system structure for highly efficient solar steam generation from zero to three dimensions". In: *Advanced Functional Materials* 29.50 (2019), p. 1903255.

[105] Baoxia Mi, Casey Finnerty, and Kelly Conway. "Prospects of artificial tree for solar desalination". In: *Current Opinion in Chemical Engineering* 25 (2019), pp. 18–25.

[106] Zhen Yu et al. "Highly efficient solar vapor generator enabled by a 3D hierarchical structure constructed with hydrophilic carbon felt for desalination and wastewater treatment". In: *ACS applied materials & interfaces* 11.35 (2019), pp. 32038–32045.

[107] Panpan Zhang et al. "Three-dimensional water evaporation on a macroporous vertically aligned graphene pillar array under one sun". In: *Journal of Materials Chemistry A* 6.31 (2018), pp. 15303–15309.

[108] Zixiao Liu et al. "Continuously producing watersteam and concentrated brine from seawater by hanging photothermal fabrics under sunlight". In: *Advanced Functional Materials* 29.43 (2019), p. 1905485.

[109] Yuchao Wang et al. "Improved light-harvesting and thermal management for efficient solar-driven water evaporation using 3D photothermal cones". In: *Journal of Materials Chemistry A* 6.21 (2018), pp. 9874–9881.

[110] Feng Ni et al. "Micro-/macroscopically synergetic control of switchable 2d/3d photothermal water purification enabled by robust, portable, and cost-effective cellulose papers". In: *ACS applied materials & interfaces* 11.17 (2019), pp. 15498–15506.

[111] Yue Bian et al. "Carbonized Tree-Like Furry Magnolia Fruit-Based Evaporator Replicating the Feat of Plant Transpiration". In: *Global Challenges* 3.10 (2019), p. 1900040.

[112] Peng Xiao et al. "Rationally Programmable Paper-Based Artificial Trees Toward Multipath Solar-Driven Water Extraction from Liquid/Solid Substrates". In: *Solar Rrl* 3.7 (2019), p. 1900004.

[113] Yi Lu et al. "Implementing hybrid energy harvesting in 3D spherical evaporator for solar steam generation and synergic water purification". In: *Solar RRL* 4.9 (2020), p. 2000232.

[114] Yusuf Shi et al. "A 3D photothermal structure toward improved energy efficiency in solar steam generation". In: *Joule* 2.6 (2018), pp. 1171–1186.

[115] Qian Yang et al. "A high-efficiency and low-cost interfacial evaporation system based on graphene-loaded pyramid polyurethane sponge for wastewater and seawater treatments". In: *ACS Applied Energy Materials* 2.10 (2019), pp. 7223–7232.

[116] Ce Tu et al. "A 3D-structured sustainable solar-driven steam generator using superblack nylon flocking materials". In: *Small* 15.37 (2019), p. 1902070.

[117] Jinlei Li et al. "Over 10 kg m- 2 h- 1 evaporation rate enabled by a 3D interconnected porous carbon foam". In: *Joule* 4.4 (2020), pp. 928–937.

[118] Peng Sun et al. "3D-structured carbonized sunflower heads for improved energy efficiency in solar steam generation". In: *ACS applied materials & interfaces* 12.2 (2019), pp. 2171–2179.

[119] Yujin Sui et al. "A flowerlike sponge coated with carbon black nanoparticles for enhanced solar vapor generation". In: *Journal of Materials Science* 55.1 (2020), pp. 298–308.

[120] Xiujun Gao et al. "Artificial Mushroom Sponge Structure for Highly Efficient and Inexpensive Cold-Water Steam Generation". In: *Global Challenges* 2.12 (2018), p. 1800035.

[121] Yali Chen et al. "Blackbody-Inspired Array Structural Polypyrrole-Sunflower Disc with Extremely High Light Absorption for Efficient Photothermal Evaporation". In: *ACS Applied Materials & Interfaces* 12.41 (2020), pp. 46653–46660.

[122] Hongqiang Wang et al. "Artificial trees inspired by monstera for highly efficient solar steam generation in both normal and weak light environments". In: *Advanced Functional Materials* 30.48 (2020), p. 2005513.

[123] Jie Liu et al. "Surface-Carbonized Bamboos with Multilevel Functional Biostructures Deliver High Photothermal Water Evaporation Performance". In: *Advanced Sustainable Systems* 4.9 (2020), p. 2000126.

[124] Si Chen et al. "Plasmonic wooden flower for highly efficient solar vapor generation". In: *Nano Energy* 76 (2020), p. 104998.

[125] Qian Zhang et al. "Banyan-inspired hierarchical evaporators for efficient solar photothermal conversion". In: *Applied Energy* 276 (2020), p. 115545.

[126] Yang Geng et al. "Bioinspired Fractal Design of Waste Biomass-Derived Solar–Thermal Materials for Highly Efficient Solar Evaporation". In: *Advanced Functional Materials* 31.3 (2021), p. 2007648.

[127] Zhanjun Xie, Jintao Zhu, and Lianbin Zhang. "Three-Dimensionally Structured Polypyrrole-Coated Setaria viridis Spike Composites for Efficient Solar Steam Generation". In: *ACS Applied Materials & Interfaces* 13.7 (2021), pp. 9027–9035.

[128] Yang Sun et al. "High performance carbonized corncob-based 3D solar vapor steam generator enhanced by environmental energy". In: *Carbon* 179 (2021), pp. 337–347.

[129] Chaofan Zhang et al. "Solar vapor generator: A natural all-in-one 3D system derived from cattail". In: *Solar Energy Materials and Solar Cells* 227 (2021), p. 111127.

[130] Yudi Yang et al. "Low-Cost and High-Efficiency Solar-Driven Vapor Generation Using a 3D Dyed Cotton Towel". In: *Global Challenges* 3.9 (2019), p. 1900004.

[131] Linlin Zang et al. "Interfacial solar vapor generation for desalination and brine treatment: Evaluating current strategies of solving scaling". In: *Water Research* (2021), p. 117135.

[132] Ying Xu et al. "Origami system for efficient solar driven distillation in emergency water supply". In: *Chemical Engineering Journal* 356 (2019), pp. 869–876.

[133] Weigu Li et al. "Portable low-pressure solar steaming-collection unisystem with polypyrrole origamis". In: *Advanced Materials* 31.29 (2019), p. 1900720.

[134] Lei Wu et al. "Highly efficient three-dimensional solar evaporator for high salinity desalination by localized crystallization". In: *Nature communications* 11.1 (2020), pp. 1–12.

[135] Yaoxin Zhang, Sai Kishore Ravi, and Swee Ching Tan. "Systematic study of the effects of system geometry and ambient conditions on solar steam generation for evaporation optimization". In: *Advanced Sustainable Systems* 3.8 (2019), p. 1900044.

[136] Chenglong Guo et al. "Constructing 3D optical absorption holes by stacking macroporous membrane for highly efficient solar steam generation". In: *Renewable Energy* 159 (2020), pp. 944–953.

[137] Bo Shao et al. "A general method for selectively coating photothermal materials on 3D porous substrate surfaces towards cost-effective and highly efficient solar steam generation". In: *Journal of Materials Chemistry A* 8.46 (2020), pp. 24703–24709.

[138] Xianquan Zhang et al. "Nature-inspired design: p-toluenesulfonic acid-assisted hydrothermally engineered wood for solar steam generation". In: *Nano Energy* 78 (2020), p. 105322.

[139] Yue Bian et al. "Carbonized bamboos as excellent 3D solar vapor-generation devices". In: *Advanced Materials Technologies* 4.4 (2019), p. 1800593.

[140] Zhengtong Li et al. "Arched bamboo charcoal as interfacial solar steam generation integrative device with enhanced water purification capacity". In: *Advanced Sustainable Systems* 3.4 (2019), p. 1800144.

[141] Xuan Wu et al. "Evaporation above a bulk water surface using an oil lamp inspired highly efficient solar-steam generation strategy". In: *Journal of Materials Chemistry A* 6.26 (2018), pp. 12267–12274.

[142] Xuan Wu et al. "A photothermal reservoir for highly efficient solar steam generation without bulk water". In: *Science Bulletin* 64.21 (2019), pp. 1625–1633.

[143] Daniel Peter Storer et al. "Graphene and rice-straw-fiber-based 3D photothermal aerogels for highly efficient solar evaporation". In: *ACS applied materials & interfaces* 12.13 (2020), pp. 15279–15287.

[144] Linfeng Wang et al. "Three-dimensional wood-inspired bilayer membrane device containing microchannels for highly efficient solar steam generation". In: *ACS applied materials & interfaces* 12.21 (2020), pp. 24328–24338.

[145] Yuchao Wang, Xueyan Sun, and Shengyang Tao. "Rational 3D Coiled Morphology for Efficient Solar-Driven Desalination". In: *Environmental Science & Technology* 54.24 (2020), pp. 16240–16248.

[146] Ting Gao et al. "A cobalt oxide@ polydopamine-reduced graphene oxide-based 3D photothermal evaporator for highly efficient solar steam generation". In: *Tungsten* 2.4 (2020), pp. 423–432.

[147] Ting Gao et al. "A Hollow and Compressible 3D Photothermal Evaporator for Highly Efficient Solar Steam Generation without Energy Loss". In: *Solar RRL* 5.5 (2021), p. 2100053.

[148] Binglin Bai et al. "High-efficiency solar steam generation based on blue brick-graphene inverted cone evaporator". In: *Applied Thermal Engineering* 163 (2019), p. 114379.

[149] Ningning Cao et al. "A self-regenerating air-laid paper wrapped ASA 3D cone-shaped Janus evaporator for efficient and stable solar desalination". In: *Chemical Engineering Journal* 397 (2020), p. 125522.

[150] Yuxia Xu et al. "Microvessel-Assisted Environmental Thermal Energy Extraction Enabling 24-Hour Continuous Interfacial Vapor Generation". In: *ChemSusChem* 13.24 (2020), pp. 6635–6642.

[151] Baohua Yuan et al. "A Low-Cost 3D Spherical Evaporator with Unique Surface Topology and Inner Structure for Solar Water Evaporation-Assisted Dye Wastewater Treatment". In: *Advanced Sustainable Systems* 5.3 (2021), p. 2000245.

[152] Yuchao Wang et al. "Wettable photothermal hollow fibers arrays for efficient solar-driven desalination under omnidirectional illumination without salt precipitation". In: *Materials Today Energy* 16 (2020), p. 100391.

[153] Yida Wang et al. "Boosting solar steam generation by structure enhanced energy management". In: *Science Bulletin* 65.16 (2020), pp. 1380–1388.

[154] Yida Wang et al. "Same materials, bigger output: a reversibly transformable 2D–3D photothermal evaporator for highly efficient solar steam generation". In: *Nano Energy* 79 (2021), p. 105477.

[155] Shuai Li et al. "Simple Hierarchical Interface Design Strategy for Accelerating Solar Evaporation". In: *Macromolecular Materials and Engineering* 306.3 (2021), p. 2000640.

[156] Zhaochuan Chen, Qiang Li, and Xuemei Chen. "Porous Graphene/Polyimide Membrane with a Three-Dimensional Architecture for Rapid and Efficient Solar Desalination via Interfacial Evaporation". In: *ACS Sustainable Chemistry & Engineering* 8.36 (2020), pp. 13850–13858.

[157] Zhangxin Wang et al. "Pathways and challenges for efficient solar-thermal desalination". In: *Science advances* 5.7 (2019), eaax0763.

[158] Christopher A Mattson and Amy E Wood. "Nine principles for design for the developing world as derived from the engineering literature". In: *Journal of Mechanical Design* 136.12 (2014).

[159] Jamie Linton and Jessica Budds. "The hydrosocial cycle: Defining and mobilizing a relational-dialectical approach to water". In: *Geoforum* 57 (2014), pp. 170–180.

[160] Muge Akpinar-Elci and Hugh Sealy. "Climate change and public health in small island states and Caribbean countries". In: *Global climate change and public health*. Springer, 2014, pp. 279–292.

[161] UNEP Unesco-IHP. "Transboundary aquifers and groundwater systems of small island developing states: status and trends, summary for policy makers". In: *United Nations Environment Programme (UNEP), Nairobi* (2016).

[162] UNESCO. "Small Islands: Meeting the Challenges of Freshwater Resilience". In: (2019).

[163] William James Smith. "The place of rural, remote and least-wealthy small islands in international water development: the nexus of geography–technology sustainability in Chuuk State, Federated States of Micronesia". In: *Geographical Journal* 174.3 (2008), pp. 251–268.

[164] Heather M Murphy, Edward A McBean, and Khosrow Farahbakhsh. "Appropriate technology–A comprehensive approach for water and sanitation in the developing world". In: *Technology in Society* 31.2 (2009), pp. 158–167.

[165] Lin Zhou et al. "The revival of thermal utilization from the Sun: interfacial solar vapor generation". In: *National Science Review* 6.3 (2019), pp. 562–578.

[166] Lina Nilsson, Temina Madon, and S Shankar Sastry. "Toward a new field of development engineering: linking technology design to the demands of the poor". In: *Procedia Engineering* 78 (2014), pp. 3–9.

[167] World Health Organization et al. "Progress on household drinking water, sanitation and hygiene 2000-2020: five years into the SDGs". In: (2021).

[168] Sun-Kee Hong and Luchman Hakim. "Survey report: natural resource use, environmental management and the minorities in Indonesian islands". In: *J Mar Island Cult* 7.2 (2018), pp. 108–116.

[169] Dina Karlina. "Tradisi Nangung Rumah dalam Penataan Kawasan Permukiman Desa Pulau Bungin Kabupaten Sumbawa NTB". PhD thesis. Universitas Islam Negeri Alauddin Makassar, 2020.

[170] Jumat. *Uniknya Pulau Bungin*. July 2012. URL: https://travel.tempo.co/read/415124/uniknya-pulau-bungin.

[171] Rusdianto Samawa. *Bpk Dan KPK Harus Audit Proyek Desalinasi*. Apr. 2018. URL: https://www.swarasenayan.com/bpk-dan-kpk-harus-audit-proyek-desalinasi/.

[172] Susi Gustiana. *Pipa PDAM Terseret Banjir Bandang, Warga Pulau bungin sumbawa kesulitan air bersih*. Feb. 2022. URL: https://regional.kompas.com/read/2022/02/15/205706778/pipa-pdam-terseret-banjir-bandang-warga-pulau-bungin-sumbawa-kesulitan-air.

[173] Verry Lahamendu. "Penataan Permukiman Suku Bajo Di Pulau Bungin". In: *Prosiding Seminar Nasional Planoearth1 2017* (2017), pp. 171–177.

[174] Haris Firdaus. *Terikat Adat di Pulau Terpadat*. Apr. 2017. URL: https://www-beta.kompas.id/baca/utama/2017/04/07/terikat-adat-di-pulau-terpadat/.

[175] Peter H Gleick. "Basic water requirements for human activities: meeting basic needs". In: *Water international* 21.2 (1996), pp. 83–92.

[176] Robert Reed et al. *Technical notes on drinking-water, sanitation and hygiene in emergencies*. 2013.

[177] Peter Kjær Jensen et al. "Domestic transmission routes of pathogens: The problem of in-house contamination of drinking water during storage in developing countries". In: *Tropical Medicine & International Health* 7.7 (2002), pp. 604–609.

[178] Des Clics Nomades. *Sea water temperature in Pulau Bungin: Today and forecasts*. URL: https://www.seatemperatu.re/southeast-asia/sumbawa/pulau-bungin/.

[179] Ben Gido, Eran Friedler, and David M Broday. "Assessment of atmospheric moisture harvesting by direct cooling". In: *Atmospheric Research* 182 (2016), pp. 156–162.

[180] Dimitrios Nioras et al. "How Different Are Fog Collection and Dew Water Harvesting on Surfaces with Different Wetting Behaviors?" In: *ACS Applied Materials & Interfaces* 13.40 (2021), pp. 48322–48332.

[181] Farhad Fathieh et al. "Practical water production from desert air". In: *Science advances* 4.6 (2018), eaat3198.

[182] I Ibrahim et al. "Biomass-based photothermal materials for interfacial solar steam generation: A review". In: *Materials Today Energy* 21 (2021), p. 100716.

[183] Haotian Zhang et al. "Highly thermally insulated and superhydrophilic corn straw for efficient solar vapor generation". In: *ACS applied materials & interfaces* 12.14 (2020), pp. 16503–16511.

[184] Hao-Yu Zhao et al. "Lotus-inspired evaporator with janus wettability and bimodal pores for solar steam generation". In: *Cell Reports Physical Science* 1.6 (2020), p. 100074.

[185] Ahmed Mortuza Saleque et al. "Natural Porous Materials for Interfacial Solar Steam Generation toward Clean Water Production". In: *Solar RRL* 6.4 (2022), p. 2100986.

[186] Yusuf Shi et al. "Solar evaporator with controlled salt precipitation for zero liquid discharge desalination". In: *Environmental science & technology* 52.20 (2018), pp. 11822–11830.

[187] Yun Xia et al. "Spatially isolating salt crystallisation from water evaporation for continuous solar steam generation and salt harvesting". In: *Energy & Environmental Science* 12.6 (2019), pp. 1840–1847.

[188] Samantha A McBride, Henri-Louis Girard, and Kripa K Varanasi. "Crystal critters: Self-ejection of crystals from heated, superhydrophobic surfaces". In: *Science Advances* 7.18 (2021), eabe6960.

[189] R Sheikholeslami. "Mixed salts—scaling limits and propensity". In: *Desalination* 154.2 (2003), pp. 117–127.

[190] Liangliang Zhu et al. "Self-contained monolithic carbon sponges for solar-driven interfacial water evaporation distillation and electricity generation". In: *Advanced Energy Materials* 8.16 (2018), p. 1702149.

[191] Liangliang Zhu et al. "Shape conformal and thermal insulative organic solar absorber sponge for photothermal water evaporation and thermoelectric power generation". In: *Advanced Energy Materials* 9.22 (2019), p. 1900250.

[192] Lin Zhao et al. "A passive high-temperature high-pressure solar steam generator for medical sterilization". In: *Joule* 4.12 (2020), pp. 2733–2745.

[193] Chao Chang et al. "High-efficiency superheated steam generation for portable sterilization under ambient pressure and low solar flux". In: *ACS applied materials & interfaces* 11.20 (2019), pp. 18466–18474.

[194] Rui Gao and Dongpeng Yan. "Recent development of Ni/Fe-based micro/nanostructures toward photo/electrochemical water oxidation". In: *Advanced Energy Materials* 10.11 (2020), p. 1900954.

[195] Oara Neumann et al. "Combining solar steam processing and solar distillation for fully off-grid production of cellulosic bioethanol". In: *ACS Energy Letters* 2.1 (2017), pp. 8–13.

[196] Ajay Kumar Kaviti, Akhilesh Yadav, and Amit Shukla. "Inclined solar still designs: A review". In: *Renewable and Sustainable Energy Reviews* 54 (2016), pp. 429–451.

[197] Man Kong Yau and Roddy Rhodes Rogers. *A short course in cloud physics*. Elsevier, 1996.

[198] Aldo V Da Rosa and Juan Carlos Ordonez. *Fundamentals of renewable energy processes*. Academic Press, 2021.

[199] Salvatore P Sutera and Richard Skalak. "The history of Poiseuille's law". In: *Annual review of fluid mechanics* 25.1 (1993), pp. 1–20.

[200] PF Scholander et al. "On the ascent of sap". In: *Science* 179.4079 (1973), pp. 1248–1250.

[201] DL Saums. "ASTM D 5470-06 Thermal Interface Material Test Stand". In: *DS&A LLC* (2006).

[202] David A Didion. *An analysis and design of a linear guarded cut-bar apparatus for thermal conductivity measurements*. Tech. rep. CATHOLIC UNIV OF AMERICA WASHINGTON DC DEPT OF MECHANICAL ENGINEERING, 1968.

[203] Sean D Lubner et al. "Identification and characterization of the dominant thermal resistance in lithium-ion batteries using operando 3-omega sensors". In: *Journal of Applied Physics* 127.10 (2020), p. 105104.

[204] Vincent T Morgan. "The overall convective heat transfer from smooth circular cylinders". In: *Advances in heat transfer*. Vol. 11. Elsevier, 1975, pp. 199–264.

[205] Jiehei Zhang, Ajaykumar Gupta, and John Baker. "Effect of relative humidity on the prediction of natural convection heat transfer coefficients". In: *Heat transfer engineering* 28.4 (2007), pp. 335–342.

Appendix A

SI - Synthetic Graphene Oxide Leaf for Solar Desalination with Zero Liquid Discharge

A.1 Natural and Simulated Solar Spectra

The solar spectra were collected for natural sunlight and simulated sunlight, respectively. As shown in Figure A.1, the simulated spectrum follows the natural spectrum over the visible light region (390 to 700 nm) but deviates in the infrared range (> 700 nm). The deviation was likely caused by placing samples close to the lamp in order to achieve light intensity comparable to that of natural sunlight. The heat dissipated from the lamp is suggested by peaks in the infrared range.

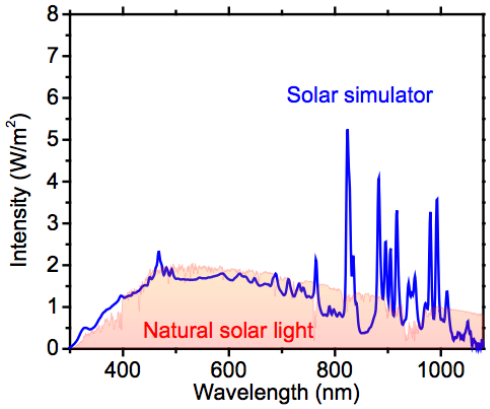

Figure A.1: Comparison of the spectra of natural and simulated sunlights.

A.2 Fabrication of Synthetic GO Leaf on Filter Paper

During the GO leaf synthesis process, the GO nanosheets were successfully crosslinked by TETA and BDGE, producing a porous structure that spanned between the cellulosic fibers of the filter paper substrate. The drastic color change from white to black on both the top and bottom sides of the GO leaf (Figure A.2) indicates that the crosslinked GO structure permeated through the entire filter paper substrate. Comparing the SEM images of the filter paper and the GO leaf, it is apparent that the GO deposition significantly changed the morphology of the filter paper by creating a much more porous surface.

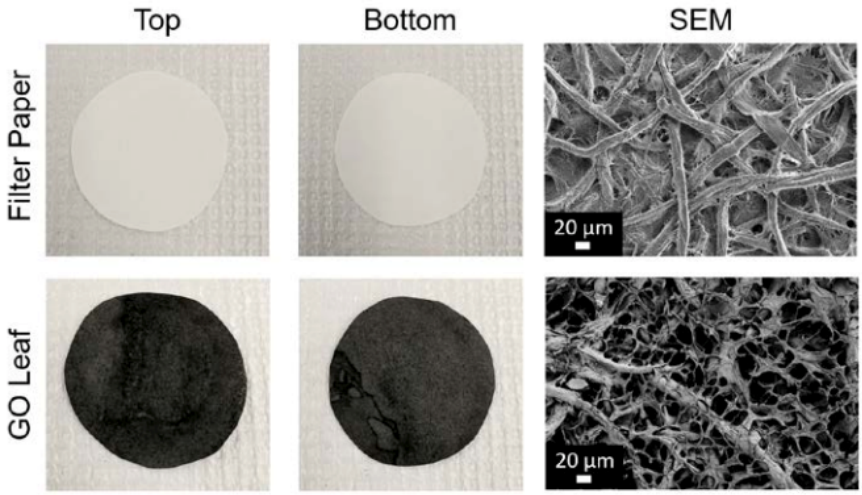

Figure A.2: Colors and morphology of the filter paper before and after GO deposition.

A.3 Durability of the GO Leaf Material

As shown in Figure A.3, the durability of the GO leaf was tested by folding the material several times and then unfolding to restore its original shape. The durability of the material is beneficial especially because the accumulated salt crystals need to be regularly scraped off from the GO leaf surface in order to reuse the material for further testing.

A.4 Stability of the GO Leaf Verified by XPS

The stability of the GO leaf was studied using X-ray photoelectron spectroscopy (XPS) before and after samples were irradiated with artificial sunlight. As shown in Figure A.4, there was no appreciable change in the elemental composition of the GO leaf after exposure to sunlight, demonstrating the material stability.

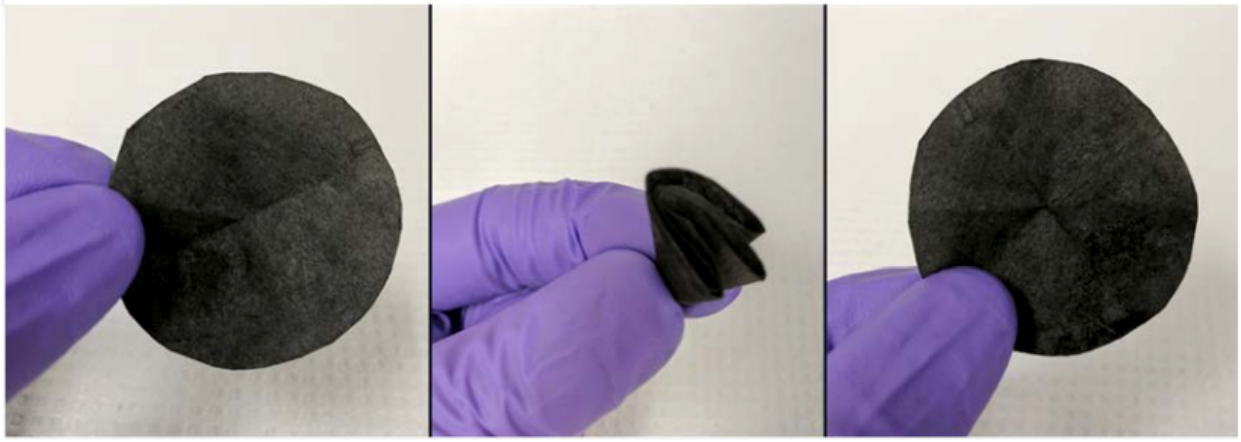

Figure A.3: Folding and unfolding of the GO leaf to demonstrate its material durability.

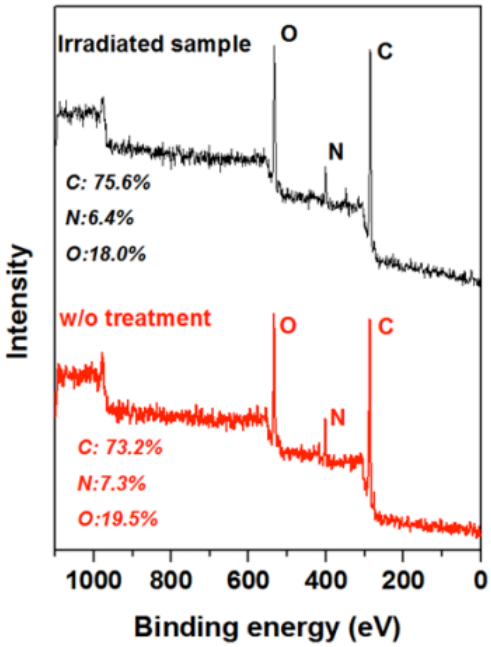

Figure A.4: XPS analysis of the GO leaf before and after sunlight irradiation.

A.5 Experimental Setup and Water Transport of the Tree Configuration

The tree configuration was designed to insulate the GO leaf from the bulk water, while simultaneously supplying the GO leaf with liquid water at a rate that did not limit the surface evaporation. To accomplish this, a water-absorbing sheet was cut into the shape of

the GO leaf and with a tail to be placed in contact with liquid water in the reservoir. As shown in Figure A.5, the GO leaf was placed on top of the water-absorbing sheet, and the tail extended into the liquid water to ensure rapid water transport from the bulk reservoir to the GO leaf via capillary action. It was observed that an initially dry GO leaf was fully saturated with water within two minutes after initiating the water transport.

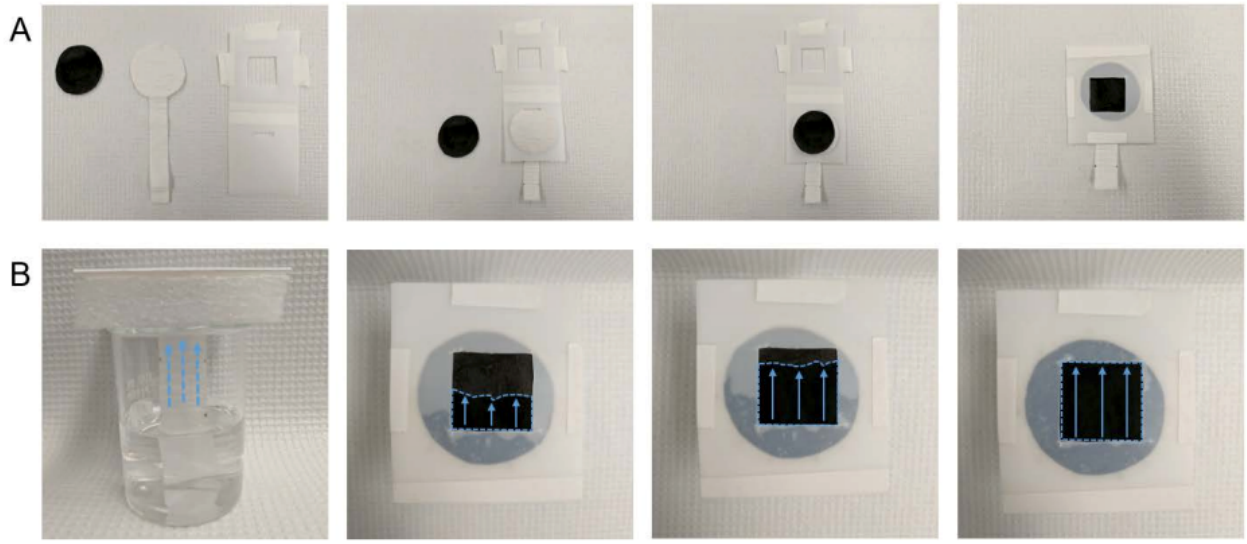

Figure A.5: Step-by-step assembly of the experimental setup of the tree configuration with a GO leaf. (A) Establishing the contact between the GO leaf and the water transporter (i.e., a water-absorbing sheet with a tail); and (B) water transport from the bulk reservoir to the GO leaf.

A.6 Calculation of Evaporation Efficiency

The evaporation efficiency can be calculated as $\dot{m}h_{LV}/I$, where $\dot{m}$ is the mass rate of Evaporation, h_{LV} is the total enthalpy of the sensible heat and phase change of water, and I is the light intensity of the incident light from the solar simulator.[14]

Mass Rate of Evaporation ($\dot{m}$):

The mass rate of evaporation is the rate at which water mass is evaporated, normalized by the evaporation area. To account for evaporation that occurs in the absence of light, the mass rate of evaporation should be determined as the difference between those in light and dark conditions:

$$\dot{m} = \dot{m}_{light} - \dot{m}_{dark} \tag{A.1}$$

Data for the normalized rates of evaporation in dark conditions were collected before samples were exposed to simulated sunlight. As shown in Figure A.6, the GO leaf did not enhance the evaporation rate in the absence of light.

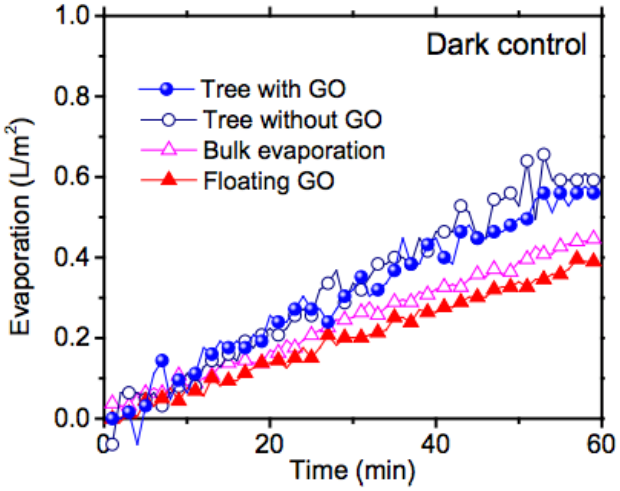

Figure A.6: Evaporation performance of the GO leaf and controls under dark conditions.

Total Enthalpy (h_{LV}):

The total enthalpy has two components: (1) the heat of changing the temperature of the water being evaporated and (2) the heat of vaporization:

$$h_{LV} = c(T_{surface} - T_{bulk}) + L \tag{A.2}$$

Where c is the specific heat capacity,$T_{surface}$ is the temperature at the evaporation interface, T_{bulk} is the temperature of the bulk water reservoir, and L is the specific latent heat of phase change. The specific heat capacity for temperature change is 4.18 $\frac{J}{g}$ and the specific latent heat of phase change is determined empirically by the following relationship:[197]

$$L = -0.00006T_{surface}^3 + 0.0016T_{surface}^2 - 2.36T_{surface} + 2500.8 \tag{A.3}$$

Light Intensity (I):

The light intensity is the intensity of light that is exposed to the material's surface. For the tree configuration, this intensity was corrected by accounting for the transmissivity of the polystyrene plastic that covered a portion of the GO leaf. By measuring the absorption spectrum of such polystyrene plastic, the GO leaf still absorbed 26.8% of the irradiating light. To account for this factor, the intensity was corrected by the following equation:

$$I = I_0(\frac{A_{exposed} + A_{covered} f_{transmitted}}{A_{exposed}}) \tag{A.4}$$

Where I is the corrected light intensity, I_0 is the initial light intensity, $A_{exposed}$ is the area of the GO leaf that was exposed directly to light, $A_{covered}$ is the area of the GO leaf that was covered by the polystyrene plastic, and $f_{transmitted}$ is the percentage of light that is transmitted through the polystyrene plastic ($\sim$26.8%).

A.7 Fate of Solar Energy on the Evaporation Surface

The fate of solar energy was determined by calculating the percent of energy input distributed to evaporation ($E_{evaporation}$), loss due to light reflection/transmission ($E_{loss\ as\ light}$), and heat loss to the environment ($E_{loss\ as\ heat}$).

Energy Used for Evaporation ($E_{evaporation}$):

The energy distributed to evaporation was calculated by multiplying the normalized mass rate of evaporation ($\dot{m}$) by the total enthalpy (h_{LV}):

$$E_{evaporation} = \dot{m} h_{LV} \tag{A.5}$$

The percent of energy distributed to evaporation was calculated by dividing $E_{evaporation}$ by the light intensity exposed to the evaporation surface (I).

Energy Loss due to Light Reflection/Transmission ($E_{loss\ as\ light}$):

The energy distributed to reflection/transmission was calculated by subtracting the total light intensity (I) by the amount of light that was absorbed by the evaporation surface. The amount of light absorbed by the evaporation surface was determined by multiplying the percent of light absorbed (A_λ) by the light intensity exposed to the evaporation surface (I_λ) for all wavelengths.

$$E_{loss\ as\ light} = (I - \sum_{\lambda=350}^{1080} A_\lambda I_\lambda) \tag{A.6}$$

The percent of energy distributed to light reflection/transmission was calculated by dividing $E_{loss\ as\ light}$ by the light intensity exposed to the evaporation surface (I).

Heat Loss to the Environment ($E_{loss\ as\ heat}$):

The amount of incoming solar energy that is not consumed by evaporation or lost by light reflection/transmission is assumed to be in the form of heat energy being captured by the

evaporation system. Since the experimental system was believed to have reached steady state with a stabilized temperature, the heat absorption should be balanced by the heat loss to the environment. Therefore, the heat loss to the environment can be calculated as:

$$E_{loss\ as\ heat} = I - (E_{evaporation} + E_{loss\ as\ light}) \tag{A.7}$$

The percent of heat loss to the environment was calculated by dividing $E_{loss\ as\ heat}$ by the light intensity exposed to the evaporation surface (I).

A.8 Crystal Formation on the GO leaf surface

Salt crystal formation became more severe as the solution salinity increased, reducing the evaporation rate. However, open pores were still observed at each tested salinity level.

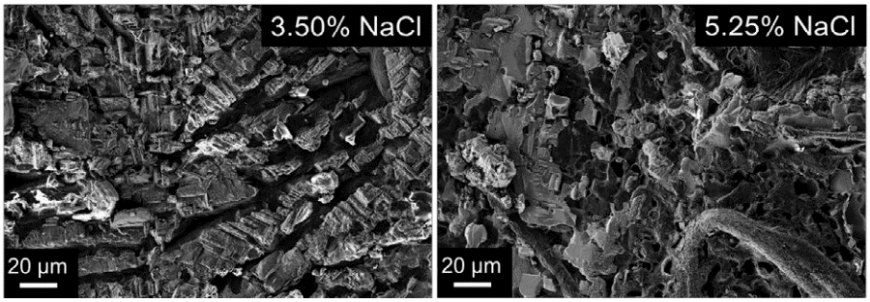

Figure A.7: SEM images of early-stage formation of salt crystals on the GO leaf surface (regions free of crystal to the naked eyes when crystals started forming in other regions) using 3.5 and 5.25 wt.% NaCl solutions, respectively.

A.9 Reusability of the GO Leaf

In order to maintain the soundness of the overall system after severe salt build-up took place on the GO leaf surface, the salt crystals were physically scraped off and the GO leaf was soaked in deionized water for about 5 minutes (Figure A.8-A). The evaporation performance of the GO leaf was monitored over the course of 5 cycles of solar evaporation followed by such scraping/soaking. As seen in Figure A.8-B, there was no apparent deterioration in evaporation performance among these cycles, demonstrating the reusability of the GO leaf with the facile cleaning approach.

Video. Time-lapse video documenting five-day salt accumulation on the surface of a GO leaf in the tree configuration tested at a high salinity of 15 wt.% NaCl.

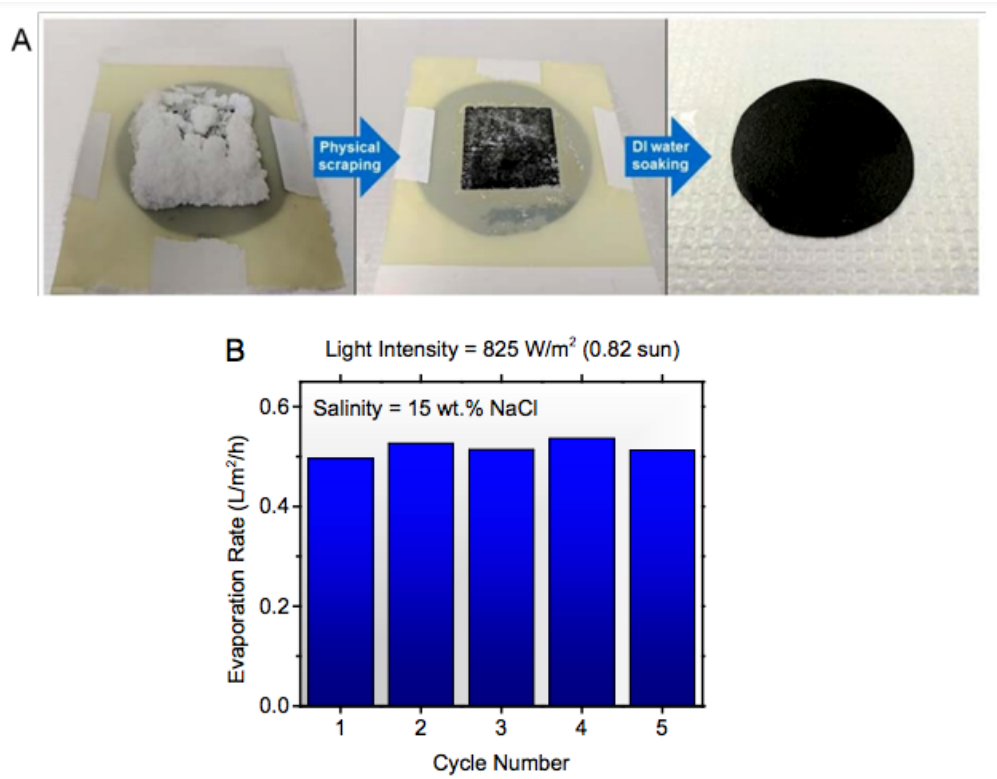

Figure A.8: Reusability of the GO leaf after physical cleaning. (A) Facile procedure for cleaning the GO leaf with severe salt build-up, and (B) steady evaporation performance after multiple cycles of scaling and cleaning.

Appendix B

SI - Interfacial Solar Evaporation by a 3D Graphene Oxide Stalk for Highly Concentrated Brine Treatment

B.1 Supplementary Note 1 – Analysis of Light Intensity and Evaporative Water Flux for Different 3D Geometries

To determine the best 3D geometry to pursue, we selected three different 3D geometries (domes, cones, and cylinders) that are most promising to generate high EAI. Using MATLAB, the 3D geometries were constructed by rendering the 3D surfaces into 2D subunits, each with a specific direction and inclination angle (Figure B.1-A). Introducing a solar model described by Da Rosa,[198] the light intensity being irradiated onto each 2D subunit (Figure B.1-B) could be calculated by the following expression:

$$I_D = [Aexp(\frac{-B}{sin(90-\chi)})][cos(\chi)cos(\epsilon) + sin(\epsilon)sin(\chi)cos(\xi-\zeta)] \tag{B.1}$$

where

- A and B are solar constants, 1310 W/m^2 and 0.18 respectively;
- χ is the solar zenith angle;
- ξ is the solar azimuth angle;
- ϵ is the tilt or inclination angle of the 2D subunit; and
- ζ is the surface azimuth angle or the direction of the 2D subunit.

To make the model representative of the testing conditions used in laboratory experiments, it was initially assumed that the light source is fixed at solar noon (χ=0°) and the 3D geometry is being irradiated at the equator (ξ=180°). These simplifications allow for the light intensity being irradiated onto each 2D subunit, based on their specific directions (ζ) and inclination angles (ϵ). Using empirical data collected on the evaporative flux of the 2D GO evaporator as a function of light intensity (Figure B.1-C), the evaporative flux of each 2D subunit was estimated. By summing up the evaporation contributions of each 2D subunit, the total evaporative flux of the 3D geometry is determined. This procedure was repeated for each 3D geometry as a function of height from 5 to 20 cm. Additionally, the models were also run for a solar zenith angle (χ) of 45º.

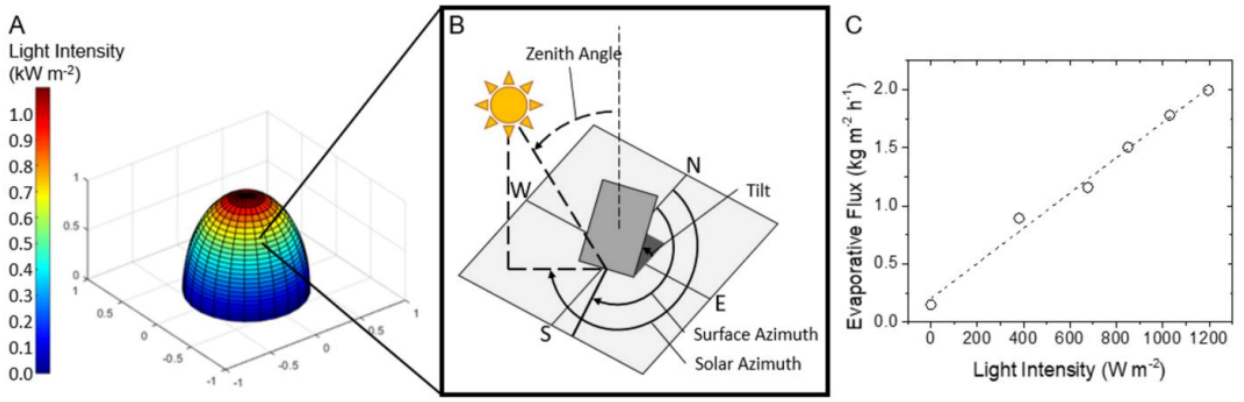

Figure B.1: Modeling the evaporative performance of various 3D geometries. A) Rendering of 3D geometry into 2D subunits. B) Determination of light intensity irradiating onto each 2D subunit. C) Correlation of light intensity to evaporative flux for each 2D subunit.

B.2 Supplementary Note 2 – Determination of Water Lifting Limit

To understand the limitations in the rate at which water can be supplied to the evaporation interfaces on a 3D evaporator by capillary action, a simplified model for passive water lifting was developed. Assuming water transport through the 3D evaporator can be modeled as flow through a cylindrical conduit, the Hagen-Poiseuille equation[199] was used to determine the maximum evaporation rate that can be supported as a function of height:

$$J_{evap,max} = \frac{Q_{HP}}{A_{conduit}} = \frac{\frac{\pi d^4 \Delta P}{128 \mu h}}{\frac{\pi}{4} d^2} = \frac{d^2 \Delta P}{32 \mu h}] \tag{B.2}$$

where

- d is the diameter of the cylindrical conduit, which is estimated to be the average internal pore diameter of ($\sim$100 μm);
- ΔP is the pressure difference across the cylindrical conduit;
- μ is the dynamic viscosity of water (0.89 kPa s at 25°C); and
- h is the height to which water has been lifted.

Drawing parallels to Cohesion-Tension theory,[200] the pressure differential (ΔP) is determined by balancing capillary force and gravitational force acting on the water flowing through the cylindrical conduit:

$$\Delta P = \frac{\pi d\sigma cos(\theta) - \frac{\pi}{4}d^2 h\rho g}{\frac{\pi}{4}d^2} = \frac{4\sigma cos(\theta)}{d} - h\rho g \tag{B.3}$$

where

- σ is the surface tension between water and air (0.072 $N\ m^{-1}$ at 25°C);
- θ is the contact angle formed by the water at the top of the cylindrical conduit, set to be 0° to determine the maximum evaporative flux that can be supported;
- ρ is the density of water (997.05 $kg\ m^{-3}$ at 25°C); and
- g is the gravitational constant (9.81 $m\ s^{-2}$).

Substituting Equation S3 into Equation S2, we can determine an expression for the maximum evaporative flux that can be supported by passive water replenishment as a function of height:

$$J_{evap,max} = \frac{d^2}{32\mu h}(\frac{4\sigma cos(\theta)}{d} - h\rho g) \tag{B.4}$$

B.3 Supplementary Note 3 – Thermal Conductivity Measurements by Cut-Bar Method

The cross-plane thermal conductivity of the 2D and 3D evaporators was measured directly using the linear heat flow Cut Bar method, which is a technique adapted from the ASTM-5470 standard.[201, 202] Figure B.2 shows a photo of the measurement setup comprising two 1×1 $in.^2$ copper reference bars, with eight fine-tip thermocouples that measure the temperature profiles along the bars. The sample with unknown thermal conductivity is sandwiched between the two copper bars such that heat flows through it in 1D. A resistance heater generates a heat flux which flows from the top bar through the sample into the bottom bar, after which it is dissipated by a large metal base. Fiberglass insulation is

wrapped around the entire setup to minimize heat losses to the environment. A pressure of ∼15 psi was applied at the top bar to reduce thermal contact resistance as thermal grease was avoided due to the porosity of the samples to be measured. All leaf and stick samples were sized to match the cross-sectional area of the reference bars, and the sample thickness was measured using a caliper. For wet measurements, the samples were soaked in water for at least one hour, and a layer of Kapton tape was then placed around the outer surface of the bars encompassing the sample to minimize evaporation during the experiment. Each measurement was performed for 10 hours to ensure that steady state conditions are attained. The temperature profile in each bar was recorded, from which the heat flux, q was calculated using the thermal conductivity of copper. The temperature gradient in each bar was also used to extrapolate to the bar surface and calculate the total temperature drop, ΔT across the sample. Using these values and the sample thickness, the cross-plane thermal conductivity can be extracted.[203] Similar measurements were also performed using samples of filter paper and the cotton stick sized to the same dimensions as the GO-containing samples in order to provide the thermal conductivity of the base material.

Table B.1: Thermal conductivity data collected by the Cut-Bar Method

Sample	**Condition**	**Thickness**	**Thermal Conductivity**
Filter Paper Substrate (Stack, 4-Layers)	Dry	0.65 mm	0.050 $W\ m^{-1}\ K^{-1}$
	Wet	0.65 mm	0.084 $W\ m^{-1}\ K^{-1}$
2D evaporator (Single, 1-Layer)	Dry	0.24 mm	0.068 $W\ m^{-1}\ K^{-1}$
	Wet	0.24 mm	0.120 $W\ m^{-1}\ K^{-1}$
2D evaporator (Stack, 4-Layers)	Dry	0.82 mm	0.072 $W\ m^{-1}\ K^{-1}$
	Wet	0.82 mm	0.140 $W\ m^{-1}\ K^{-1}$
Cotton Stick Substrate	Dry	25.0 mm	0.080 $W\ m^{-1}\ K^{-1}$
	Wet	25.0 mm	0.116 $W\ m^{-1}\ K^{-1}$
3D evaporator	Dry	26.8 mm	0.120 $W\ m^{-1}\ K^{-1}$
	Wet	26.8 mm	0.165 $W\ m^{-1}\ K^{-1}$

B.4 Supplementary Note 4 – Analysis of Convective Heat Transfer Coefficient for Ambient Heating

Ambient heating (also called environmental energy)[59] introduces an additional energy source that further increases the maximum evaporative flux that can be achieved by interfacial vapor generation systems. The primary mode of heat transfer for ambient heating

Figure B.2: Image of cut-bar experimental setup used to determine the thermal conductivities of the samples described above.

is through convection and can be quantified by the following expression:

$$q_{ambient} = h_{conv} A_{side} (T_a - T_s) \tag{B.5}$$

where

- h_{conv} is the convective heat transfer coefficient through air;
- A_{side} is the area of the side of the 3D evaporator, excluding the top area;
- T_a is the temperature of the surrounding environment; and
- T_s is the sub-ambient temperature of the side surface of the 3D evaporator.

Of the variables listed above, the convective heat transfer coefficient (h_{conv}) is the only one that cannot be directly measured. To determine this value, we used an empirical relationship developed for convective heat transfer from an isothermal, vertically-oriented cylinders[204] with the height to diameter ratio ranges between 8 and 127:

$$h_{conv} = \frac{Nu_L k}{L} \tag{B.6}$$

where

- L is the characteristic length or height of the 3D evaporator;
- k is the thermal conductivity of air ($k_{air}(30°C) = 26.62 \times 10^{-3}\ W/(mK)$); and
- Nu_L can be calculated by:

$$Nu_L = 1.07(Gr_L Pr)^{0.28} \tag{B.7}$$

and

$$Gr_L = \frac{g(T_a - T_s)L^3}{T_a \nu^2} \tag{B.8}$$

where

- Pr is the Prandtl Number for air ($P_r(30°C) = 0.7066$);
- g is the acceleration due to gravity ($g = 9.81\ m/s^2$); and
- ν is the kinematic viscosity of air ($\nu(30°C) = 18.610^{-6}\ m^2/s$).

Using the above relationship, the convective heat transfer coefficient was determined for three separate experiments where the evaporative flux was determined for 3D evaporators with varying heights: 1.0 cm, 7.5 cm, and 13.0 cm. The results have been tabulated in Table B.2:

Table B.2: Determination of convective heat transfer coefficient by empirical correlations.

Height	**L/D**	T_a	T_s	$\|Gr\|$	Nu_L	h_{conv}
10 mm	1.33*	27.8°C	32.0°C	$4.28x10^3$	4.97	$13.23\frac{W}{m^2\ °C}$
75 mm	10.00	27.7°C	22.0°C	$2.46x10^6$	59.8	$21.22\frac{W}{m^2\ °C}$
130 mm	17.33	28.5°C	20.6°C	$1.73x10^7$	103.2	$21.13\frac{W}{m^2\ °C}$

∗A different correlation[204] was used for the 10-mm 3D evaporator due to its low L/D ratio.

These calculated values for convective heat transfer coefficients were compared to those determined by an energy balance under dark conditions (0 W m-2 of incident sunlight). Under these conditions, it is assumed that the energy for evaporation is solely derived from convective heat transfer as seen in the following expression:

$$J^D_{evaporation} h_{lv} A_{total} = h^D_{conv} A_{total} (T^D_a - T^D_s) \tag{B.9}$$

where

- $J^D_{evaporation}$ is the evaporative flux under dark conditions;
- h_{lv} is the enthalpy of vaporization at $T_s (h_{lv}(20°C) = 2454.6\ kJ\ kg^{-1})$;
- h^D_{conv} is the convective heat transfer coefficient determined under dark conditions;
- T_a is the temperature of the surrounding environment under dark conditions; and
- T_s is the temperature of the surface of the 3D evaporator under dark conditions.

Rearranging this expression, we can solve for the convective heat transfer coefficient (h^D_{conv}) and the results have been tabulated in Table B.3:

$$h^D_{conv} = \frac{J^D_{evaporation} h_{lv}}{T^D_a - T^D_s} \tag{B.10}$$

Table B.3: Determination of convective heat transfer coefficient by dark-condition experiments.

Height	$J^D_{evaporation}$	T^D_a	T^D_s	h^D_{conv}
10 mm	$1.396 \times 10^{-4}\ \frac{kg}{m^2\ s}$	$27.5°C$	$20.8°C$	$9.58 \frac{W}{m^2\ °C}$
75 mm	$3.848 \times 10^{-3}\ \frac{kg}{m^2\ s}$	$27.5°C$	$18.1°C$	$25.17 \frac{W}{m^2\ °C}$
130 mm	$7.973 \times 10^{-3}\ \frac{kg}{m^2\ s}$	$27.5°C$	$17.0°C$	$29.18 \frac{W}{m^2\ °C}$

When comparing the convective heat transfer coefficients determined from the two methods described above, we can see that the results are similar. We believe that discrepancies may arise from differences in experimental setups under which our experiments were run and under which the empirical correlations were established. Unlike the empirical studies, which studied isothermal cylinders with no mass exchange between the cylinders and the environment, our 3D cylinders evaporate water to the ambient environment. This likely has two effects: (1) the mass transfer of water transitioning from a liquid to a vapor at the evaporative interface disturbs the boundary layer that serves as the rate limiting step for heat transfer and (2) the presence of water vapor has been shown to increase convective heat transfer.[205] This would explain why the experimentally determined convective heat transfer coefficients were typically higher than those estimated by empirical correlations, as seen for the 75-mm and 130-mm 3D evaporators. As a result, we used these experimentally determined convective heat transfer coefficients for our calculation of energy input.

The estimation for the 10-mm 3D evaporator using an empirical correlation was less successful because of its low L/D ratio. Additionally—as will be described in Supplementary Note 5—the energy from reflected diffuse light is heating the sides of the 10-mm 3D cylinder to a temperature above the temperature of the ambient environment. As a result, the difference in the surface temperatures is believed to cause the difference in the calculated convective heat transfer coefficients.

B.5 Supplementary Note 5 – Analysis of Solar Energy from Direct Solar and Diffuse Light

The solar energy input can be attributed to either direct solar radiation or diffuse light. The direct solar energy flux from incident solar radiation was determined by the following:

$$q_{solar} = I_0 \times A_{top} \tag{B.11}$$

where

- I_0 is the incident solar intensity (1000 $W\ m^{-2}$); and
- A_{top} is the area of the top (or projected area) of the 3D evaporator.

The diffusive radiation flux from diffuse light was determined by summing the contributions of light being reflected from segments of the extruded polystyrene (EPS) base onto segments of the side of the 3D evaporator (Figure B.3):

$$q_{diffuse} = n_k \sum_{i=1}^{n_i} \sum_{j=1}^{n_j} \frac{I_i \alpha_{EPS} \times A_i}{A_i} \left(\frac{A_i cos(\phi_i) A_j cos(\phi_j)}{\pi R_{ij}^2}\right) \tag{B.12}$$

where

- I_i is the incident light intensity at the level of the EPS base;
- α_{EPS} is the albedo of the EPS base (0.85);
- A_i is the area of base segment;
- A_j is the area of 3D evaporator segment projected onto the vertical plane facing perpendicularly to the direction of A_i;
- R_{ij} is the distance between the center point of A_i to the center point of A_j;
- ϕ_i is the angle between the surface normal of A_i and the ray formed by R_{ij};
- ϕ_j is the angle between the surface normal of A_j and the ray formed by R_{ij};
- n_i is the number of base segments going out radially from the 3D evaporator;
- n_j is the number of 3D evaporator segments going out vertically from the base; and
- n_k is the number of slices that comprise the EPS base.

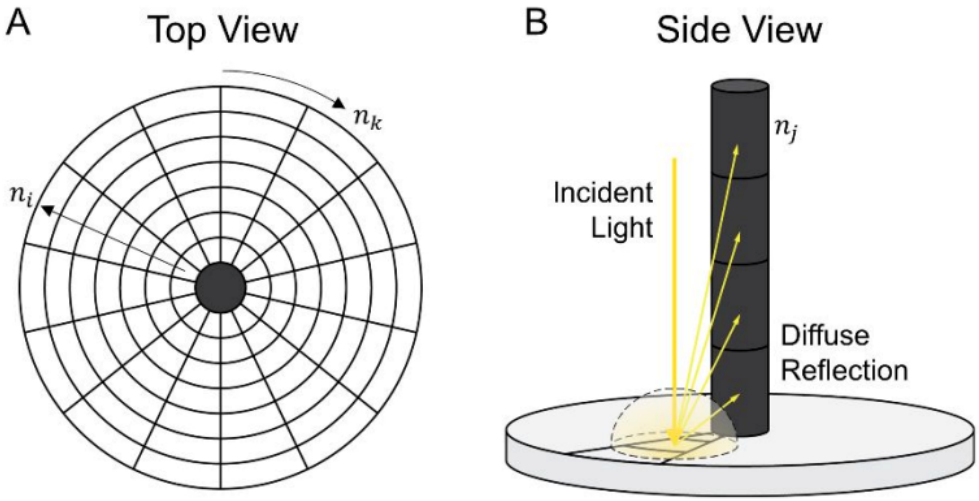

Figure B.3: Incorporation of diffuse light to calculate solar-vapor conversion efficiency. (A) Top view of the 3D evaporator setup, showing how the extruded polystyrene base was segmented for the reflected diffuse light analysis. (B) Side view of the 3D evaporator setup, showing how the 3D cylinder was segmented for the reflected diffuse light analysis.

B.6 Supplementary Note 6 – Outdoor Comparison of 2D and 3D Evaporator Performance

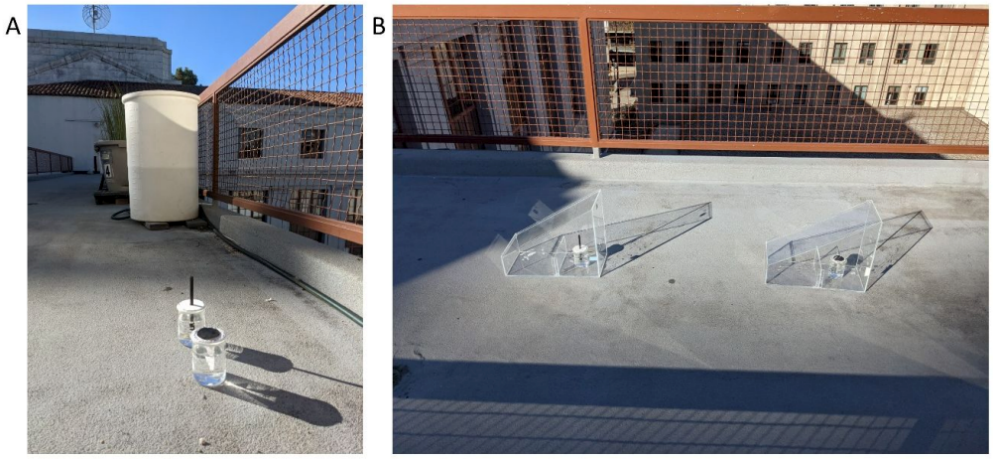

Figure B.4: Outdoor experiments to demonstrate the advantages of omni-directional light utilization of the 3D GO stalk over the 2D evaporator. (A) Experiment conducted under open-air conditions. (B) Experiments conducted under closed conditions.

To demonstrate the benefits of omni-directional light utilization of the 3D GO stalk, the evaporative performance was evaluated using actual sunlight. Experiments were conducted

in Berkeley, CA (latitude: 37.87° N) from 9:00 am to 5:00 pm on clear days (minimal smoke or cloud cover). The open-air experiment was run on September 30, 2021, where the peak temperature reached 27.8°C. The closed experiment was run on October 1, 2021, where the peak temperature reached 28.9°C. For both sets of experiments, the mass of the 3D GO stalk and 2D GO evaporator setups were measured at 9:00am and 5:00pm. The mass change (in kg) was divided by both the duration (in hours) of the experiment and the projected ground area of the evaporator (in m^2) to obtain an day-averaged evaporative flux. These values have been tabulated in Table B.4.

Table B.4: Day-averaged evaporative flux from 9:00 am to 5:00pm in Berkeley, CA.

Condition	**Date [MM-DD-YY]**	**2D Evaporative Flux** $[kg\ m^{-2}\ h^{-1}]$	**3D Evaporative Flux** $[kg\ m^{-2}\ h^{-1}]$
Open	09-30-21	1.01	39.98
Closed	12-01-21	0.74	18.84

B.7 Supplementary Note 7 – Compilation of 3D Evaporator Performance Data

The data presented in Figure 5.B of the main manuscript was manually compiled by consulting all interfacial solar vapor generation papers that proposed a geometry with an evaporation area index (EAI) that was greater than 1. This data only includes the evaporative performance of 3D evaporators under 1-sun conditions (1000 $W\ m^{-2}$), without dark conditions having been subtracted out. Additionally, values for EAI—unless stated outright—were estimated based on available information about the 3D evaporator configuration. The data compiled in Table B.5 includes all references that were found and published by June 2020.

Table B.5: Tabulated data of 3D evaporator performance under 1-sun conditions.

Source	**EAI**	**Light** $[kg\ m^{-2}\ h^{-1}]$	**Shape**	**Year**
Xu et al., 2017, Advanced Materials [34]	1.73	1.25	Bio-Inspired	2017
	1.73	1.67	Bio-Inspired	2017
Xiao et al., 2019, Solar RRL [112]	0.62	0.65	Bio-Inspired	2019
	1.23	1.08	Bio-Inspired	2019
	1.84	1.68	Bio-Inspired	2019
	2.44	1.96	Bio-Inspired	2019
	3.05	2.18	Bio-Inspired	2019
	3.66	2.38	Bio-Inspired	2019
Bian et al., 2019, Global Challenges [111]	5.17	3.15	Bio-Inspired	2019
Sun et al., 2020, ACS Applied Materials & Interfaces [118]	2	1.51	Bio-Inspired	2020
Sui et al., 2020, Journal of Material Science [119]	1.36	2.01	Bio-Inspired	2020
	8.32	2.32	Bio-Inspired	2020
Gao et al., 2018, Global Challenges [120]	1.44	1.07	Bio-Inspired	2018
	1.44	1.11	Bio-Inspired	2018
	1.44	1.15	Bio-Inspired	2018
	1.44	1.24	Bio-Inspired	2018
	1.44	1.32	Bio-Inspired	2018
	1.44	1.38	Bio-Inspired	2018
Chen et al., 2020, ACS Applied Materials & Interfaces [121]	1.60	1.74	Bio-Inspired	2020
Wang et al. 2020, Advanced Functional Materials [122]	2.00	1.8	Bio-Inspired	2020
	2.78	1.71	Bio-Inspired	2020
	3.87	1.75	Bio-Inspired	2020
	5.02	1.78	Bio-Inspired	2020
	6.18	1.81	Bio-Inspired	2020
	7.33	1.83	Bio-Inspired	2020
	2.00	2.13	Bio-Inspired	2020
	2.47	2.14	Bio-Inspired	2020
	3.05	2.17	Bio-Inspired	2020
	3.62	2.21	Bio-Inspired	2020
	4.19	2.28	Bio-Inspired	2020
	4.89	2.30	Bio-Inspired	2020
Liu et al., 2020, Advanced Sustainable Systems [123]	1.03	1.65	Bio-Inspired	2020
Chen et al., 2020, Nano Energy [124]	3.50	2.08	Bio-Inspired	2020

Source	**EAI**	**Light** $[kg\ m^{-2}\ h^{-1}]$	**Shape**	**Year**
Wang et al. 2020, Advanced Functional Materials [122]	2.00	1.8	Bio-Inspired	2020
	2.78	1.71	Bio-Inspired	2020
	3.87	1.75	Bio-Inspired	2020
	5.02	1.78	Bio-Inspired	2020
	6.18	1.81	Bio-Inspired	2020
	7.33	1.83	Bio-Inspired	2020
	2.00	2.13	Bio-Inspired	2020
	2.47	2.14	Bio-Inspired	2020
	3.05	2.17	Bio-Inspired	2020
	3.62	2.21	Bio-Inspired	2020
	4.19	2.28	Bio-Inspired	2020
	4.89	2.30	Bio-Inspired	2020
Liu et al., 2020, Advanced Sustainable Systems [123]	1.03	1.65	Bio-Inspired	2020
Chen et al., 2020, Nano Energy [124]	3.50	2.08	Bio-Inspired	2020
Zhang et al. 2020, Applied Energy [125]	2.26	1.69	Bio-Inspired	2020
	2.64	1.80	Bio-Inspired	2020
	3.39	1.95	Bio-Inspired	2020
Geng et al., 2020, Advanced Functional Materials [126]	2.72	1.72	Bio-Inspired	2020
	3.06	1.76	Bio-Inspired	2020
	3.41	1.83	Bio-Inspired	2020
	3.75	1.86	Bio-Inspired	2020
	4.47	1.95	Bio-Inspired	2020
Xie et al., 2021, ACS Applied Materials and Interfaces [127]	10.60	3.72	Bio-Inspired	2021
Sun et al., 2021, Carbon [128]	21.00	4.16	Bio-Inspired	2021
Zhang et al., 2021, Solar Energy Materials and Solar Cells [129]	11.00	2.86	Bio-Inspired	2021
	21.00	4.11	Bio-Inspired	2021
Li et al., 2017, National Science Review [79]	2.8	1.72	Cone	2017
Yang et al., 2019, Global Challenges [130]	5.15	1.56	Cone	2019
Wu et al., 2020, Nature Communications [134]	1.16	1.86	Cone	2020
	1.72	2.28	Cone	2020
	2.97	2.55	Cone	2020
	4.12	2.64	Cone	2020
Tu et al., 2019, Small [116]	43.92	19.07	Cuboid	2019
Zhang et al., 2019, Advanced Sustainable Systems [135]	1.48	0.90	Cuboid	2019
	4.68	1.00	Cuboid	2019
	11.88	0.97	Cuboid	2019
Guo et al., 2020, Renewable Energy [136]	3	1.34	Cuboid	2020
	5	1.46	Cuboid	2020
	7	1.54	Cuboid	2020
	9	1.6	Cuboid	2020
	11	1.63	Cuboid	2020
Shao et al., 2020, Journal of Materials Chemistry A [137]	4	1.98	Cuboid	2020
Zhang et al. 2020, Nano Energy [138]	4	2.30	Cuboid	2020
Shi et al., 2018, Joule [114]	2.70	1.37	Cup	2018
	4.40	1.43	Cup	2018
	6.11	1.51	Cup	2018
	7.81	1.66	Cup	2018
	9.51	1.737	Cup	2018
	18.02	1.84	Cup	2018
	23.13	2.04	Cup	2018
Bian et al., 2019, Advanced Materials Technologies [139]	26.18	3.13	Cup	2019

Source	**EAI**	**Light** $[kg\ m^{-2}\ h^{-1}]$	**Shape**	**Year**
Li et al., 2019, Advanced Sustainable Systems [140]	1.4	1.35	Curved	2019
	1.4	1.46	Curved	2019
Liu et al., 2019, Advanced Functional Materials [108]	1.25	1.34	Curved	2019
Wu et al., 2018, Journal of Materials Chemistry A [141]	2.60	1.54	Cylinder	2018
Wu et al., 2019, Science Bulletin [142]	4.85	2.55	Cylinder	2019
	8.69	3.4	Cylinder	2019
	12.54	4.01	Cylinder	2019
Storer et al., 2020, ACS Applied Materials & Interfaces [143]	2.33	1.3	Cylinder	2020
	3.67	1.85	Cylinder	2020
	5	2.25	Cylinder	2020
Li et al., 2020, Joule [117]	7	2.63	Cylinder	2020
	7	2.8	Cylinder	2020
	7	2.63	Cylinder	2020
	7	2.57	Cylinder	2020
Tang et al., 2020, ACS Applied Materials & Interfaces [103]	6	2.50	Cylinder	2020
	8.5	3.06	Cylinder	2020
	11	3.72	Cylinder	2020
	13.5	4.53	Cylinder	2020
	16	4.52	Cylinder	2020
	18.5	4.14	Cylinder	2020
Wang et al., 2020, ACS Applied Materials & Interfaces [144]	3.82	2.27	Cylinder	2020
Wang et al. 2020, Environmental Science & Technology [145]	12.76	1.79	Cylinder	2020
	24.52	1.83	Cylinder	2020
	36.29	1.93	Cylinder	2020
	11.52	1.65	Cylinder	2020
	10.52	1.61	Cylinder	2020
Li et al., 2020, Journal of Materials Chemistry A [27]	2.2	1.82	Cylinder	2020
Gao et al., 2020, Tungsten [146]	4.08	2.85	Cylinder	2020
	5.62	3.37	Cylinder	2020
	7.15	3.71	Cylinder	2020
Gao et al., 2021, Solar RRL [147]	8.20	4.70	Cylinder	2021
	15.40	6.10	Cylinder	2021
	23.40	7.60	Cylinder	2021
Hong et al., 2018, ACS Applied Materials & Interfaces [38]	1.02	0.96	Folded	2018
	1.87	1.19	Folded	2018
	1.92	1.14	Folded	2018
	2.06	1.08	Folded	2018
	2.23	1.20	Folded	2018
	2.37	1.19	Folded	2018
	2.46	1.26	Folded	2018
	3.21	1.42	Folded	2018
	3.55	1.35	Folded	2018
	4.16	1.42	Folded	2018
	4.32	1.45	Folded	2018
	4.62	1.51	Folded	2018
	4.63	1.60	Folded	2018
	5.41	1.53	Folded	2018
	5.62	1.51	Folded	2018
	7.20	1.58	Folded	2018
Xu et al., 2019, Chemical Engineering Journal [132]	1.41	1.16	Folded	2019
Song et al., 2018, Advanced Science [58]	7.94	1.58	Folded	2018
	13.11	2.2	Folded	2018
Li et al., 2019, Advanced Materials [133]	4.24	1.63	Folded	2019
	5.52	1.68	Folded	2019
	3.65	1.56	Folded	2019
	10.35	2.12	Folded	2019
Ni et al., 2019, ACS Applied Materials & Interfaces [110]	2.76	2.99	Folded	2019
	2.5	2.01	Folded	2019

Source	**EAI**	**Light** $[kg\ m^{-2}\ h^{-1}]$	**Shape**	**Year**
Wang et al., 2018, Journal of Materials Chemistry A [109]	1.07	0.99	Inverted Cone	2018
	1.35	1.15	Inverted Cone	2018
	1.74	1.23	Inverted Cone	2018
	2.50	1.29	Inverted Cone	2018
	2.33	1.28	Inverted Cone	2018
	2.80	1.42	Inverted Cone	2018
	3.29	1.56	Inverted Cone	2018
	3.45	1.71	Inverted Cone	2018
	1.74	1.37	Inverted Cone	2018
Bai et al., 2019, Applied Thermal Engineering [148]	1.15	1.14	Inverted Cone	2019
	1.24	1.18	Inverted Cone	2019
	1.41	1.21	Inverted Cone	2019
Ni et al., 2019, ACS Applied Materials & Interfaces [110]	3	2.14	Inverted Cone	2019
Cao et al., 2020, Chemical Engineering Journal [149]	3.86	1.78	Inverted Cone	2020
	2.61	1.50	Inverted Cone	2020
	2	1.38	Inverted Cone	2020
	1.64	1.31	Inverted Cone	2020
Yang et al., 2019, ACS Applied Energy Materials [115]	1.42	1.31	Pyramid	2019
Xu et al., 2020, ChemSusChem [150]	20.00	3.19	Pyramid	2020
Yuan et al., 2020, Advanced Sustainable Systems [151]	2.00	1.56	(Hemi)Sphere	2020
	4.00	2.00	Sphere	2020
Lu et al., 2020, Solar RRL [113]	4.00	3.09	Sphere	2020
Zhang et al., 2018, Journal of Materials Chemistry A [107]	11.05	2	Other	2018
	7.98	2.04	Other	2018
	6.13	2.06	Other	2018
	4.93	2.01	Other	2018
	6.23	2.08	Other	2018
	5.91	2.02	Other	2018
	5.65	2.00	Other	2018
	5.15	1.95	Other	2018
Li et al., 2018, Joule [59]	11.76	1.62	Other	2018
Yu et al., 2019, ACS Applied Materials & Interfaces [106]	2.64	1.28	Other	2019
	3.11	1.56	Other	2019
	3.57	1.53	Other	2019
	4.04	0.64	Other	2019
Wang et al., 2020, Materials Today Energy [152]	9.70	3.1	Other	2020
	18.39	3.94	Other	2020
	27.09	4.53	Other	2020
Tu et al., 2019, Small [116]	1.76	1.28	Other	2019
	7.03	1.94	Other	2019
	8.78	2.01	Other	2019
	10.54	2.11	Other	2019

Source	**EAI**	**Light** $[kg\ m^{-2}\ h^{-1}]$	**Shape**	**Year**
Wang et al., 2020, Science Bulletin [153]	3.42	1.91	Other	2020
	4.83	2.53	Other	2020
	6.25	2.72	Other	2020
	7.66	2.94	Other	2020
Wang et al., 2021, Nano Energy [154]	2.66	1.56	Other	2021
Li et al., 2020, Macromolecular Materials & Engineering [155]	1.01	1.65	Other	2020
Chen et al., 2020, ACS Sustainable Chemistry & Engineering [156]	2.51	1.42	Other	2020
This Work	6.33	3.41	Cylinder	2021
	41	18.35	Cylinder	2021
	70.33	34.66	Cylinder	2021

Appendix C

Interview Guide for Bungin Island Surveys

Introduction

Our names are _____, and we are students from the University of Sumbawa who are assisting with a research collaboration between the University of California, Berkeley and the non-profit, Energinesia. We are hoping to ask you some questions about the different places where you get water and how that water is used in the home. Are you involved with any of the water collecting responsibilities of your home and would you have about 20 minutes to answer some questions about your experiences with water? Yes | No

[No] Would there be a better time we could talk with you? Yes | No

[Yes] (*Come back at the scheduled time.)

[No] No problem, thank you for your time. (*Move onto the next household.)

[Yes] Thank you so much for your time. Would you be ok with us recording the audio of the interview? Your participation will remain confidential, but the recording will help us analyze the information from these interviews. Would this be ok? Yes | No

[Yes] Thank you! (*Use the phone app to record.)

[No] No problem, we will take notes by hand.

Before we begin, we just wanted to emphasize that these interviews are intended to collect information about everyday practices that concern the collection, storage, and use of water in your household. Your participation is completely voluntary, and if you wish—for any reason—to withdraw your participation from the study, either during the interview or after, we would be happy to accommodate. Additionally, if there are any questions that you do not wish to answer, you can just say “Next question”.

Do you have any questions before we begin? Yes | No

Interview ID: _____

Household Characteristics

Could you tell us about yourself and what you do on a typical day?

Who else lives with you in this house?

How many years ago was your home built? ____ years

Does your household have access to a boat during the day? Yes | No

Is your home connected to the Bungin Island's piped water supply? Yes | No

Interview ID: _____

Water Sources & Uses

Where do you get your water, and what do you use it for?

Water Source	Water Use(s)

(*Be sure to identify water sources for at least the following uses: drinking, cooking, cleaning, and bathing.)

Have the water sources that you typically use changed recently? Yes | No

[Yes] Could you explain what happened and how this has affected you?

Interview ID: _____

Water Collection & Storage

Could you describe the collection process for each of the water sources described previously?

Water Source: Collection Process:			
Collection Frequency per month	Amount of Water Collected liters	Time Required for Collection hours	Cost of Collection per liter
Water Source: Collection Process:			
Collection Frequency per month	Amount of Water Collected liters	Time Required for Collection hours	Cost of Collection per liter
Water Source: Collection Process:			
Collection Frequency per month	Amount of Water Collected liters	Time Required for Collection hours	Cost of Collection per liter

Interview ID: _____

Water Source: Collection Process:			
Collection Frequency per month	Amount of Water Collected liters	Time Required for Collection hours	Cost of Collection per liter
Water Source: Collection Process:			
Collection Frequency per month	Amount of Water Collected liters	Time Required for Collection hours	Cost of Collection per liter
Water Source: Collection Process:			
Collection Frequency per month	Amount of Water Collected liters	Time Required for Collection hours	Cost of Collection per liter

(*If it is not mentioned, ask if they purchase water from other households.)

Interview ID: _____

Who is responsible for collecting water from these water sources?

How is water from each of these water sources stored?

Is water treatment necessary before storage or use from any water sources? Yes | No

[Yes] Could you provide details about how and when treatment is used?

Is any of the water collected by your household sold to other households? Yes | No

[Yes] What is the source of the water that is sold?

[Yes] How much is water sold for? How is this price decided on?

[Yes] How much money is typically made from selling water?

[Yes] Is this a significant source of income for the household? Yes | No

Interview ID: _____

Reflections on Water Service

Are you satisfied with your water access?

What do you like about your current water access?

What would you wish was different about your water access?

Do you have any concerns about your future water access?

Do you know of any plans (for your household or for the community) to improve water access in the future?

Interview ID: _____

Visuals for Preliminary Design Feedback

Floating device that can purify seawater using sunlight:

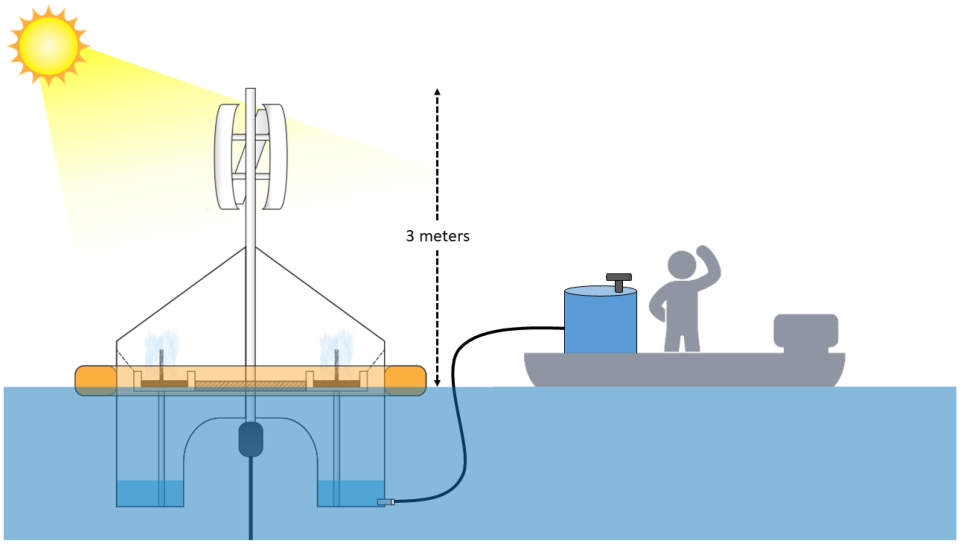

Map of Bungin Island:

↑ North

Interview ID: _____

Preliminary Design Feedback

(*Provide interviewee with the *Visuals for Preliminary Design Feedback* page.)
We are working on designing a device that can desalinate seawater. In order for the device to work, it needs to have access to sunlight and seawater. For this reason, we envision the device floating on the ocean surface. Currently, we believe that the device would be about as large as a small fish pond (~2 meters across) and we hope it can produce 10-50 liters of water per day.

Do you have any initial questions about the device that we can try to clarify?

What would you use the water collected from this device for?

Would you consider drinking the water from this device? Why or why not?

How would you evaluate whether the water is suitable for the uses discussed previously?

Interview ID: _____

Which households on Bungin Island face the greatest challenges when it comes to water access? (*Indicate by having the interviewee draw circles on the Map of Bungin Island.)

Due to boat traffic or pollution, where should we not locate the floating devices? (*Indicate by having the interviewee draw X's on the Map of Bungin Island.)

Are there any other considerations we should be aware of when determining where these devices should be located?

Which of the following options would you most prefer for obtaining water from the floating device? (*Circle the respondents answer below.)

A. You (or someone in your household) collect water directly from the device by using a boat.

B. Someone else collects water from the device and brings the water to a location on the island where it can then be collected by you (or someone in your household).

C. No preference between A or B.

How much would you be willing to pay for this water? Please explain your reasoning.

Do you have any additional feedback for the proposed use or design of the floating device?

Interview ID: _____

Conclusion

(*Collect *Visuals for Preliminary Design Feedback* from interviewee.)

Thank you so much for your time and thoughtfulness in answering these questions! To show our appreciation, we would like to give you a prepaid phone card with 150,000 IDR and a reusable water bottle. (*Give the interviewee their gift for participating in the interview.)

For our records, could we take a photo of the front of your home? Yes | No

[Yes] Thank you! (*Take a photo after you conclude the interview.)

[No] No problem. (*Record rough location of home in *Post-Interview Debrief*.)

Lastly, if you have any additional comments or questions, please reach out to us through this contact information. (*Give the interviewee our business card with contact information.)

Thank you again!

Interview ID: _____

Post-Interview Debrief

(*This section should be completed privately by the interviewers after each interview, interviewees should not be present or within earshot.)

What are the household coordinates? (*Use Google Maps)

Roughly where on the island was the household located? (*Indicate on the map below.)

Are there any additional observations about the household, interviewee, or interview that should be recorded?